ABSTRACT

PROTON INDUCED SPALLATION OF ^{20}Ne AND THE ASTROPHYSICAL PRODUCTION OF THE LITHIUM ISOTOPES

By

Lolo Marangkup Panggabean

Cross sections for production of masses 6 and 7 in the proton induced spallation of ^{20}Ne have been measured at the proton bombarding energies 30, 35, 40, and 42 MeV. The magnitudes of the mass 6 and mass 7 cross sections at each energy are equal within the experimental uncertainties, both rising from 1.5 mb at 30 MeV to 4 mb at 42 MeV. The angular distributions for both masses at all energies are very similar; they go down monotonically at back angles.

The measurements employed the time-of-flight (ET^2) technique for particle identification. The energy E was measured by stopping the particles in a surface barrier Si-detector and the time-of-flight T was measured by measuring the time interval between the time the particles were created and the time of their arrival at the detector.

The time width of the proton beam bursts (0.4 nsec to 0.6 nsec) from the Michigan State University Cyclotron yielded a mass resolution that was sufficient for this experiment.

The ^{20}Ne target gas of 99.66% purity was contained in a cylindrical gas cell, 1.25 in. high and 4.75 in. in diameter, which was equipped with kapton window for the proton beam and a thin formvar window as an exit window for the reaction products. The pressure of the target gas varied from 21 to 43 torr.

Together with the cross sections for mass 6 and mass 7 that are available in the literature, the cross sections measured in this laboratory were used to calculate the ratio of the production rate of ^{7}Li to that of ^{6}Li by the protons in stellar flares, assuming a spectrum of the form $E^{-\gamma}$, where γ is a constant. It was found that a spectrum $E^{-7.1}$ was required to produce the experimentally observed abundance ratio of 12.5. The steepest spectrum observed in solar flares has $E^{-5.6}$. It is suggested that one must include the $\alpha + \alpha$ reactions as additional sources of ^{7}Li.

PROTON INDUCED SPALLATION OF ^{20}Ne AND THE ASTROPHYSICAL PRODUCTION OF THE LITHIUM ISOTOPES

By

Lolo Marangkup Panggabean

A THESIS

Submitted to
Michigan State University
in partial fulfillment of the requirements
for the degree of

DOCTOR OF PHILOSOPHY

Department of Physics

1972

ACKNOWLEDGEMENTS

I sincerely would like to thank Prof. S. M. Austin for introducing the topic of research and his guidance and enduring patience from the beginning of the experiment to the end of the final analysis of the experimental results.

I would also like to thank Dr. H. W. Laumer for the valuable discussions that we had about the detail of the experimental technique and his assistance in collecting the data each day during the experiment.

I would like to thank Dr. R. A. Hinrich who was willing to take the place of Prof. S. M. Austin during his leave of absence and Mr. S. H. Fox and D. Larson who were willing to assist in data collection when called upon.

Help from Mr. N. Mercer and his staff from the machine shop and the staff of the Cyclotron Laboratory are greatly appreciated.

I would like to thank the National Science Foundation and Michigan State University for their support during the research.

Last but not least, I would like to thank the Ford Motor Co. who provided the support during my first year of study at Michigan State University.

TABLE OF CONTENTS

Page

TABLE OF CONTENTS (cont.)

LIST OF TABLES

LIST OF FIGURES

LIST OF FIGURES (cont.)

LIST OF APPENDICES

Chapter I

INTRODUCTION

I.1 Astrophysical Problem

While the thermonuclear reactions in the interior of the stars can explain the abundances of many of the light elements ($A \leqslant 60$) as the result of a series of fusions of lighter elements into heavier ones (BBFH 57, Ba 71), one does not expect the isotopes of the elements D, Li, Be, and B to be formed by the same mechanism. The origin of this expectation is found in Figure I.1 (BBFH 57) where the measured abundances of the elements in the solar system are plotted as a function of the mass number A. It is seen that Li, Be, and B lie well below the general curve, being a factor of 10^7 to 10^9 less abundant than He. The reason for this low abundance is found in the nuclear physics of these nuclei.

Isobars with $A = 5$ (^{5}He and ^{5}Li) and $A = 8$ (^{8}Li, ^{8}Be, and ^{8}B) are not stable and hence are not found in nature. The isobars $A = 6, 7, 9, 10$, and 11 do have stable isotopes (^{6}Li, ^{7}Li, ^{9}Be, ^{10}B, and ^{11}B) but are not

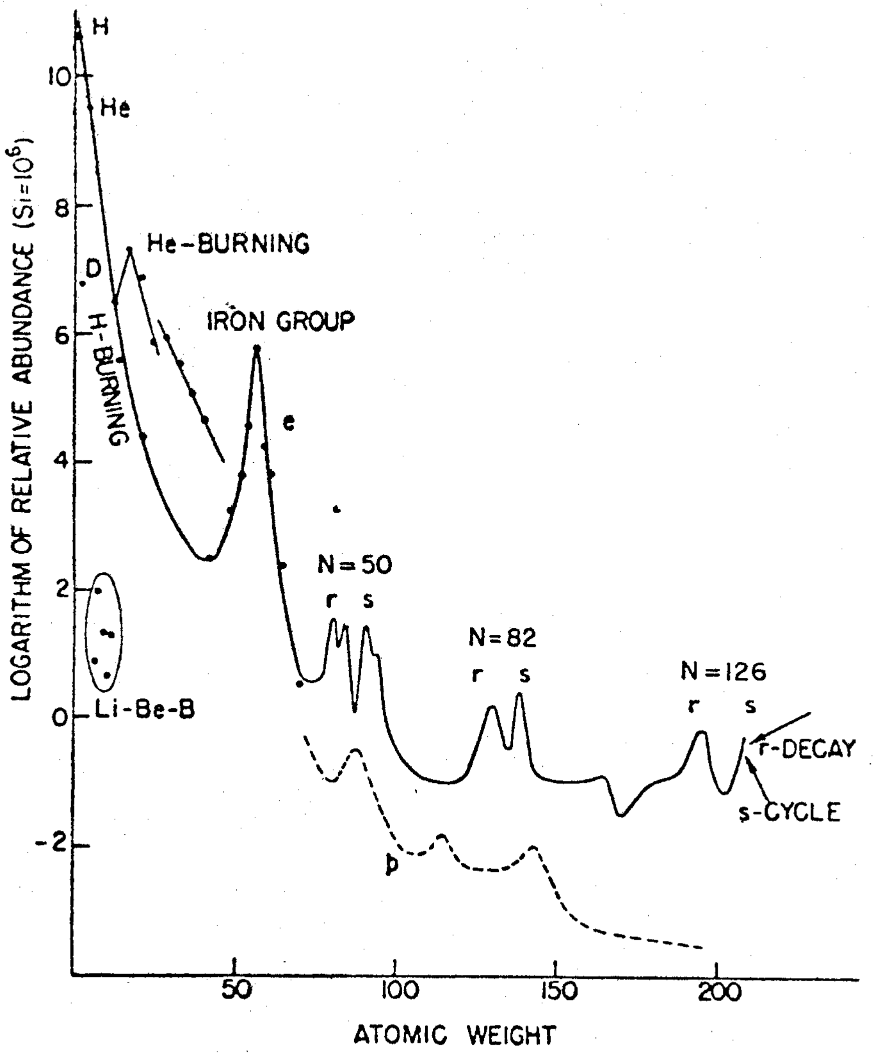

Fig. I.1.--Curve of Relative Abundances From (BBFH 57) Based on Suess and Urey.

expected to survive due to (p, α) reactions on these isotopes in the interior of the stars at any temperature above 10^6 ^{0}K (BGRS 67). Thermonuclear reactions proceed at a non-negligible rate only at temperatures a factor of ten higher than this, so these isotopes will not be present in significant amounts in the ashes of a thermonuclear process. Thus we require a mechanism for the formation of Li, Be, and B in a region of low temperature, i.e. a process which is not thermonuclear in nature.

W. A. Fowler, G. R. Burbidge, E. M. Burbidge, and F. Hoyle (FBB 55, BBFH 57) first suggested such a mechanism, namely proton or alpha induced spallation reactions on suitable targets found at the surface of the stars or in the interstellar medium. Taking into consideration the threshold energy and the abundances of elements in the solar system the most important targets appear to be ^{12}C, ^{14}N, ^{16}O, and ^{20}Ne and the incident particles are protons and alphas from solar flares and/or cosmic rays.

I.2 Calculations of Cross Sections

To calculate the amount of Li, Be, and B produced in the proton or alpha induced reaction one needs the spallation cross section for each element from each target in addition to the flux of the incoming protons or alphas and the abundances of the target elements.

There have been many attempts to calculate these cross sections. The calculations are based on the Serber model (Se 47), i.e. a fast nucleon cascade followed by a slow evaporation according to Weisskopf (We 37), or a fast nucleon cascade followed by a fast breakup according to Fermi (Fe 50). Dostrovsky and several other collaborators have done a series of calculations on different targets at various energies (Do 65, Do 68). They applied the Monte Carlo calculation technique for the fast cascade as prescribed by Metropolis et al. (Me 58) and another Monte Carlo calculation for the evaporation part following the methods of their previous work (Do 58, Do 59, Do 60, Do 61). They also included the effects of a diffuse nuclear surface as initiated by Chen et al. (Ch 68). N. T. Porile and S. Tanaka (Po 64), R. G. Korteling and A. A. Caretto Jr. (Ko 70a, Ko 70b) have also applied a similar approach in their papers. The results of these calculations are fairly good, only about 20 to 30% of the calculations deviating from the experimental values by more than a factor of two. These calculations are for heavy targets (except Do 68) and high energies.

For lighter targets as ^{12}C, ^{14}N, ^{16}O, and ^{20}Ne where the evaporation model is probably not suitable, the Fermi break up model has been applied by R. Bernas and E. Gradsztajn (BGRS 67) to follow the nuclear cascade. For the energies considered in this paper (70, 100, 156, and 200 Mev) the results are, for Li, Be, and B, in good agreement with the experimental values except for simple reactions like pick up of a few nucleons. Unfortunately these simple processes sometimes dominate the total production cross section.

G. Rudstam (Ru 55, Ru 66) has devised a semi-empirical formula which predicts the cross sections for heavy targets (Ca) and R. Silberberg and C. H. Tsao have extended the formula to include light targets (Si 72). While each of the methods predicts, one way or another, the approximately correct cross sections at high energies none of them gives reliable information for the energy region from the threshold up to about 100 MeV where the cross section rises very rapidly reaching its maximum value (see Figure IV.1). In this energy region then, one has no option but to measure the cross sections.

I.3 Importance of Low Energy Region

All proton spectra that have been observed decrease rapidly with energy E_p. The importance of the cross sections in the low energy region then depends on their slope. For some models the low energy cross sections are extremely important, even dominant (see Section IV.2).

I.4 Cross Section Measurement for ^{20}Ne

While fairly complete measurements have been made for targets of ^{12}C, ^{14}N, and ^{16}O (see Chapter IV) the production cross sections for ^{20}Ne targets had not been measured at any energy.

In this thesis I describe the cross section measurements of the production of the isobars A = 6 and A = 7. An attempt to measure the cross sections for A = 10 and A = 11 was hampered by the available mass resolution and hence the values of the cross sections for A = 10 only are reported.

The technique is based on the kinetic energy formula for a particle with a constant velocity V, i.e. $E = 1/2\ MV^2$ where E and M are the kinetic energy and the mass respectively. Also V = D/T where D and T are the distance traveled and the time of flight over the distance D (see Figure I.2). By rearranging it one can write:

$$ET^2 = M(1/2\ D^2) \tag{1.1}$$

i.e. ET^2 is proportional only to the particle mass and other constants. Both the energy E and the time of flight T of the reaction products can be measured and with the help of the computer the product ET^2 can be computed on-line, displayed and stored; thereby the measurement of the mass M is made possible.

A weakness of the time-of-flight technique is that it does not separate the members of an isobar from each other. For the purpose of astrophysics, however, it is sufficient to measure the cross section of an isobar since there is only one member of each isobar A = 6, 7, 9, 10, and 11 which is stable. The rest have short half lives compared to an astrophysical time scale and β-decay to the stable member. The one exception is ^{10}Be with a half life of 2.7×10^6 years. For the energies considered in this thesis (30 to 42 MeV), however, it is not a serious

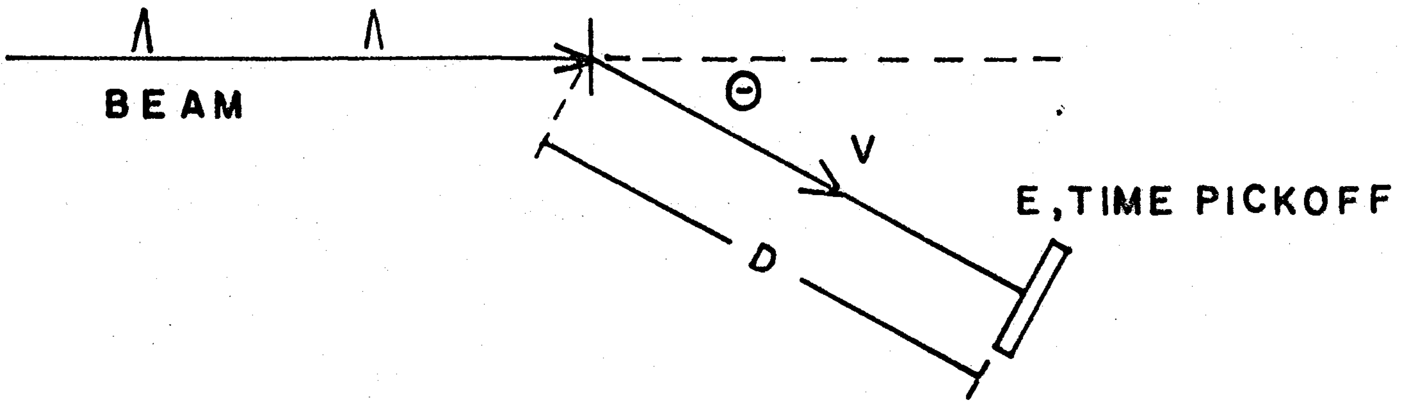

$$E\,T^2 = \frac{1}{2} M V^2 \left(\frac{D}{V}\right)^2 = M\left(\frac{1}{2} D^2\right)$$

Fig. I.2.--Schematic Diagram of Time-of-Flight Technique. Energy (E), Time-of-Flight (T) and Distance-of-Flight (D) are Quantities to be Measured.

problem since the threshold energy for ^{10}Be is high (37.8 MeV).

The measurement technique uses time of flight for particle identification and has been described in a paper by Davids et al. (Da 70). Here it is modified for use with a gas target, as is discussed in detail, together with the experimental procedures, in Chapter II.

The variable energy proton beam from the Michigan State University Cyclotron has a burst width of $\leqslant$ 0.3 nsec insuring a small time spread for the reaction products and hence a good mass resolution.

The angular distributions $\sigma(\theta, E_p)$ were obtained for A = 6 and A = 7 at 30, 35, 40, and 42 MeV proton bombarding energies. Integrating $\sigma(\theta, Ep)$ over the angle θ the cross section $\sigma(E_p)$ is obtained. The analysis necessary to obtain these cross sections is presented in Chapter III.

Together with the cross sections that are available (see Table IV.2) and predictions from isospin systematics (valid at high energies) these cross sections will be used to calculate the ratio of the production rate of the isobars A = 6 and A = 7. This is presented in Chapter IV.

Chapter II

EXPERIMENTAL APPARATUS AND PROCEDURES

II.1 Cyclotron Facilities

The Michigan State University sector-focused Cyclotron is used to accelerate protons up to 30, 35, 40, and 42 MeV in conducting this experiment. The layout of the machine, the beam line that leads to the 40 inch scattering chamber in which the experiments were carried out and the focusing elements are shown in Figure II.1. Q_1, Q_2, . . . Q_{10} are the magnetic quadrupole focusing elements and M_1, M_2, . . . M_5 are beam alignment, analyzing and beam switching dipole magnets.

When properly run the cyclotron can produce an analyzed proton beam with an energy resolution $\leqslant 0.1\%$. The energy analysis slits at boxes 3 and 5 were set for energy resolution of 0.07%. The careful design of the central region makes it possible to select a narrow phase group. A time width Δt of the proton beam burst of < 0.3 nsec FWHM has been obtained. In this experiment Δt varied from 0.4 to 0.6 nsec FWHM. This time resolution is

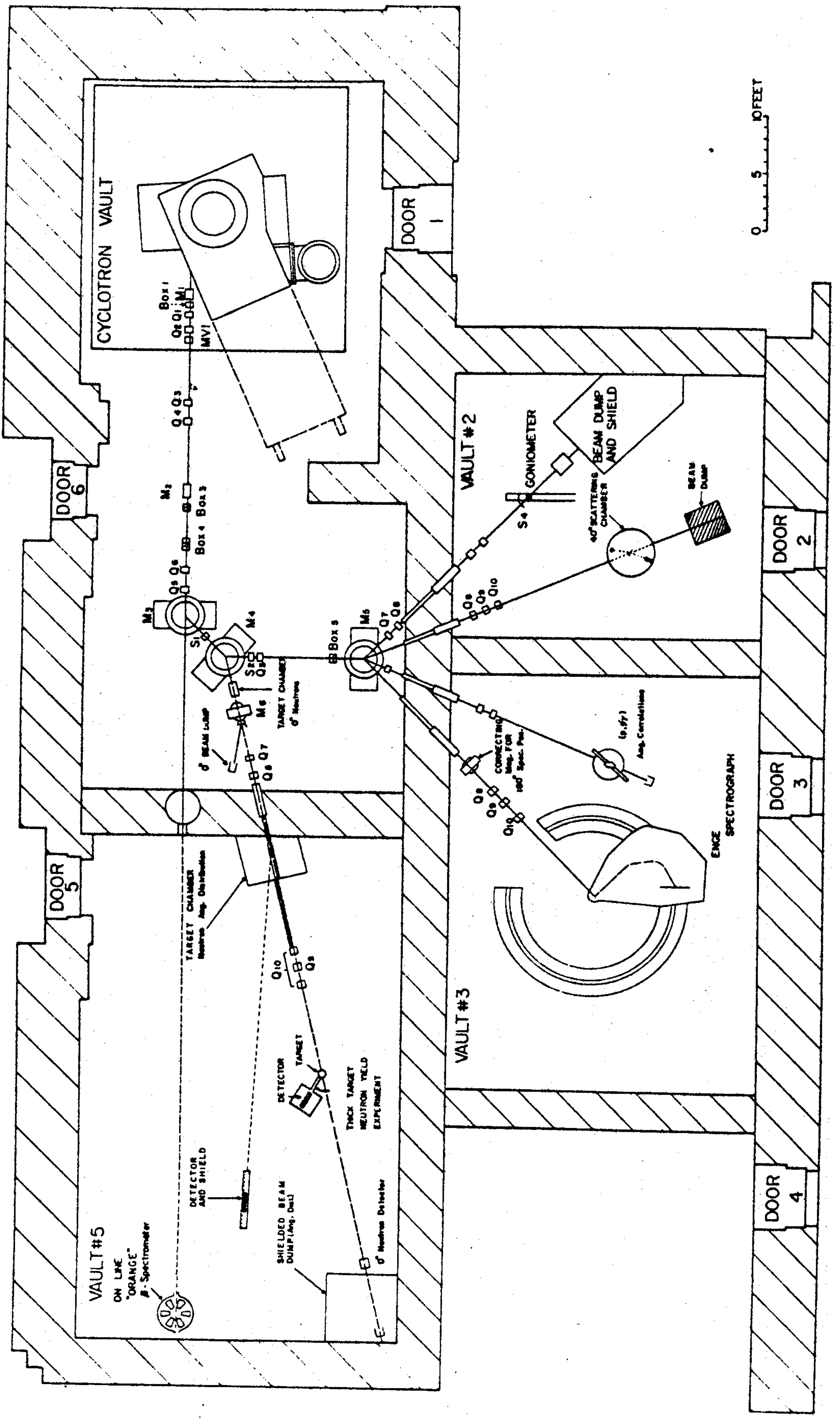

Fig. II.1.--Schematic Drawing of the Beam Transport and Analyzing System.

sufficient for our needs. For the present experimental setup, the fastest particle of interest (i.e. 20 MeV ^{6}Li ion) has a time of flight of 12 nsec, so the width of the beam corresponds to only a spread of 3.5% in time or less than 7% in mass since the contribution of the time spread to the spread in mass is twice the percentage spread in time (see Section III.2). The neighboring isobars are separated by (7-6)/7 = 14%.

In most cases 3 to 4 μ amps of protons are extracted with 100% efficiency and a current of 300 to 800 n amps is incident on the target in a beam 0.03 to 0.05 in. wide and less than 0.1 in. high. The proton beam is collected in a Faraday cup which is 57 in. long and 4 in. in diameter and integrated by a current integrator (ELCOR Model A310B). The Faraday cup was isolated from the scattering chamber by a 1.5 in. plastic ring and was surrounded with a water-filled fifty-eight-gallon barrel to shield the detectors from radiation produced by the stopping beam.

II.2 Scattering Chamber

The scattering chamber[1] is located in the experimental vault no. 2 (see Figure II.1). Its inside diameter is 40 in. and the height provides 13.5 in. of working space above the beam line. The chamber is provided with a rotatable table and a monitor arm. The beam line is 4.985 in. above the table and 2.625 in. above the arm. Both the table and the arm are equipped with radial groves and dowel pin holes along the sides of the groves at the radii of 6 in. to 18 in. separated by 2 in.

During these experiments the proton monitor counter was positioned on the table and the detectors and the target were positioned on the arm; the table was kept in position while the arm was rotated to the desired angle. The position of the arm was read through a digital readout with an accuracy of 0.01° least count. The chamber was evacuated down to 7 X 10^{-6} torr.

---

[1] Manufactured by William M. Brobeck & Associates, Berkeley, California.

II.3 Target

A gas target of ^{20}Ne, isotopically enriched to 99.66 Mol % with a gross composition of 99.71 Mol % Ne,[1] is used. The main contaminants in the target are hydrogen (0.22 Mol %), helium (0.07 Mol %), nitrogen (< 0.01 Mol %) and carbon dioxide (< 0.01 Mol %). Other contaminants are ^{21}Ne (0.05 Mol %) and ^{22}Ne (< 0.01 Mol %).

Since the contaminants make up only a very small percentage of the target (0.34 Mol %) their presence has been ignored in the measurement of the pressure in the gas target. For the same reason the contributions to the cross section of productions of Li, Be, and B by C, O, ^{21}Ne, and ^{22}Ne have been ignored.

The data at 42 MeV was taken with pressure of 20.8 torr Hg while the rest were taken at various pressure ranging from 24.2 to 43.3 torr. For the slit system used this corresponds to a target thickness of 22.2 $\mu g/cm^2$ at 20.8 torr and 46.21 $\mu g/cm^2$ at 43.3 torr assuming the temperature of the target is the room temperature (300° K).

---

[1] Manufactured by Monsanto Research Corporation, Miamisburg, Ohio.

II.4 Gas Cell and Slit System

The gas is contained in a gas cell with a diameter of 4.75 in. and a height of 1.25 in. It essentially consists of two pieces of circular plates, made of brass, connected by a spacer that makes up one-sixth of the wall of the cell (See Figure II.2). The rest of the wall is made up of 0.0005 in. Kapton[1] through which the proton beam can go without losing a significant amount of energy (a 30 MeV proton loses 0.030 MeV in 0.0005 in. Kapton). The construction of the cell has been described in detail elsewhere (La 71).

A shell whose design is explained in (La 71) can be positioned through the spacer so as to function as an exit slit for the reaction products. The slit is covered with 16 double-layers of formvar films that, on the average, corresponds to 38 $\mu g/cm^2$. Earlier experiences proved that the formvar film might break so one needed several slits (see Section II.6). The width of the slit ranges from 0.0425 to 0.0435 in. and they are 0.75 in. high. The height and the rear end of the shell are large

---

[1] Available from E. I. DuPont de Nemours, Wilmington, Delaware.

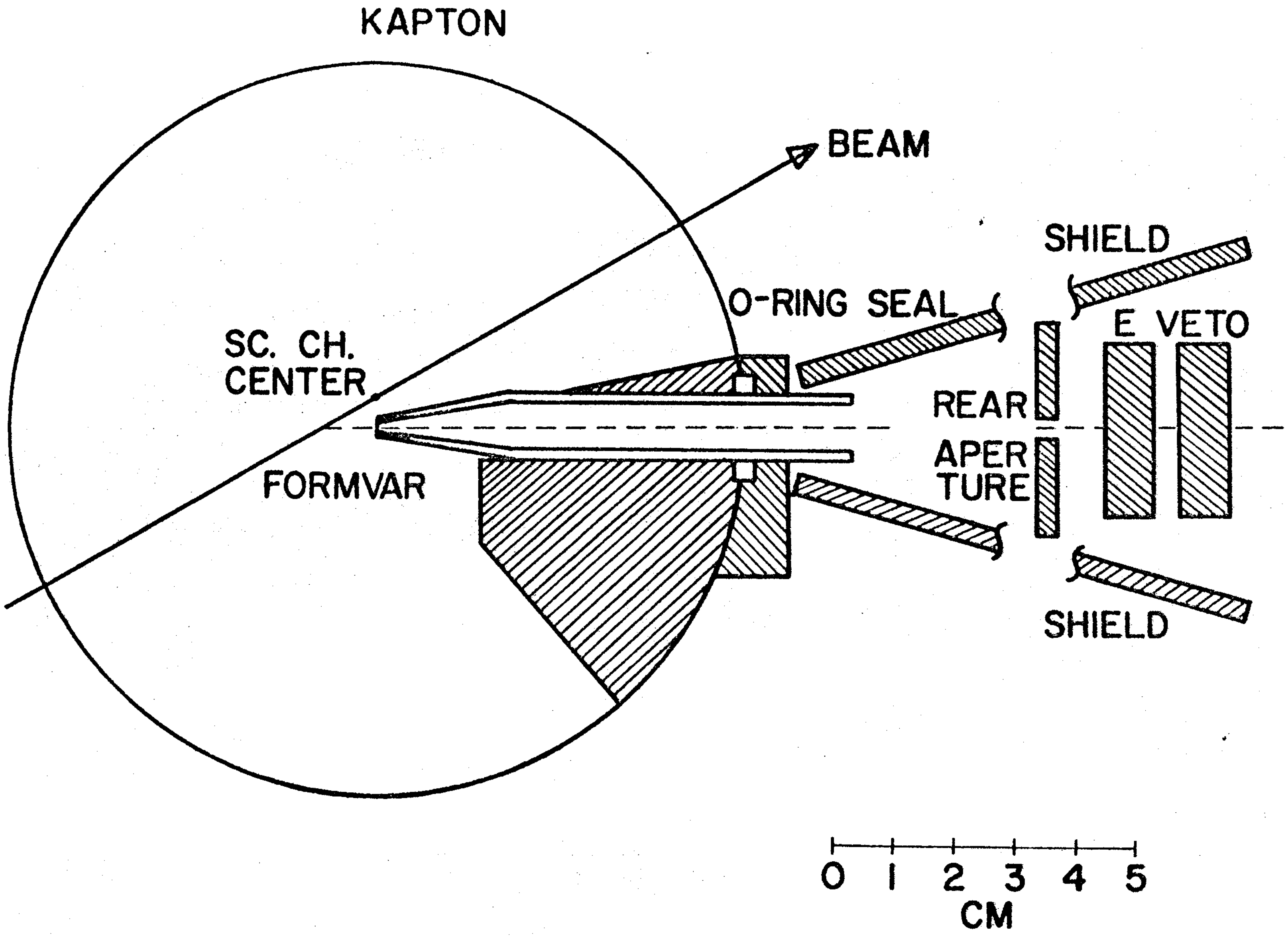

Fig. II.2.--Horizontal Cross Section of the Gas Cell, Slits and Detectors.

compared to the dimensions of the rear aperture (0.125 in. by 0.25 in.) which is positioned at a distance of 9.6 inches from the front slit; hence, it is treated as a two-slit system with a rectangular rear aperture according to the description of Silverstein (Si 59).

The gas cell with the shell, the rear aperture, and the detectors are fixed in their position on a steel rail that is mounted on the arm of the scattering chamber. The whole system moves with the arm of the scattering chamber as a unit (see Figure II.2).

The shield in Figure II.2 is made of lucite, 4.5 in. thick on the side facing the port and 1 in. on the other side. It is used to protect the detectors from neutrons.

From Figure II.2 it is seen that the reaction products have to traverse a certain distance through the gas before they reach the formvar window. This distance depends on the angle between the beam and the detector and on the position of the shell. The gas cell itself is positioned off the center of the scattering chamber by 0.021 in. in a direction perpendicular to the radial grove of the arm of the scattering chamber and 0.25 in.

in the direction parallel to the grove, away from the center of the chamber. This allows the shell to be positioned such that at 15° angle of detection the distance between the beam and the front slit is about 1 in. and with the same setting at 90° the distance will be about 0.25 in. Both distances are small enough so there is no need for a readjustment of the position of the shell when the angle of detection is changed.

There are both disadvantages and advantages associated with the use of a gas target. One disadvantage is that the exit areal density and hence a correction for spectrum cutoff (see Section III.3) is angular dependent. With a pressure of 43.3 torr at 15° the exit areal density is 118 $\mu g/cm^2$ gas and at 90° it is 29 $\mu g/cm^2$ of gas. To this, 38 $\mu g/cm^2$ formvar window is to be added. In addition to that there is an imbedded disadvantage in the use of a gas cell with a time of flight technique, i.e. the difference in the flight distance for particles created at various points along the passage of the proton beam causes a spread in the flight time. The advantages are the accuracy of the measurement of target thickness and that it is possible to obtain a very pure and thin target. Of course for ^{20}Ne, there are essentially no other options available.

II.5 Pressure Measurement

The pressure of the gas target is measured with an oil manometer connected to the gas cell during the experiment. This manometer was designed for the measurement of the low pressures involved in this experiment. It has a range of 135 cm of oil and the meniscus can be read to within 0.5 mm; hence, the pressure can be read to within ± 1 mm of oil or, for most cases, ± 0.17% of the pressure.

Octoil-S pump fluid[1] is used in the manometer; it has a low viscosity that provides a quick reading and a very low vapor pressure (2.7×10^{-7} torr at 25° C) compared to the gas pressure which, in most cases, was approximately 40 torr. In these experiments the vapor pressure was ignored since the error associated with it is very small (6.8×10^{-8}%). Its density at 25°C is 0.9812 g/cm^3.

---

[1] Manufactured by Consolidated Vacuum Corporation.

A manifold interconnects the manometer, scattering chamber, gas cell, and the gas cylinder containing the target gas.

To check the local heating by the proton beam in the gas both the elastically and inelastically scattered (leaving ^{20}Ne in its first excited state) protons were counted and compared at two experimental cases. In the first case a 100-namp. beam was sent through the target for 100 sec. while in the second case a 500-namp. was sent for 600 sec. The ratio of the number of protons per coulomb in both cases was 1.004 while the ratio of the pressure readings was 1.004. This indicates that the beam heating by the proton beam is negligible.

II.6 The Thin Formvar Window

The formvar window is prepared in a simplified version of the method of Hoogenboom (Ho 61). Formvar-E ($C_4H_{16}O_8$) is available in the powder form.[1] A certain amount of formvar is diluted in 1-2 dichloroethane to obtain a 2% (by weight) solution. A film is obtained by dipping the tip of a piece of wire (14 B.S. gauge)

---

[1] Available from Shawinigan Resins Corporation, Springfield 1, Massachusetts.

into the formvar solution and then drawing a line on the surface of distilled water contained in a glass beaker thereby forming a thin layer of formvar solution on the surface of the water. Within a few seconds the 1-2 dichloroethane evaporates leaving a formvar film.

The film is lifted from underneath with the help of a square loop somewhere in the middle of the film. One double-layer film is then obtained and directly applied on to the shell. In this work a 16-double-layer formvar window has been used.

The performance of the formvar window prepared this way has been very satisfactory. Its durability seems to lessen in the case of a repeated pumping down of the gas cell and letting it up to atmospheric pressure.

The thickness of the film was measured by measuring the energy loss of a 5.48 MeV alphas from an Am-source. The result is that each double layer, on the average, has a thickness of 2.4 ± 0.2 $\mu g/cm^2$ (La 71). The total thickness of the window used here is thus 38 ± 3 $\mu g/cm^2$.

II.7 Main Detectors

A silicon surface barrier detector, called the E detector (see Figure II.2) is used to measure the energy of the particles. The thickness of this detector is so chosen that the most energetic particle produced in the reaction, that is ^{6}Li in the ground state, is just stopped in the detector. At 30 and 35 MeV a 86 μ-detector is used (needed 64 μ) while at 40 and 42 MeV a 150 μ-detector is used (see Appendix A).

The detector was cooled by circulation of alcohol at -78.5°C and was overbiased by a factor of two to decrease the detector risetime and increase the sensitivity of the time pickoff unit (see Section III.3).

A second detector, called the veto detector, is used to detect particles that pass through the E detector. These are lighter particles which are not of interest. For all runs the thickness of the veto detector is 260 μ. The purpose of the veto detector is to avoid the dead-time of the analog-to-digital-converter associated with processing the large number of detected protons and alpha particles.

II.8 Monitor Detector

To monitor the elastically scattered protons a NaI(Tl) detector is used (see Figure II.3). The discriminator level of the monitor single-channel-analyzer was adjusted to accept both elastically scattered protons and inelastically scattered protons leaving ^{20}Ne in its first excited state. The logic signal from the single-channel-analyzer was sent to a scaler and to channel zero. The total proton spectrum was also recorded with a multi-channel-analyzer (ND 160).

II.9 Electronics for Time of Flight Measurement

In this section (and hereafter) the electronic modules used during the experiments will be frequently mentioned. For simplicity the names of the modules will be abbreviated. Below is the list of the modules together with their descriptions and models.

	MODULE DESCRIPTION	MODEL
1.	Fast Discriminator (FD)	ORTEC 417
2.	Delay (DELAY)	ORTEC 425
3.	Dual Coincidence (DUCO)	C102B/N, EG&G
4.	Dual Discriminator (LRS)	Model 121 Discriminator LeCroy Research System Corp.

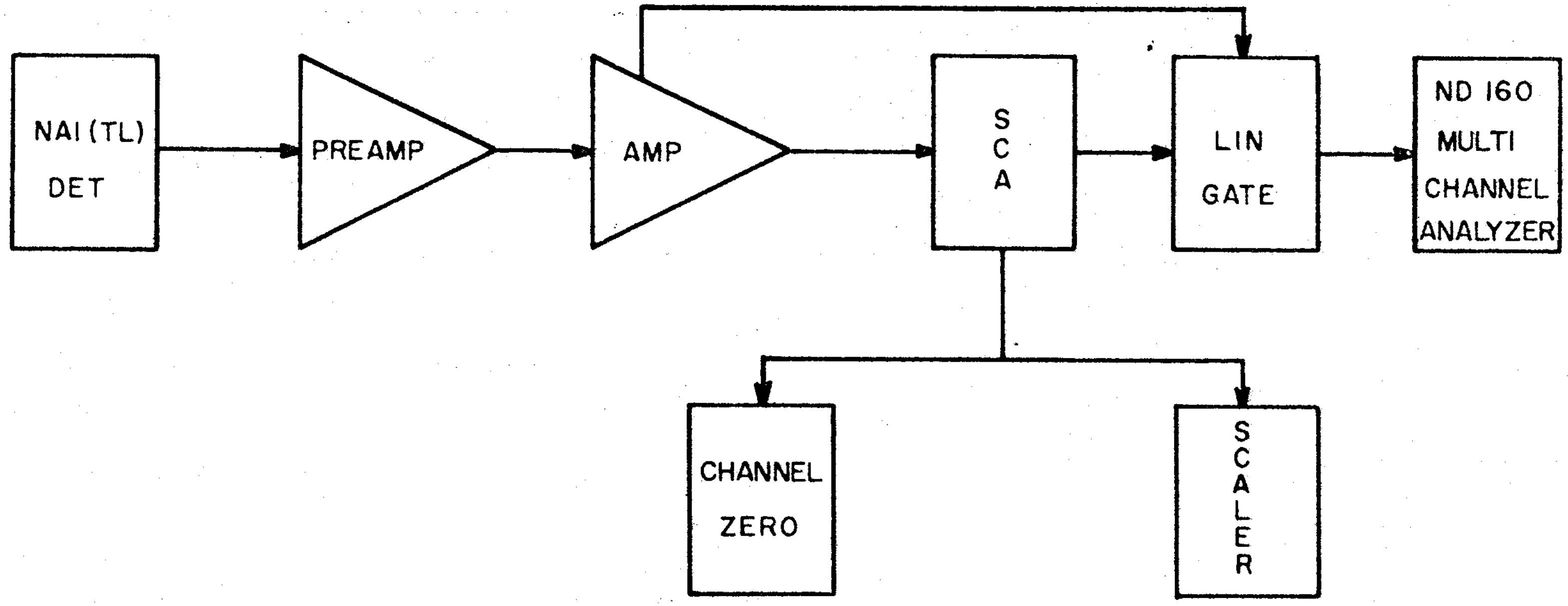

Fig. II.3.--Block Diagram of Monitor Electronics.

5.	Time Pickoff Control (TPC)	ORTEC 403A
6.	Time Pickoff Unit (TPU)	ORTEC 260
7.	Time to Amplitude Converter (TAC)	ORTEC 437
8.	Timing Single Channel Analyzer (SCA)	ORTEC 420
9.	Linear Gate and Stretcher (LINGATE)	ORTEC 442
10.	Preamplifier (PRAMP)	ORTEC 109A
11.	Selective Active Filter Amplifier (AMP)	ORTEC 440
12.	Gate and Delay Generator	ORTEC 416
13.	Universal Coincidence (UCOIN)	ORTEC 418
14.	Analog to Digital Converter (ADC)	NORTHERN SCI NS-629
15.	NaI(Tl) Detector	MSU-L. LEARN
16.	Multichannel Analyzer	ND 160
17.	Scaler	ORTEC 430
18.	Computer	XDS 7

The block diagram for the electronic setup is shown in Figure II.4. The upper row is for the energy pulses, the middle row is for the veto pulses, and the lower row is for the time pulses.

The energy pulse goes through the TPU (thereby generating a pulse that serves as a start pulse for the TAC) and

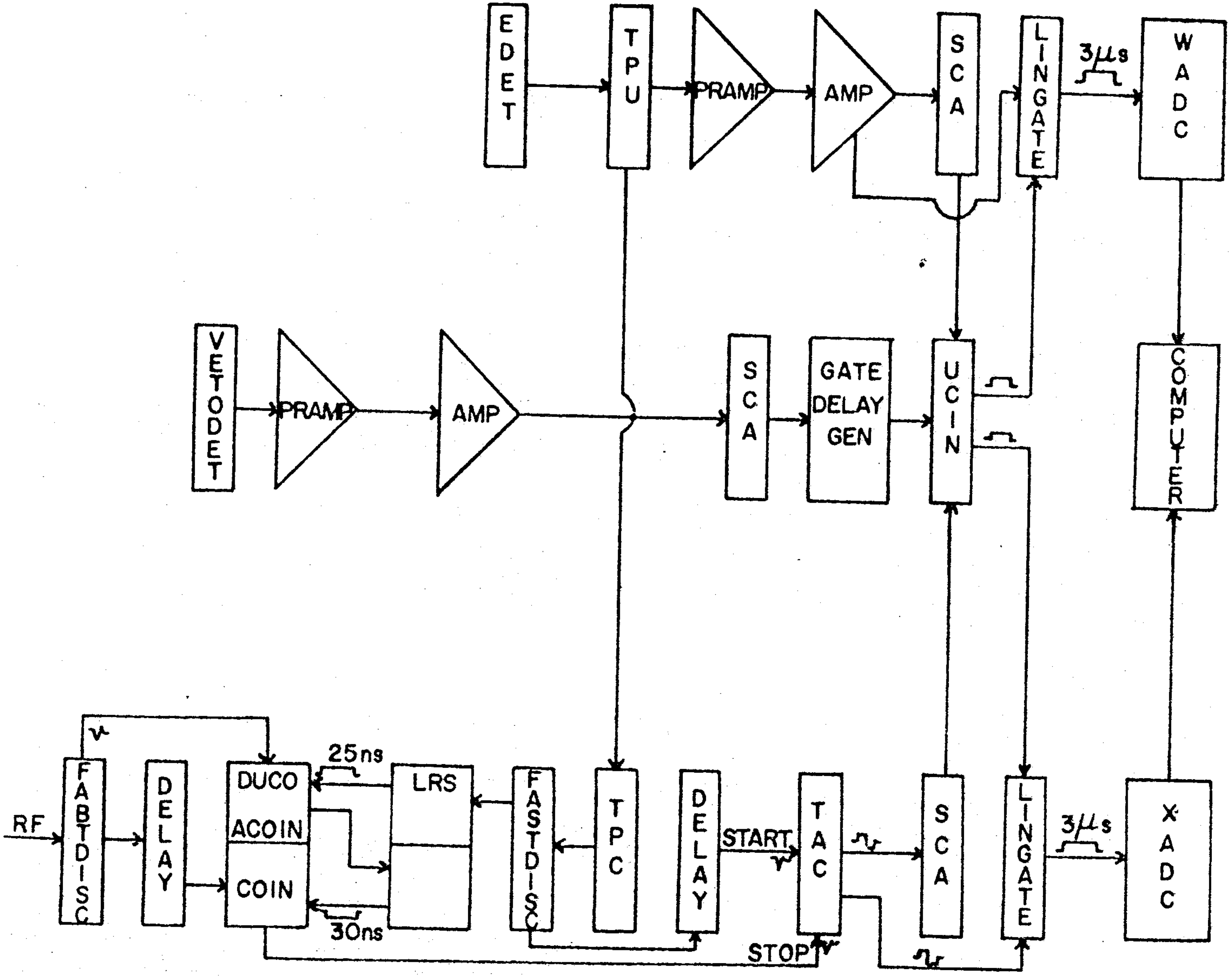

Fig. II.4.--Block Diagram of Time-of-Flight Electronics.

is then amplified. The prompt output goes to a SCA to generate a logic pulse that goes to a UCOIN module in a coincidence mode.

Pulses from the cyclotron RF system were used as stop pulses for the TAC, the output of which is the time signal. One of the TAC output pulses goes to another SCA to generate a logic pulse that goes to the UCOIN module in coincidence mode. This means the UCOIN module will output a pulse if there is a coincidence between the energy and the time signal in which case the gate in each of the linear gates for the energy and time signals are open and letting the other half of the energy and time signals go through; they are adjusted so they enter the ADC's at the same time. The ADC's were set in a synchronous mode.

The pulse from the veto detector, after amplification, goes to a SCA, then to a Gate Generator and finally to the UCOIN module in anti-coincidence mode. This veto pulse will inhibit an output of the UCOIN even if the energy and the time signal are in coincidence in which case there is no pulses entering the ADC's. This case corresponds to a particle passing through the E detector which is not of interest.

The rest of the modules in the lower row are used to avoid the non-linear region of the TAC (15% of the range setting). They are shown in Figure II.5.

The non-linear region can be avoided by a proper delay of the stop pulses. If, however, every stop pulse is accepted the range of time that can be measured is 15 nsec. less than the period of the RF. The setup shown in Figure II.5 allows one to reject or to accept a stop pulse if it arrives before or after a certain period of time which in this experiment was 25 nsec. with a range setting of 100 nsec. The entire RF period is then available for analysis of pulses.

The signal from the TPC is fed into a FD, the outputs of which are fed into the LRS module and, after proper delay, into the START terminal of the TAC. Upon arrival of the input pulse at the LRS module it generates a positive going pulse the length of which is adjustable; in this experiment it was chosen to be 25 nsec. long (the non-linear region was 15 nsec.). Pulses from the RF system are fed into another FD whose outputs are used to select the stop pulse and as a stop pulse for the TAC.

The selection of the stop pulse is done by feeding one of the stop pulses and the positive going pulse from the

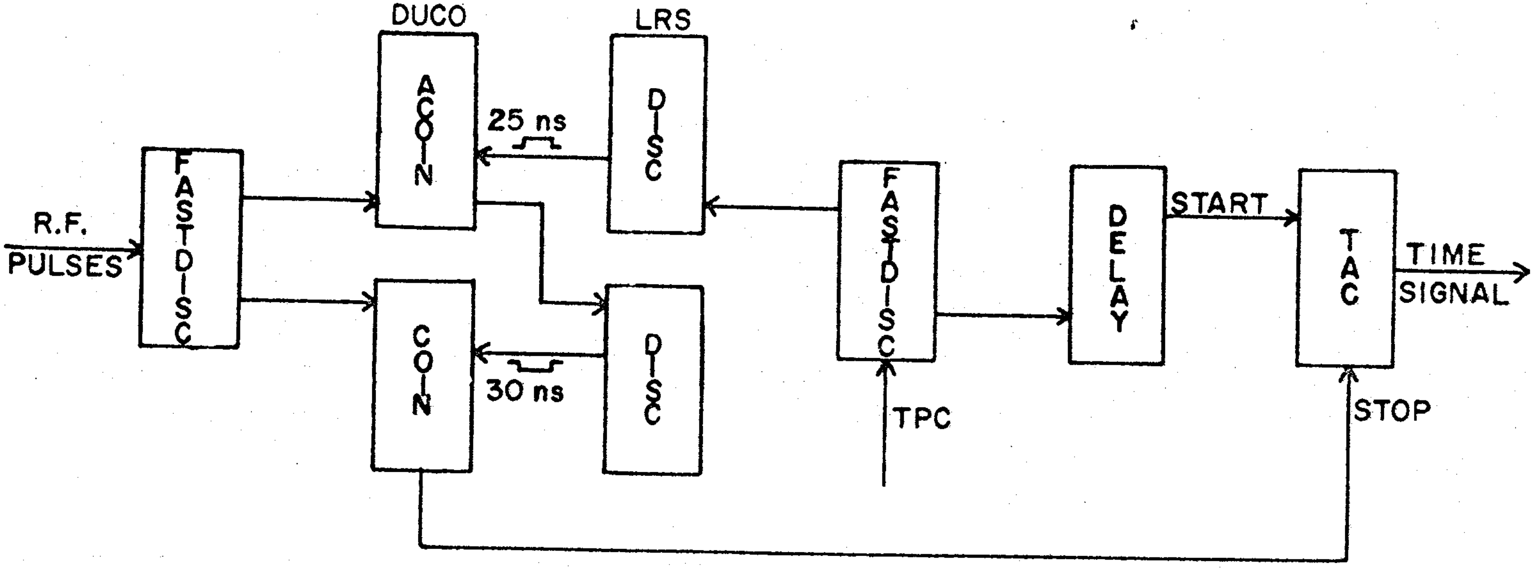

Fig. II.5.--Electronics Used to Avoid the Non-linear Region of the TAC.

LRS module into a DUCO module operated in anti-coincidence mode. The DUCO module gives an output which is fed into the other half of the LRS module which will generate a negative going pulse. This negative going pulse, together with the other stop pulse, properly delayed, are fed into the other half of the DUCO module operated in coincidence mode. The final output of the DUCO module serves as the selected stop pulse and is fed into the TAC. The start pulse then is delayed by the amount of time necessary to carry out this logic.

The net result is that only stop pulses which arrive 25 nsec. after the start pulse are recorded. Long flight times correspond to small TAC pulses, the lowest energy identifiable particle yielding a 25 nsec. pulse while short flight times give large TAC pulses, the fastest particle identified yielding a 25 nsec. + 1 RF period pulse. A more detailed explanation appears in Appendix B.

With the time-of-flight technique it is clear that there is a low energy limit for each mass such that it can be unambiguously assigned to a mass band (see Appendix B). From the kinematics of the reaction the kinetic energy of the most energetic particle, which is ^{6}Li in the ground state, is known and the time of flight of the slowest particle that can be unambiguously assigned is equal to the time of flight of ^{6}Li (g.s.) plus one RF period, hence depends on the bombarding energy of the protons and the flight distance. Increasing the flight distance will increase the low energy cutoff while decreasing the flight distance will decrease the low energy cutoff but worsen the time of flight resolution and hence the mass resolution. For this experiment the flight distance at 15 degrees laboratory angle is 28 cm. With this setup the low energy cutoff is about 0.6 to 1 MeV for mass 6, 7, and 10.

II.10 Accumulation of Data

At the beginning of every experiment the resolution of the electronic system was measured. It was always better than 40 KeV FWHM for 5.48 MeV alphas from an ^{241}Am source. Then a random time spectrum was taken. This is done by using the pulser (ORTEC 204) to simulate particle pulses and the RF pulses as the stop pulses. Since the frequencies of the RF and the pulser are so different then the time length measured are essentially randomly distributed on the nanosecond scale from the minimum length (25 ns) to the maximum (1 RF period + 25 ns). A random time spectrum assures that the TAC is operating beyond its non-linear region which is 15% of the range setting.

Next the width of the proton beam burst was measured. It was found to vary from one experiment to another in a range from 0.4 to 0.6 nsec. FWHM.

Now the beam is sent to the target and the mass spectrum is studied by displaying the mass bands on Time-Energy axes using the EDE routine of the program TOOTSIE (Ba 70). Energy gain is adjusted to make sure that all particles are detected by positioning the ^{6}Li ground state peak to the most right side of the energy axis. Also the discriminator level of the TPC is adjusted to insure that it triggers for every energy pulse detected. Then the delay of the RF pulse train is adjusted such that the fastest particle of interest (^{6}Li) corresponds to the longest time signal since $T_S = T_{RF} - T_{flight}$ + constant. This can be checked by looking at the spectrum (see Figure II.6).

The last step is to switch to the ET^2 routine of TOOTSIE which will calculate $M = A + E(T_s - T_o)^2/NORM$ where A, NORM, and T_o are constants to be input to the program. The constants were so chosen that the mass bands are as straight as possible. The display is on M - E energy axes (See Figure II.7).

The two-dimensional spectrum in Figure II.7 was taken at 15° with 40 MeV proton bombarding energy. The low energy cutoff here is a straight line, it corresponds to a constant time signal--the minimum time signal.

At every angle where a measurement was taken a background run was also taken. The background was measured by evacuating the gas cell and sending the beam through it. The amount of beam used was, in most cases, 25% of the integrated charge used to measure the foreground.

The data were collected and stored on both cards and magnetic tapes for further analysis.

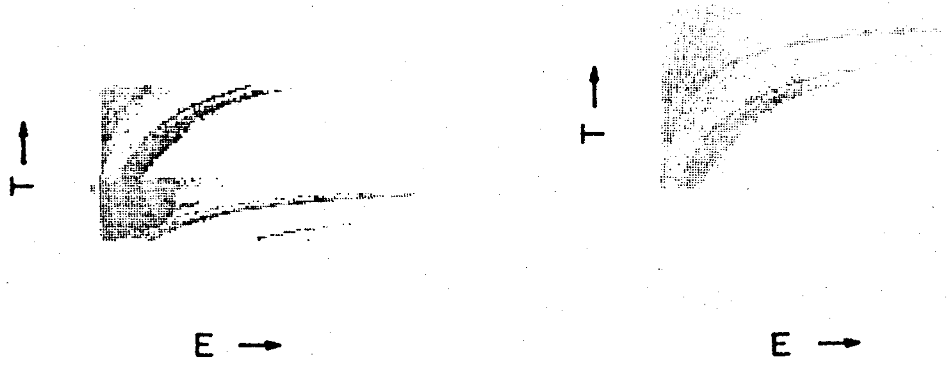

(a)

(b)

Fig. II.6.--Time-signal vs. Energy displays. (a) Improper timing (of arrival of stop pulses). (b) Proper timing.

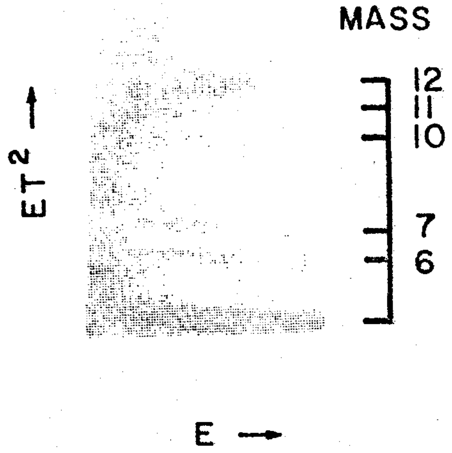

Fig. II.7.--Mass bands display.

Chapter III

DATA ANALYSIS

III.1 Normalization of Data

The raw data is corrected for the dead time of the ADC's during which the ADC's do not accept pulses. This is done by sending one of the pulses coming from the monitor detector to a scaler and on to channel zero of the ADC's. The ratio between the count in channel zero and the scaler gives the fraction of the time during which the ADC's are accepting the data. The background data have been multiplied by the ratio of the integrated charges during the data taking and the background run.

The area under the elastic peak of the monitor spectrum has been found by using the program SAMPO. Together with the integrated charge of each run during the data taking and the pressure of the gas target measured during the run the ratio of the counts in the peak to the product of the pressure and the integrated charge for each run agrees to within 3 to 4% as is shown in Appendix C.

III.2 Mass Spread

Each mass band is comprised of particles distributed along the mass axis at various energies. At each energy a mass resolution can be assigned.

From the two dimensional spectrum it is seen that the mass resolution $(\frac{\Delta M}{M})$ for each band is worse in the low energy region. The band of lighter mass is better resolved than the ones for heavier masses. This is probably due to the poorer energy resolution for heavy particles in that energy region and the time width of the beam burst.

Energy E and the time of flight T are the two parameters measured. TOOTSIE calculates the product ET^2 (in arbitrary units) which is proportional to the mass M of the particle.

A spread in E and T will then determine the spread of M as follows:

$$\Delta(ET^2) = \left[\Delta E^2 (T^2) + 4E^2T^2(\Delta T)^2\right]^{1/2}$$

$$\frac{\Delta M}{M} = \frac{\Delta(ET^2)}{ET^2} = \left[\left(\frac{\Delta E}{E}\right)^2 + 4\left(\frac{\Delta T}{T}\right)^2\right]^{1/2}$$

ΔE: being the energy resolution of the detecting system

ΔT: is the time resolution for the time length corresponding to the time of flight of particles within the energy range $E-\frac{\Delta E}{2}$ to $E+\frac{\Delta E}{2}$.

The time spread ΔT is primarily due to the time shifts for the start pulses associated with a group of energy pulses $(E - \frac{\Delta E}{2})$ to $(E + \frac{\Delta E}{2})$ coming from different points in the targets. There are three contributing causes:

1. Pulses associated with particles of the same mass and energy traveling through different path lengths.

2. Pulses associated with particles of the same mass but slightly different energies that cause time shifts in the output of the time pickoff unit.

3. Time spread due to the finite width of the proton beam bursts.

The first contribution can be calculated from the energy formula, where

$$\frac{\Delta T}{T} = \frac{\Delta D}{D} \text{ (D = flight path)},$$

where ΔD depends on angle as is seen in Figure III.1. At 17° scattering angle the length ACD is 0.19 in.

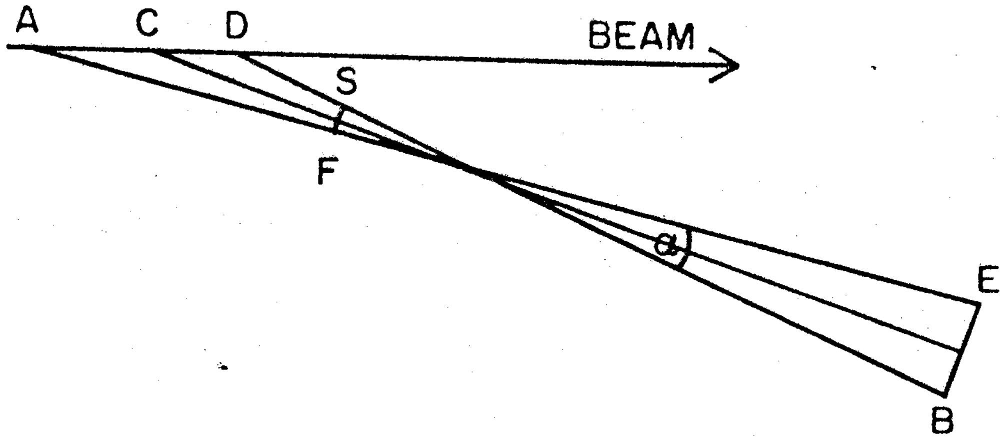

Fig. III.1.--Schematic Drawing of Different Path Lengths. FS = Front Slit, BE = Rear Aperture; α = 1°.

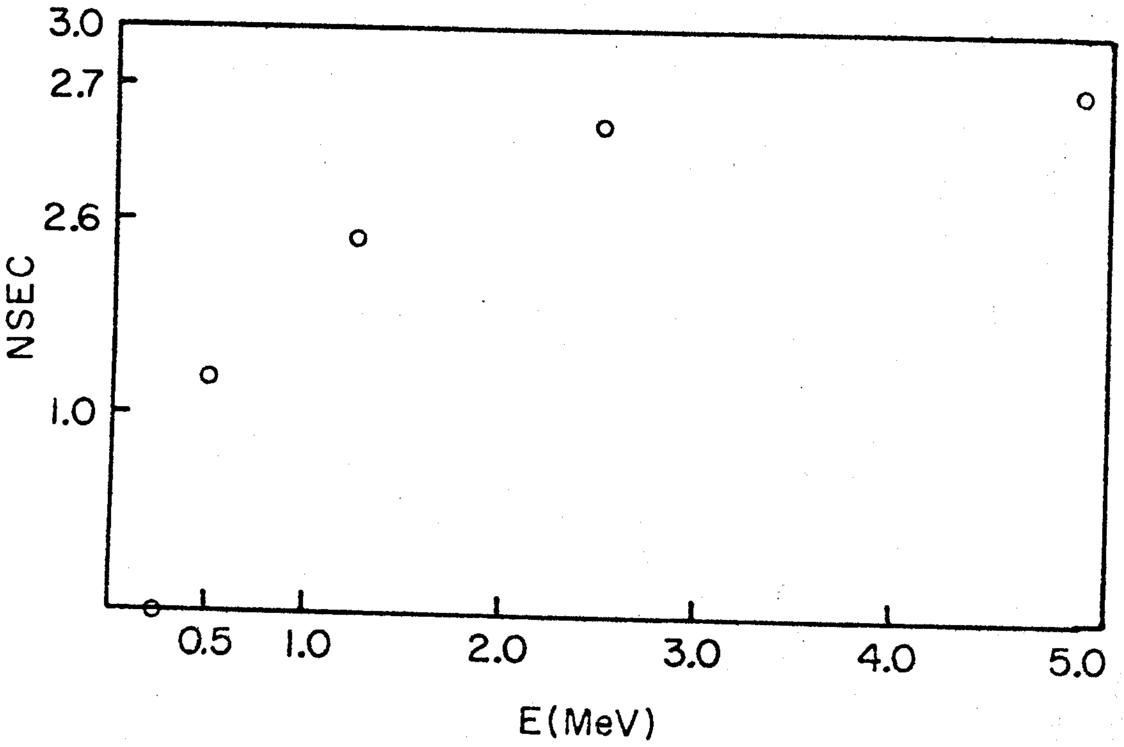

Fig. III.2.--Time Shift (nsec.) of the TPU Output as a Function of Energy.

The second contribution is important only for energies lower than 5 MeV (see Figure III.2), while the third contribution is measured and its value ranges from 0.4 nsec. to 0.6 nsec. FWHM.

Adding these contributions in quadrature the band resolution at energy E is calculated according to:

$$\frac{\Delta(ET^2)}{ET^2} = {\left(\frac{\Delta E}{E}\right)^2 + 4\left(\frac{\Delta D}{D}\right)^2 + 4\left(\frac{\Delta T_{BEAM}}{T}\right)^2 + 4\left(\frac{\Delta T_{TPU}}{T}\right)^2}^{1/2}$$

(see Appendix D), the result of which for 5.5 MeV particles at 17° scattering angle are tabulated in Table III.1.

TABLE III.1.--Mass Resolution for 5.5 MeV Particles; E_p = 40 MeV, D = 28 cm, Scattering Angle = 17°, Front Slit = 0.425 in., Beam Width = 0.5 nsec.

Particles	$\left(\frac{\Delta E}{E}\right)^2$ (%)^2	$4\left(\frac{\Delta D}{D}\right)^2$ (%)^2	$4\left(\frac{\Delta T_{BEAM}}{T}\right)^2$ (%)^2	$\frac{\Delta(ET^2)}{ET^2}$(%)
^{6}Li	0.53	11.7	22.5	5.9
^{7}Li	0.53	11.7	19.3	5.6
^{10}B	0.53	11.7	13.5	5.1
^{11}B	0.53	11.7	12.3	5.0
^{12}C	0.53	11.7	11.2	4.8

As expected the mass resolution for high energy particles is largely determined by the time resolution; for lower energy particles it would be determined by the energy resolution. Geometry affects all particles in the same way.

For comparison the observed mass resolutions for mass 6 and 7 mentioned in Table III.1 are shown in Table III.2. The observed and the calculated mass resolutions agree to within 1%.

TABLE III.2.--Observed Mass Resolutions for Mass-6 and Mass-7 at 5.5 MeV; E_p = 40 MeV, Scattering Angle = 17°, D = 28 cm; Beam Width = 0.5 nsec.

Observed Mass Scale = 0.16 mass unit/channel.
Mass Resolution (FWHM) for:

Mass-6 = 2.5 channels
= 6.7%

Mass-7 = 2.5 channels
= 6.9%

Comparing the band separation for mass-6 and mass-7 which is (7-6)/7 or 14% with the calculated mass resolution from Table III.1 which are 6%, one expects that mass-6 and mass-7 should be well separated down to low energy region. Experimentally, however, it is not so. For mass-6 and mass-7 the separation is good down to 4 MeV while from there on to lower energy region it is smeared almost uniformly. After a thorough investigation it was concluded that it was due to the background events that covered the low mass region up to about mass-8 or mass-9 (therefore the background was subtracted). From the data at 17° scattering angle mentioned above it was found that the yield for mass-8 was only 3% of the yield for mass-7. Since there is no stable isotope with A = 8, it is not expected to have a large yield for mass-8, as it is the case with the data, and therefore the above conclusion is made.

In the higher mass region the bands are not well separated even as high as 5 MeV. In addition the bands seem to bend down in the very low energy part. The reason for it is not clearly understood but it is probably due to the incomplete charge collection in the E-detector that will cause a too-small energy signal, hence a too-small mass.

III.3 Yields Extraction

The 2-dimensional spectrum (ET^2 vs E) displaying the bands of masses detected during each run was read from tape and either displayed on the storage scope using the code TOOTSIE or was printed, giving the number of counts with a given set of values of E and ET^2, for closer inspection.

Starting from the high energy region the mass-6 or mass-7 band is chosen by tracing the position of ^{6}Li and ^{7}Li ground state that comes from the 2-body break-ups using their energies as identifications as are predicted by the program FASTKINE (written by Dr. R. A. Paddock in this laboratory). The upper and lower limits of each band are determined by drawing a straight line from the high energy region, then identified, to the low energy region.

By projecting each band on the energy axis, the energy distribution for each mass is obtained. Then the entire procedure is repeated to obtain the energy spectra for the background runs. The background spectrum is then normalized to the foreground spectrum and subtracted from it to form the net spectrum (see Figure III.3 and III.4).

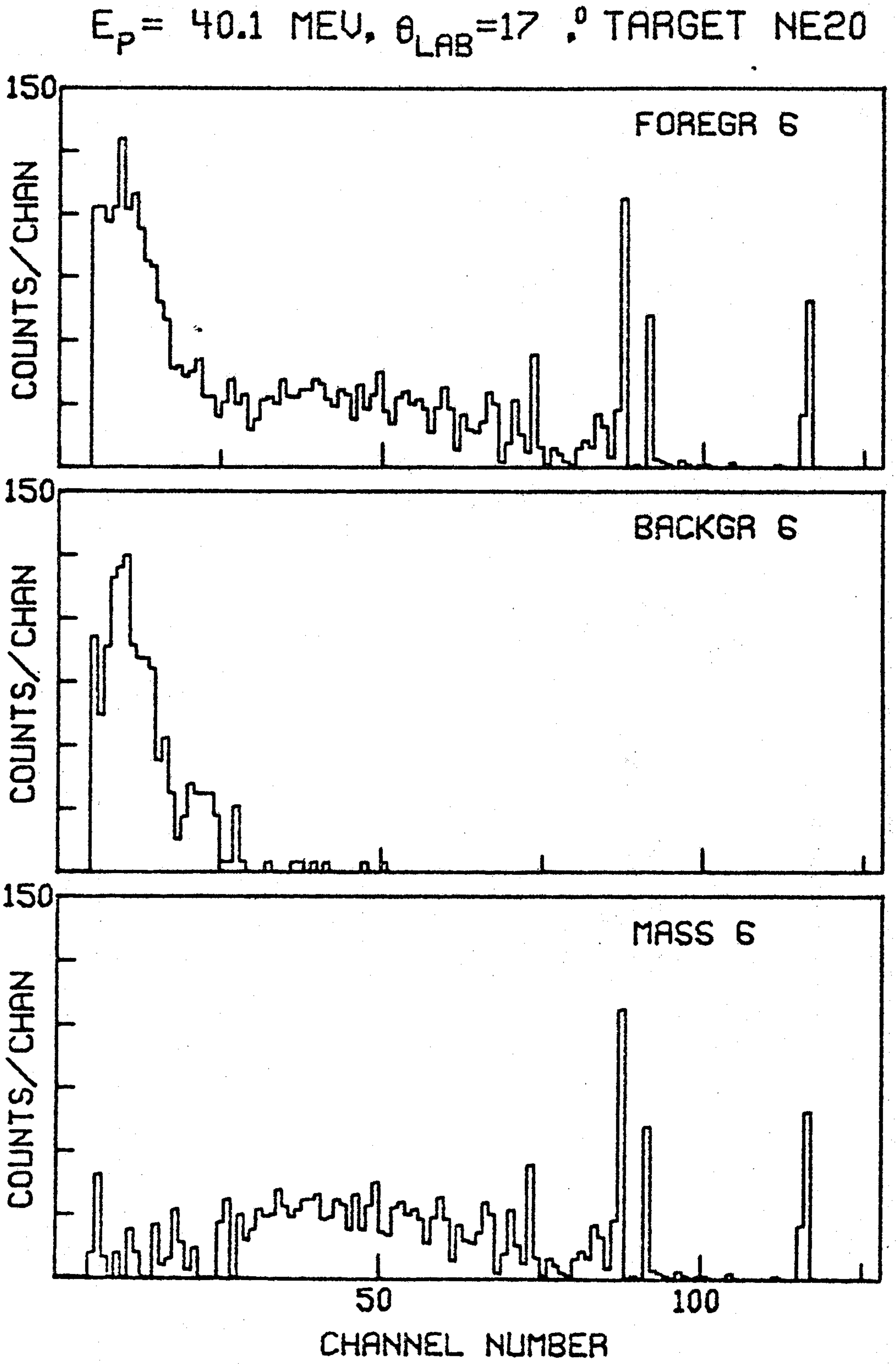

Fig. III.3.--Representative Spectra for the Foreground (Foregr), Background (Backgr) and Net (Mass) (0.18 MeV/channel).

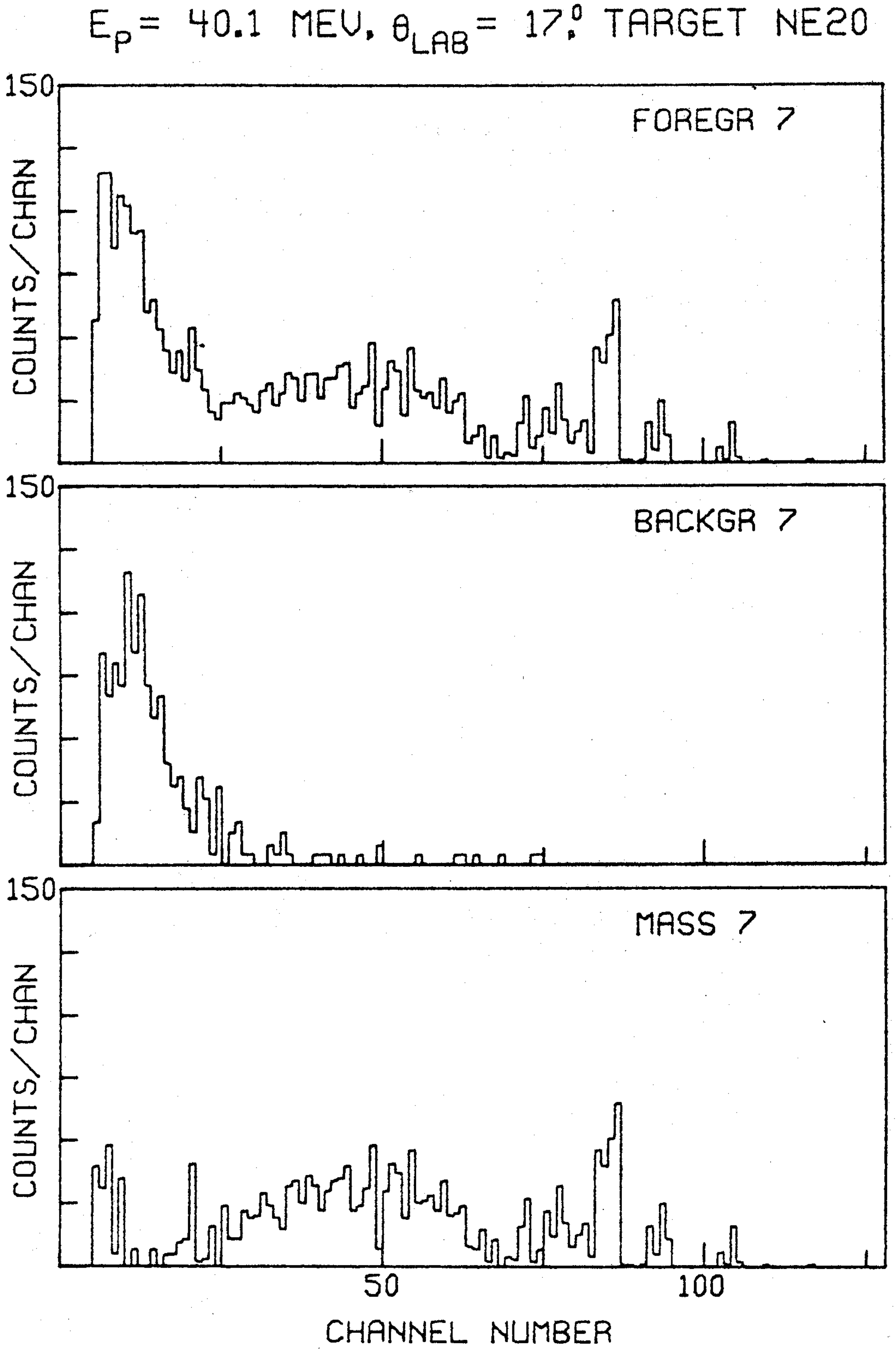

Fig. III.3.--(cont.) . . . . (0.18 MeV/Channel).

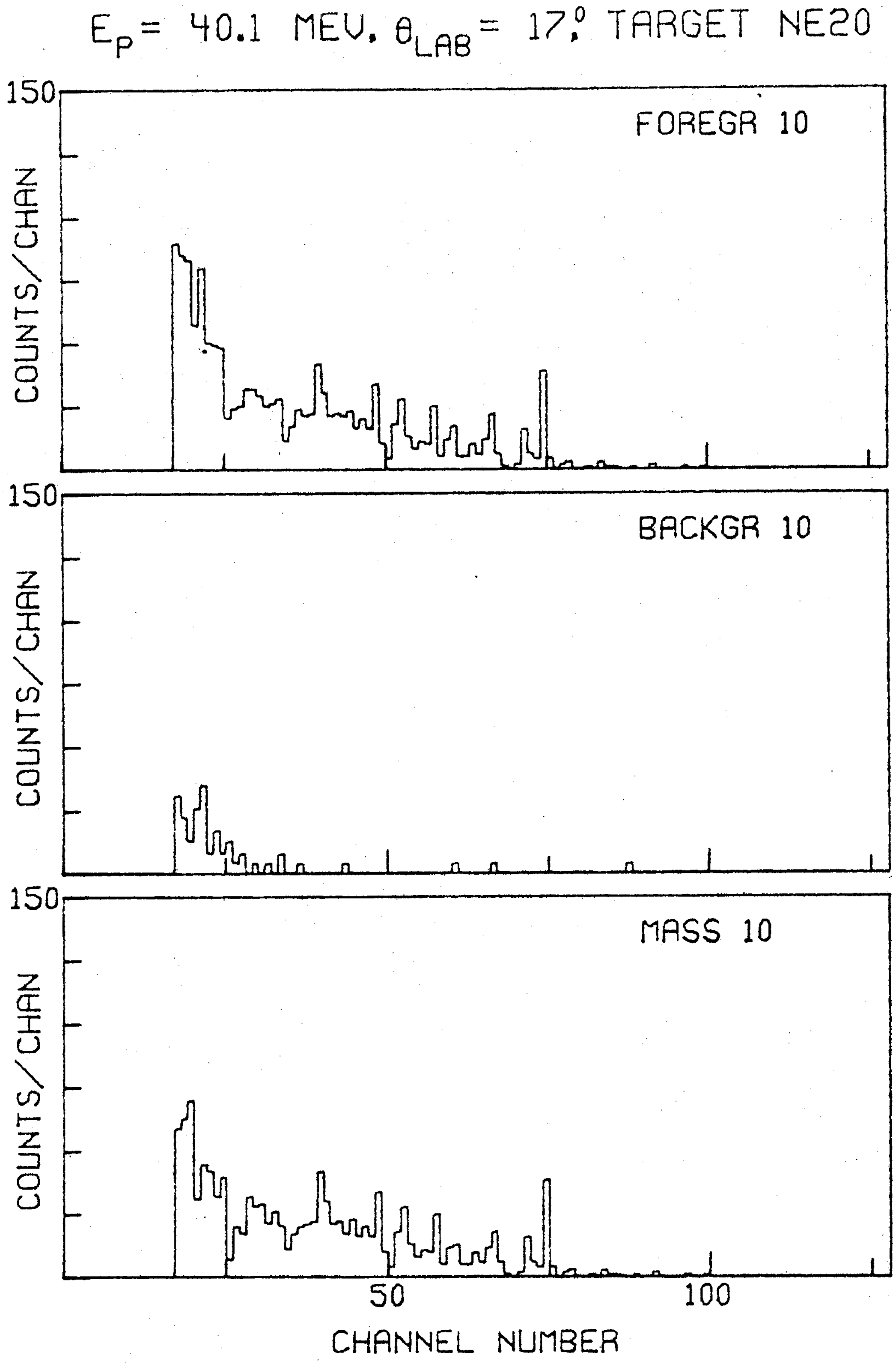

Fig. III.3.--(cont.) . . . (0.18 MeV/Channel).

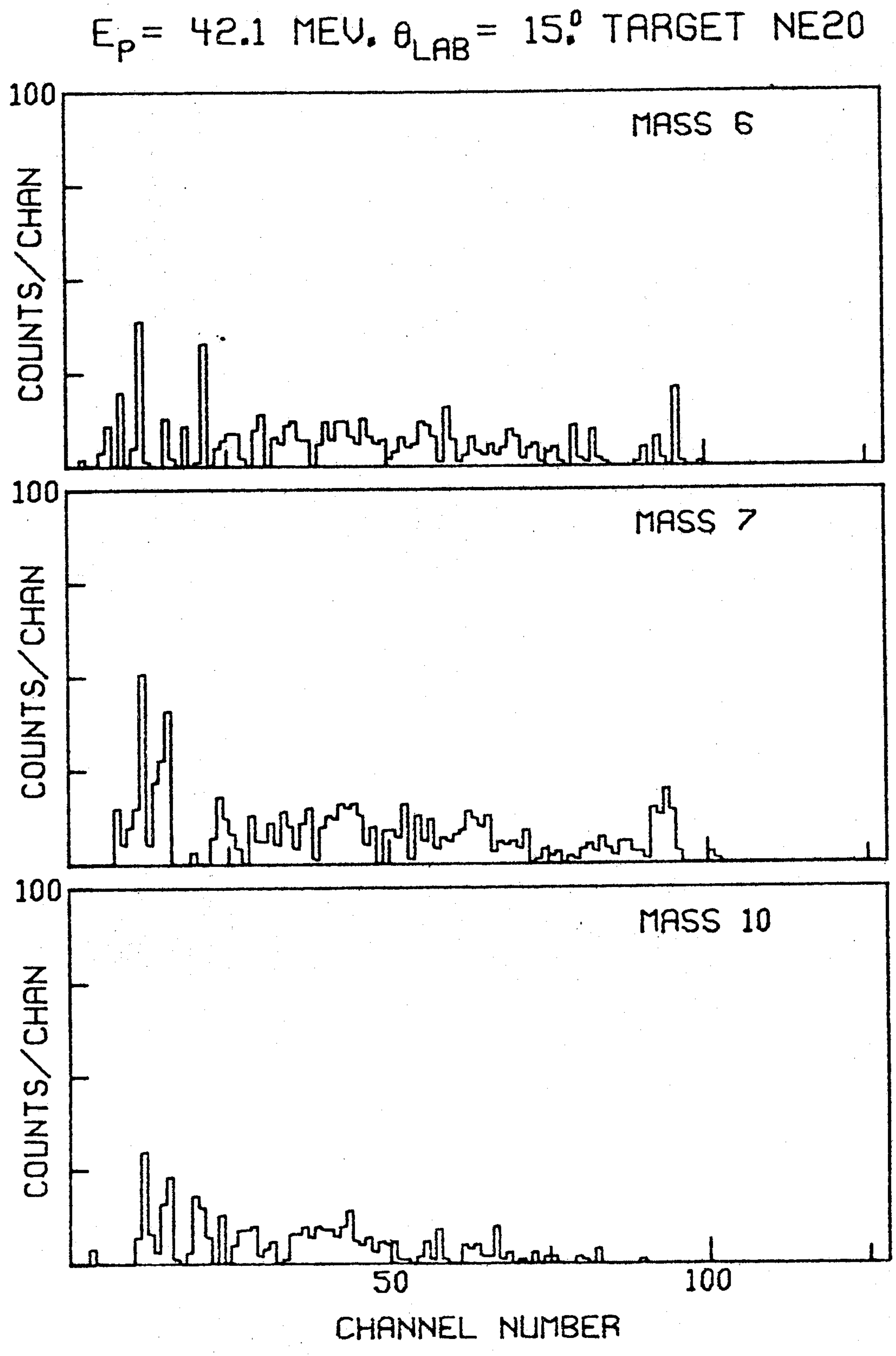

Fig. III.4.--Energy Spectra for Net Yields (0.17 MeV/channel).

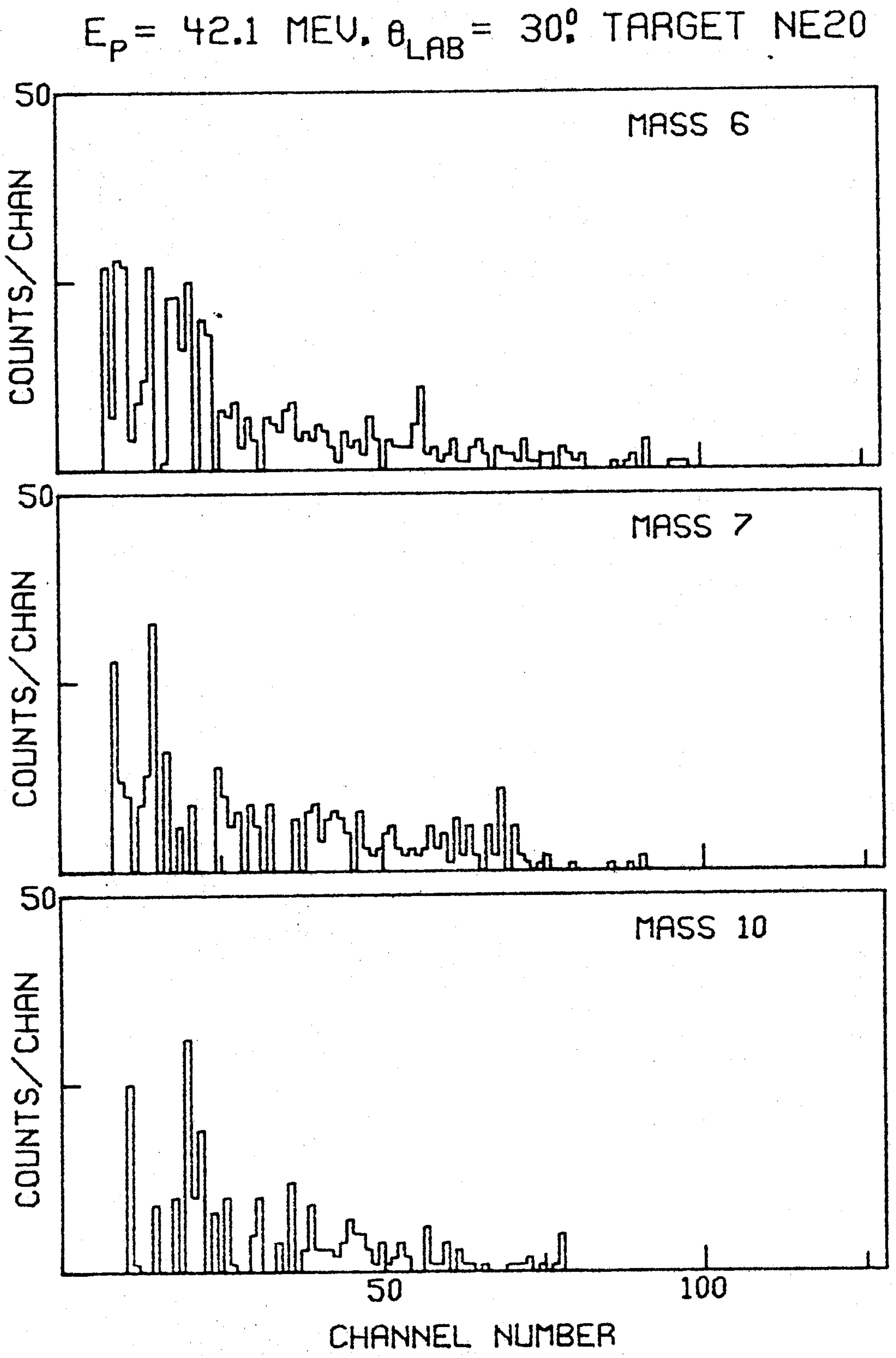

Fig. III.4.--(cont.) . . . (0.17 MeV/channel).

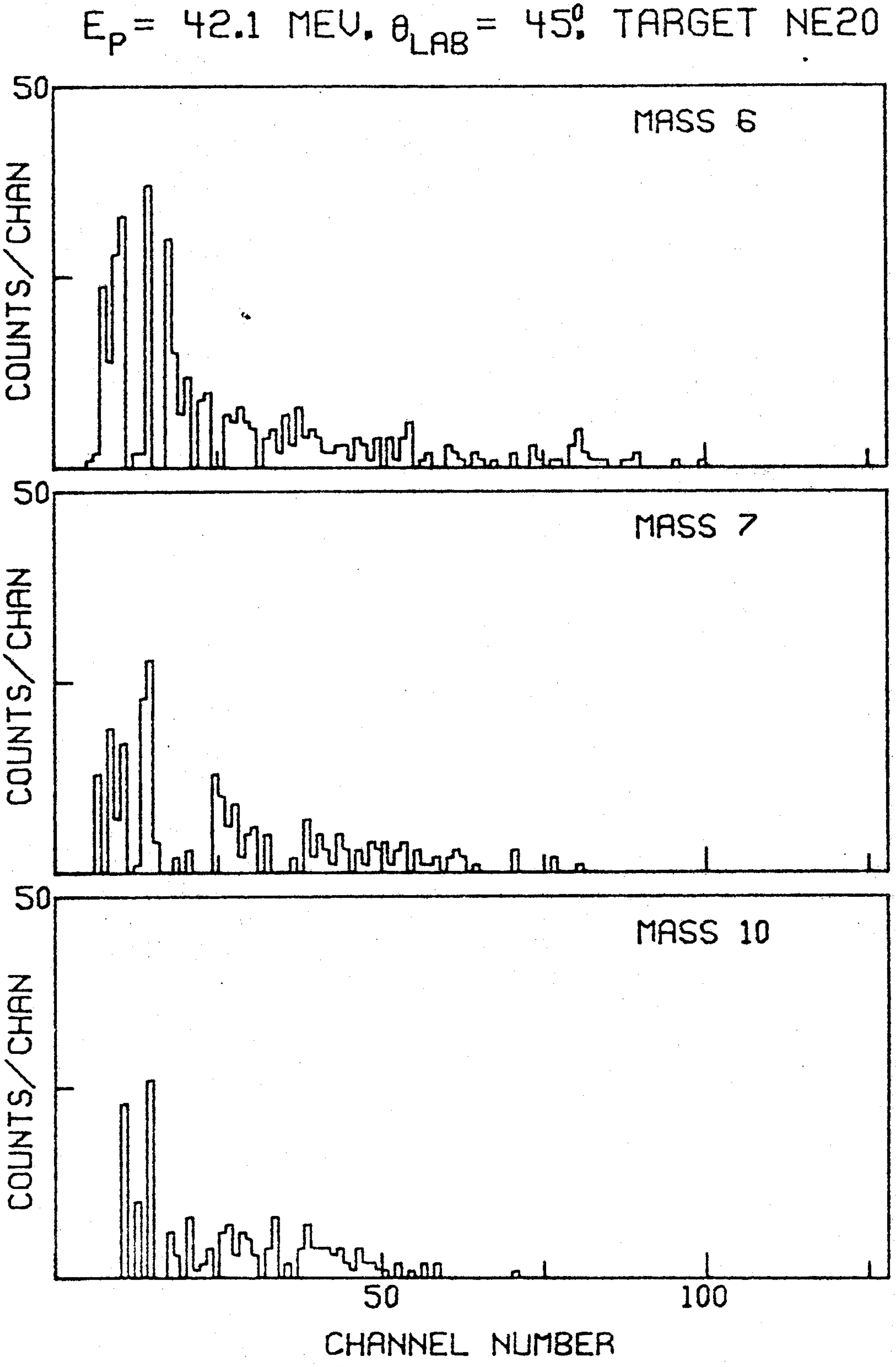

Fig. III.4.--(cont.) . . . (0.17 MeV/channel).

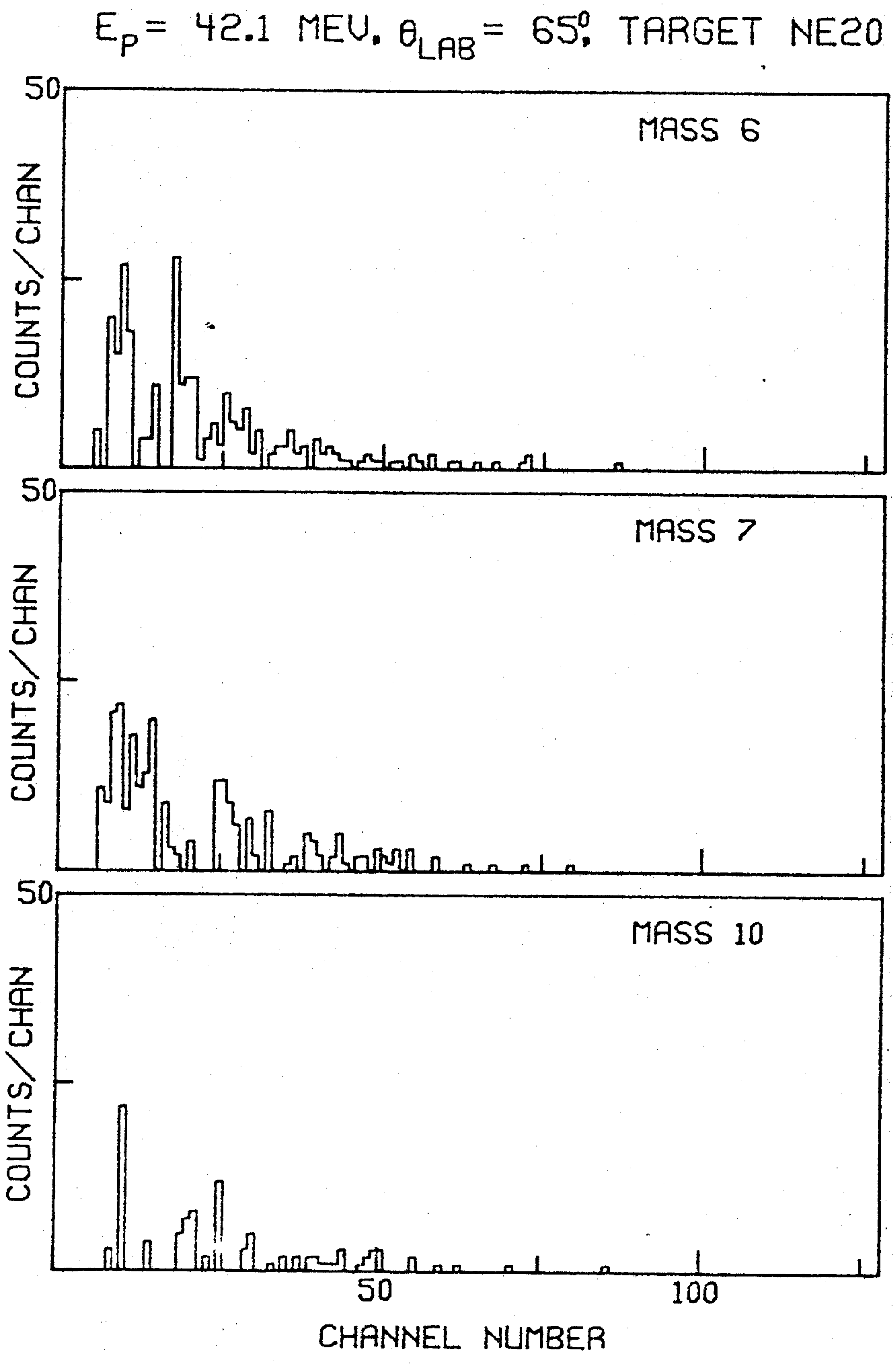

Fig. III.4.--(cont.) . . . (0.17 MeV/channel).

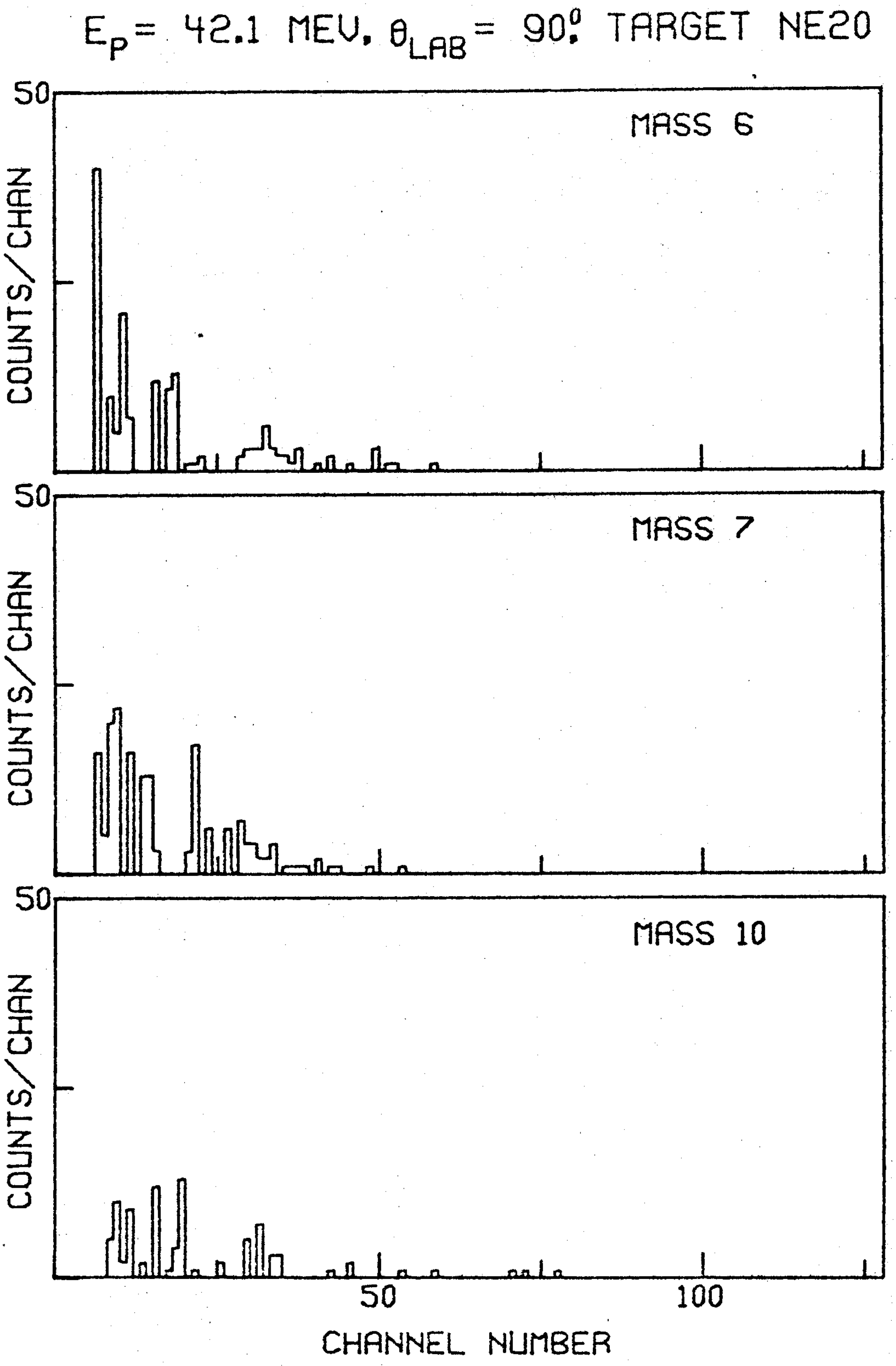

Fig. III.4.--(cont.) . . . (0.17 MeV/channel).

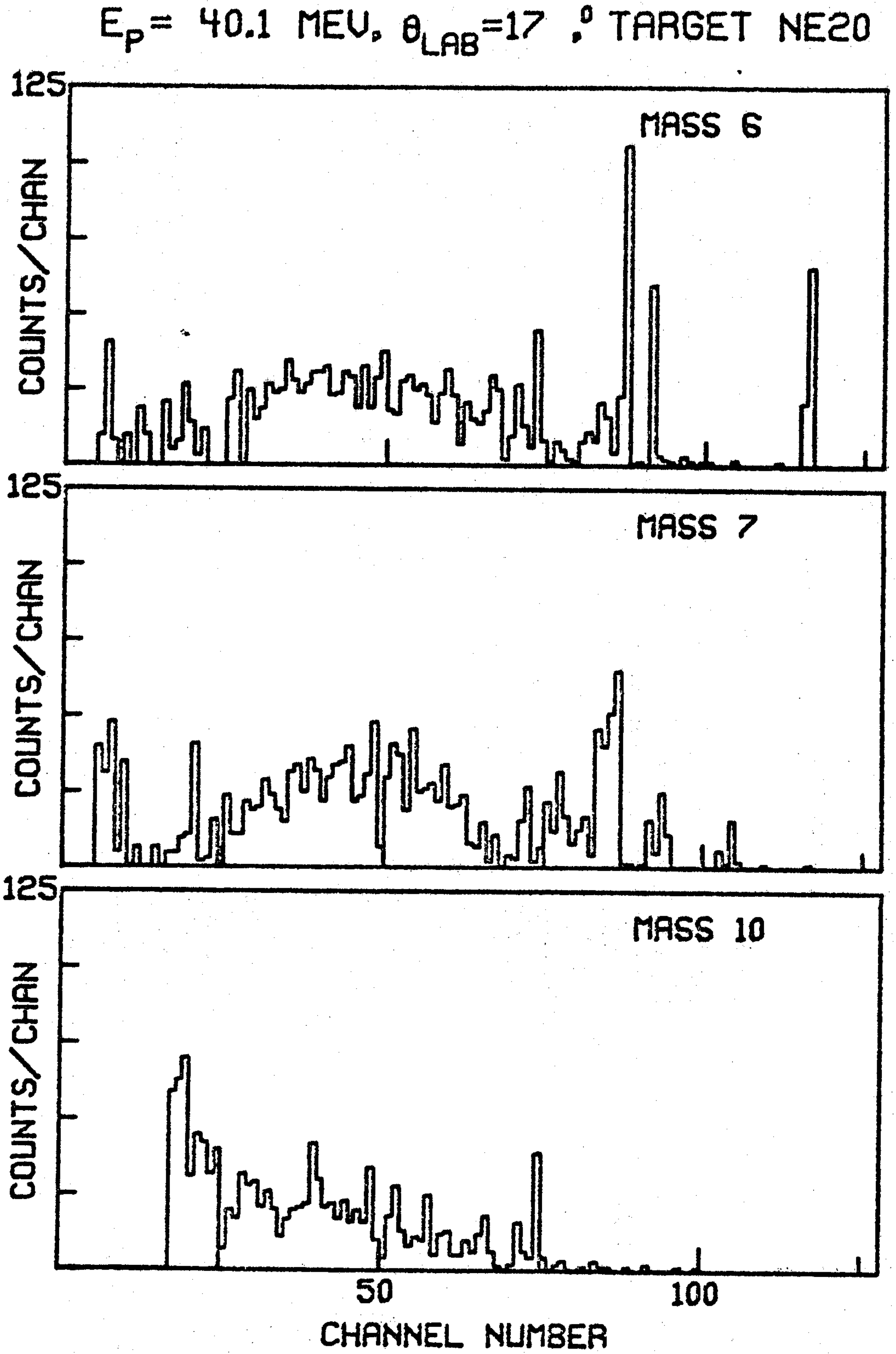

Fig. III.4.--(cont.) . . . (0.18 MeV/channel).

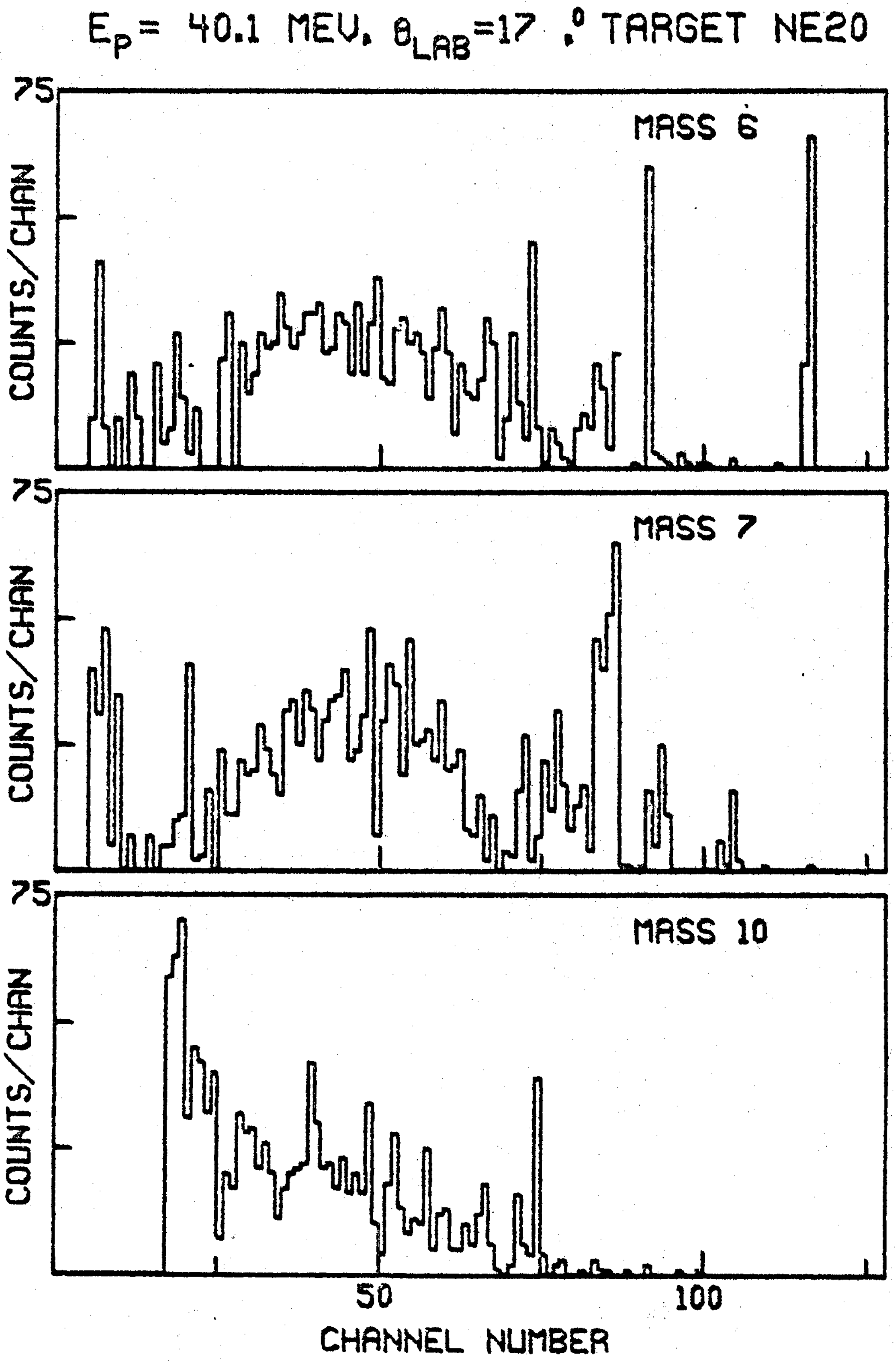

Fig. III.4.--(cont.) . . . (0.18 MeV/channel).

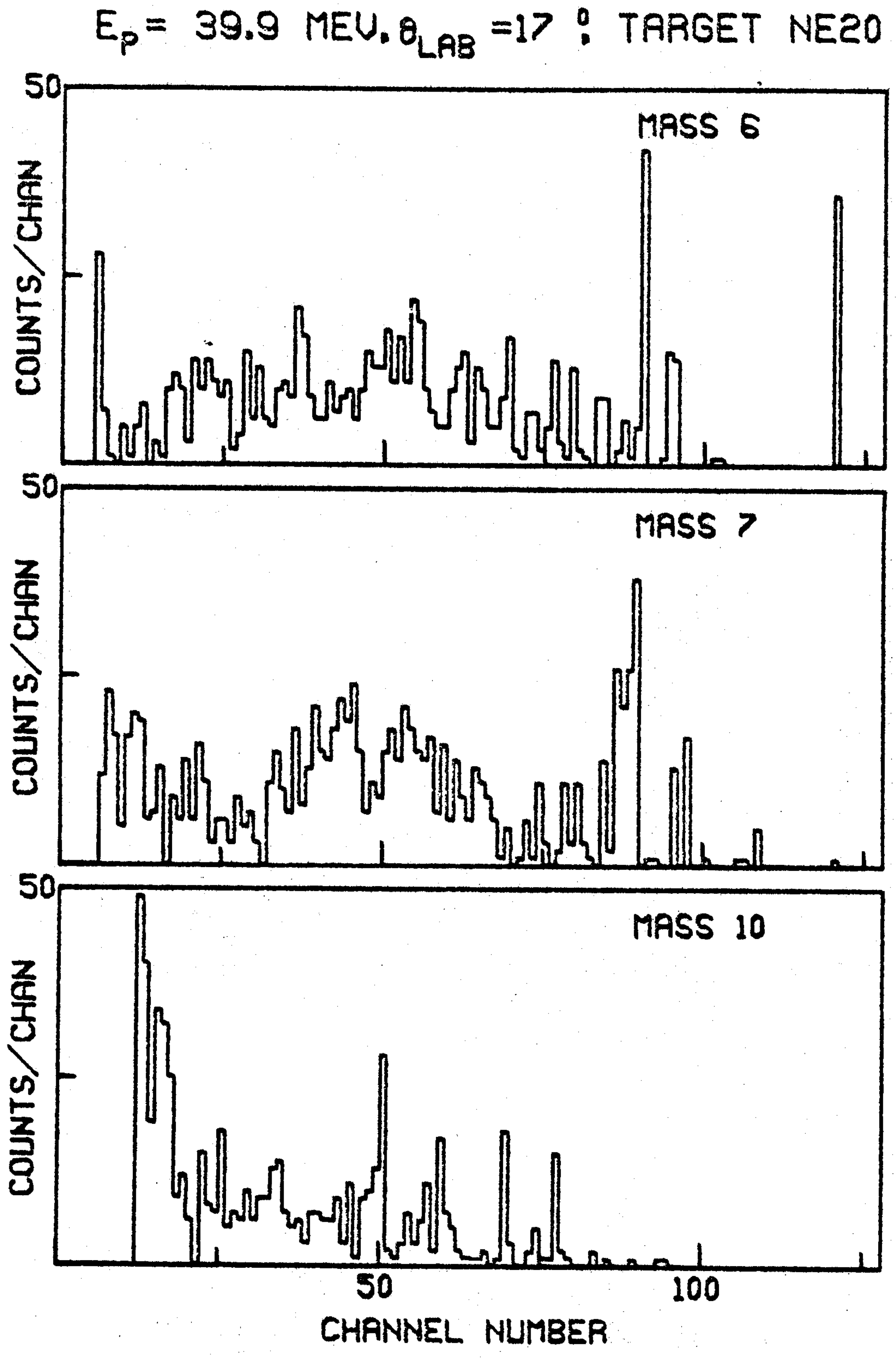

Fig. III.4.--(cont.) . . . (0.18 MeV/channel).

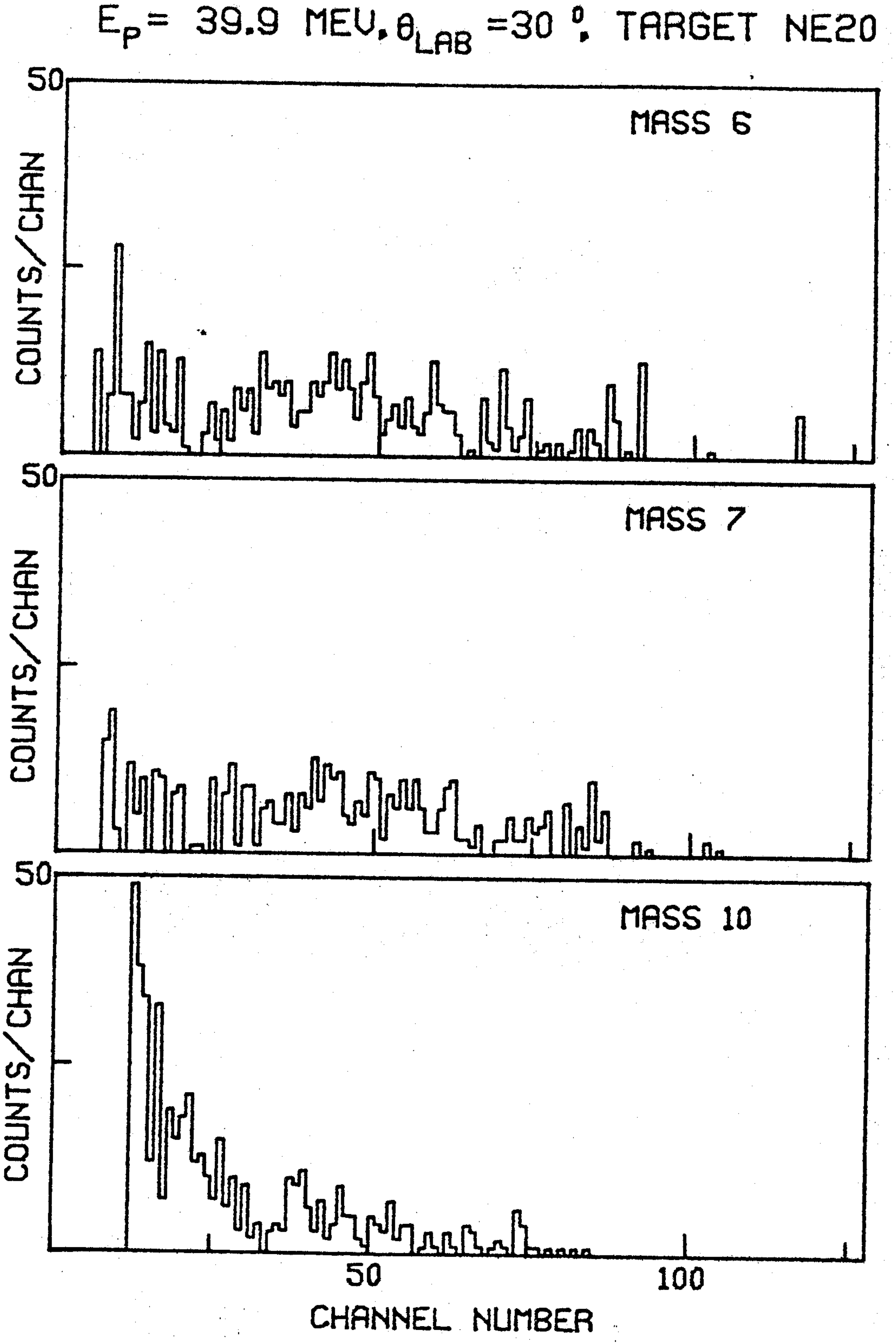

Fig. III.4.--(cont.) . . . (0.18 MeV/channel).

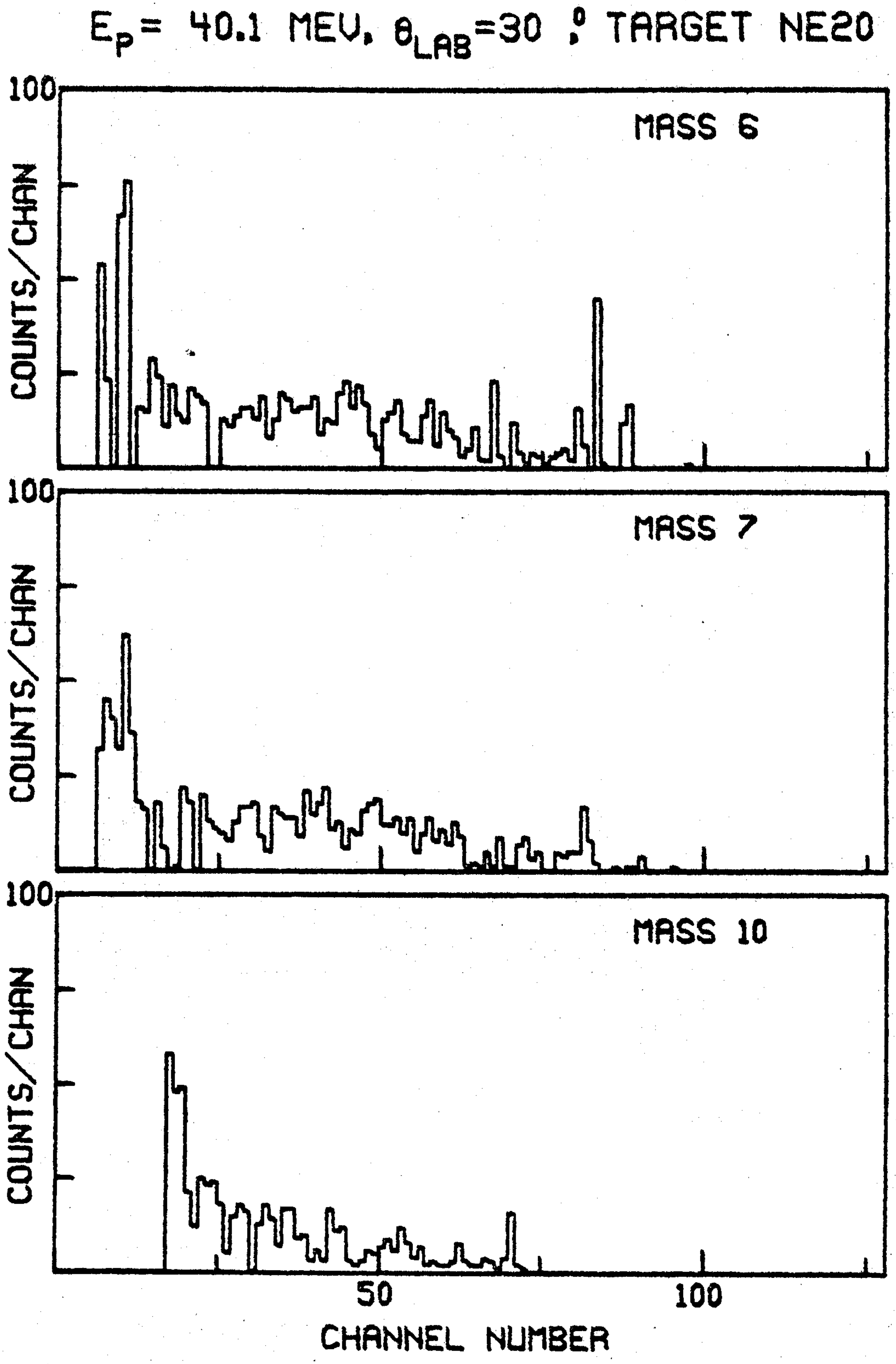

Fig. III.4.--(cont.) . . . . (0.18 MeV/channel).

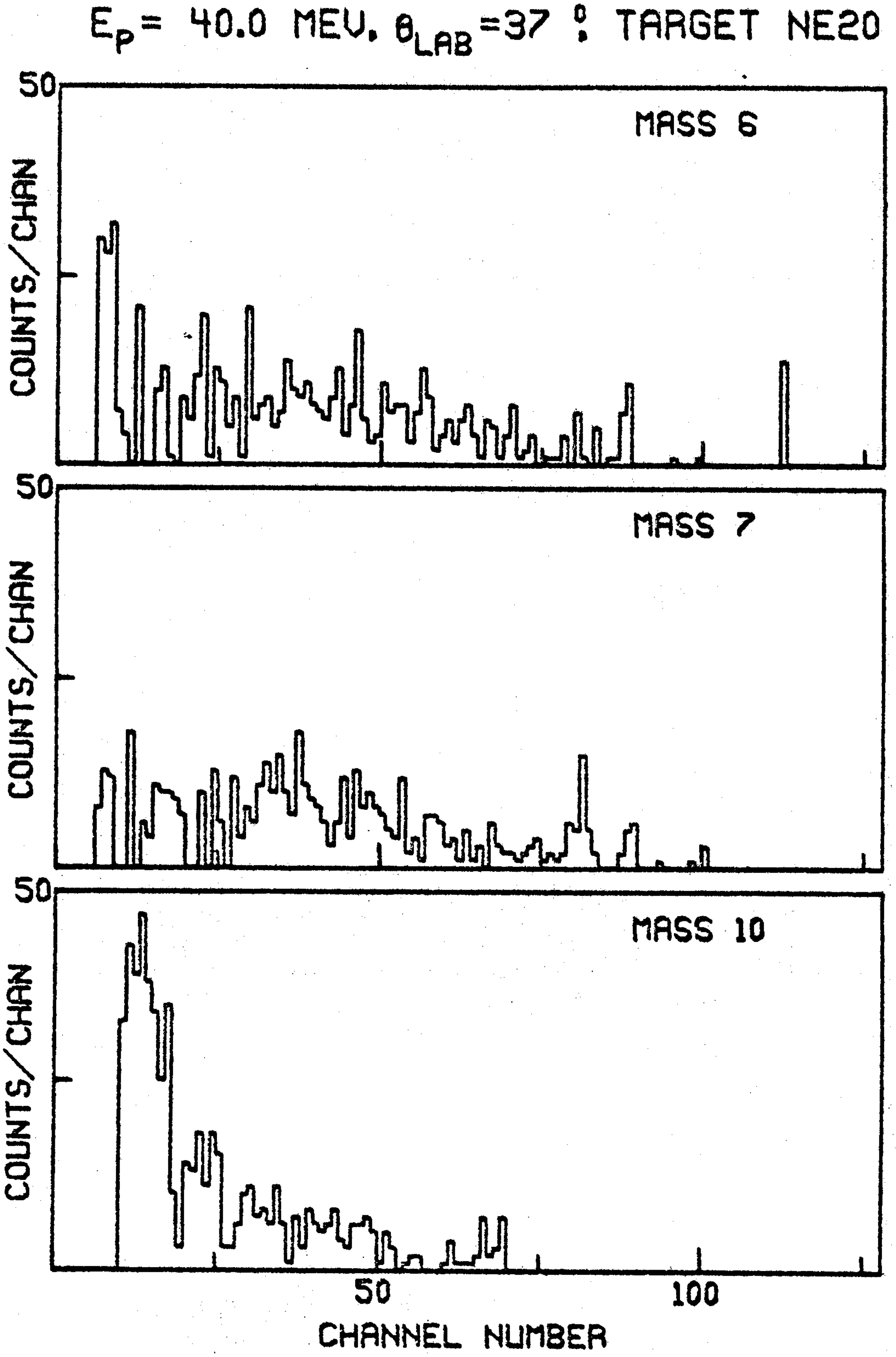

Fig. III.4.--(cont.) . . . (0.18 MeV/channel).

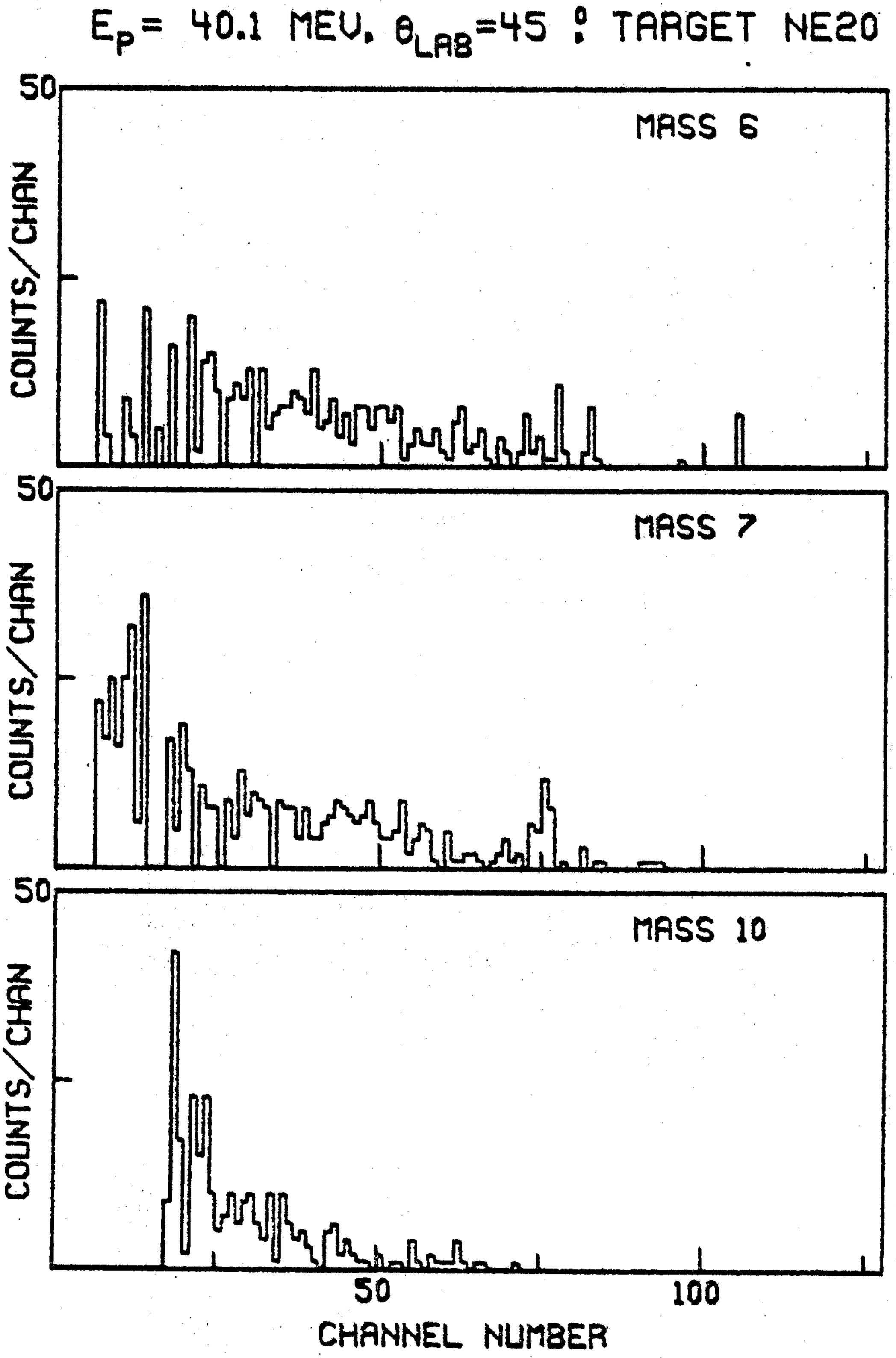

Fig. III.4.--(cont.) . . . (0.18 MeV/channel).

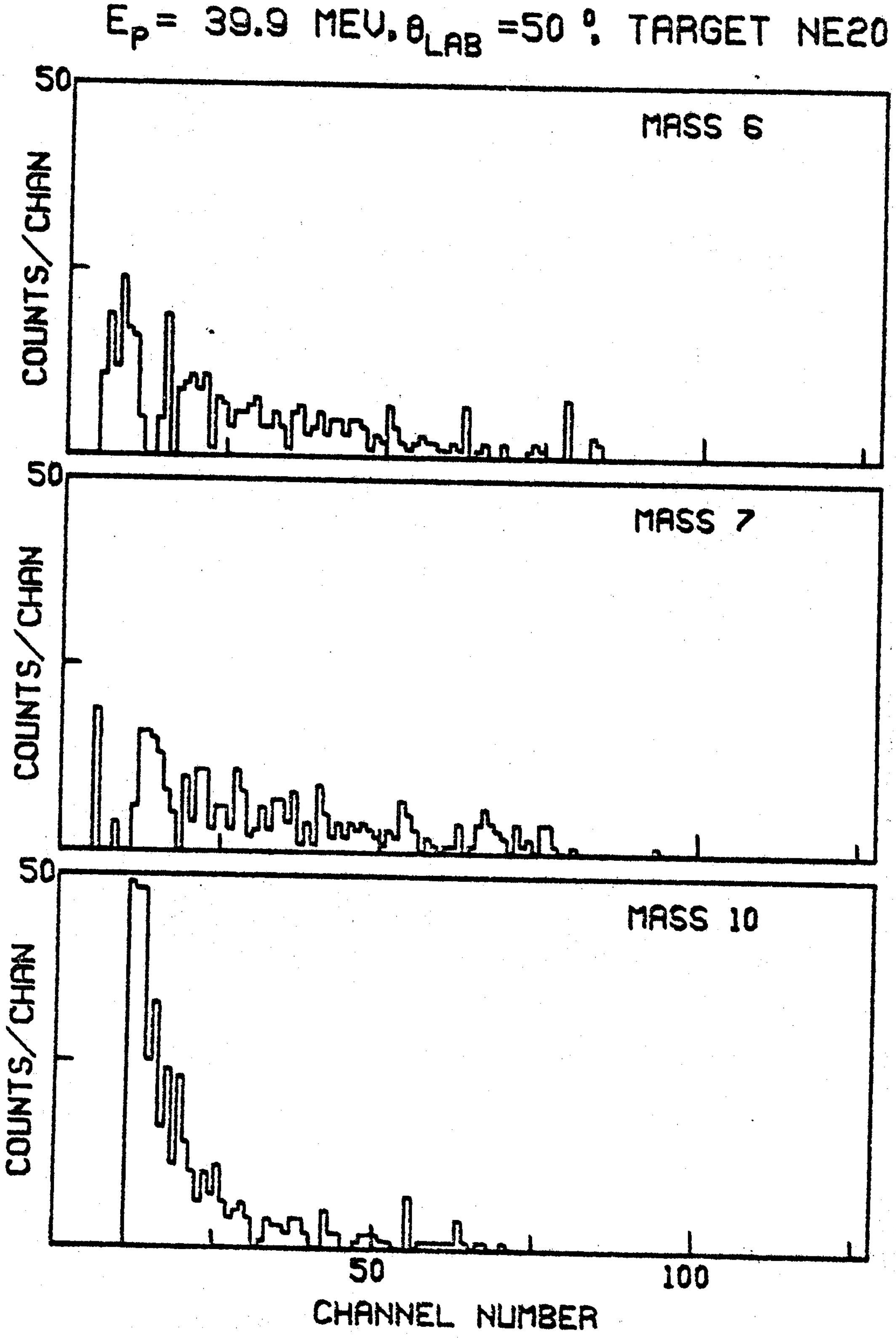

Fig. III.4.--(cont.) . . . (0.18 MeV/channel).

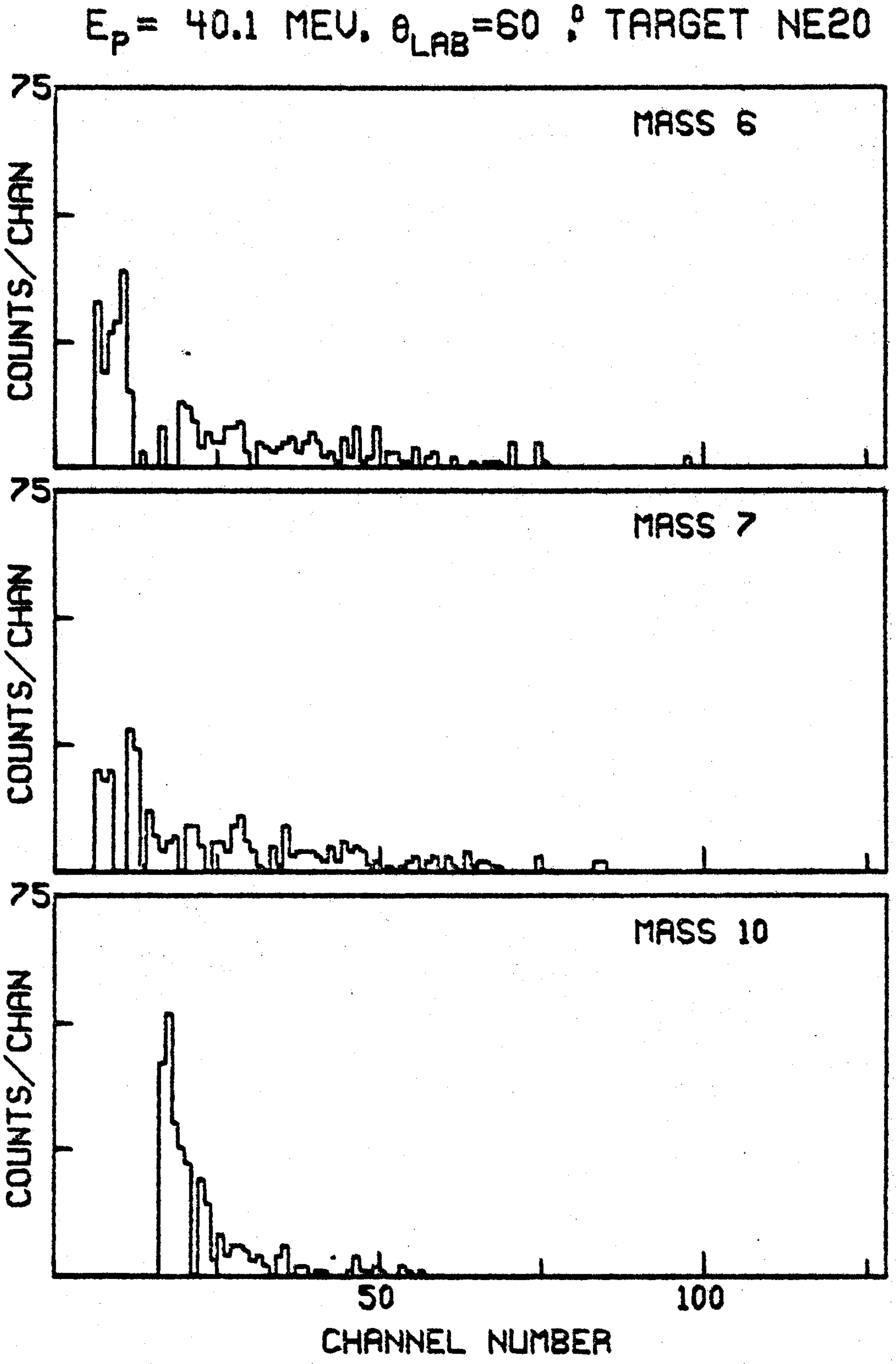

Fig. III.4.--(cont.) . . . (0.18 MeV/channel).

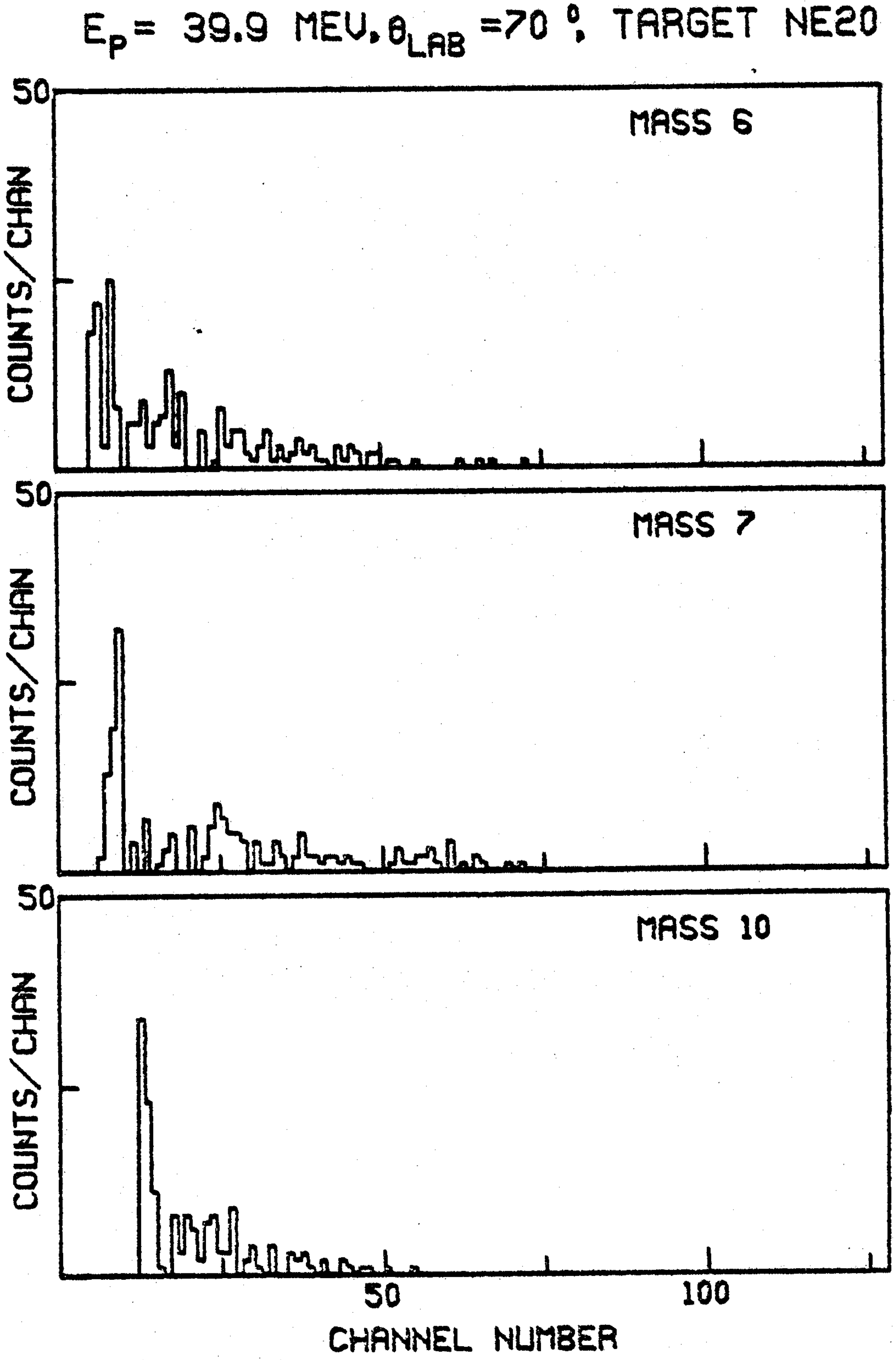

Fig. III.4.--(cont.) . . . (0.18 MeV/channel).

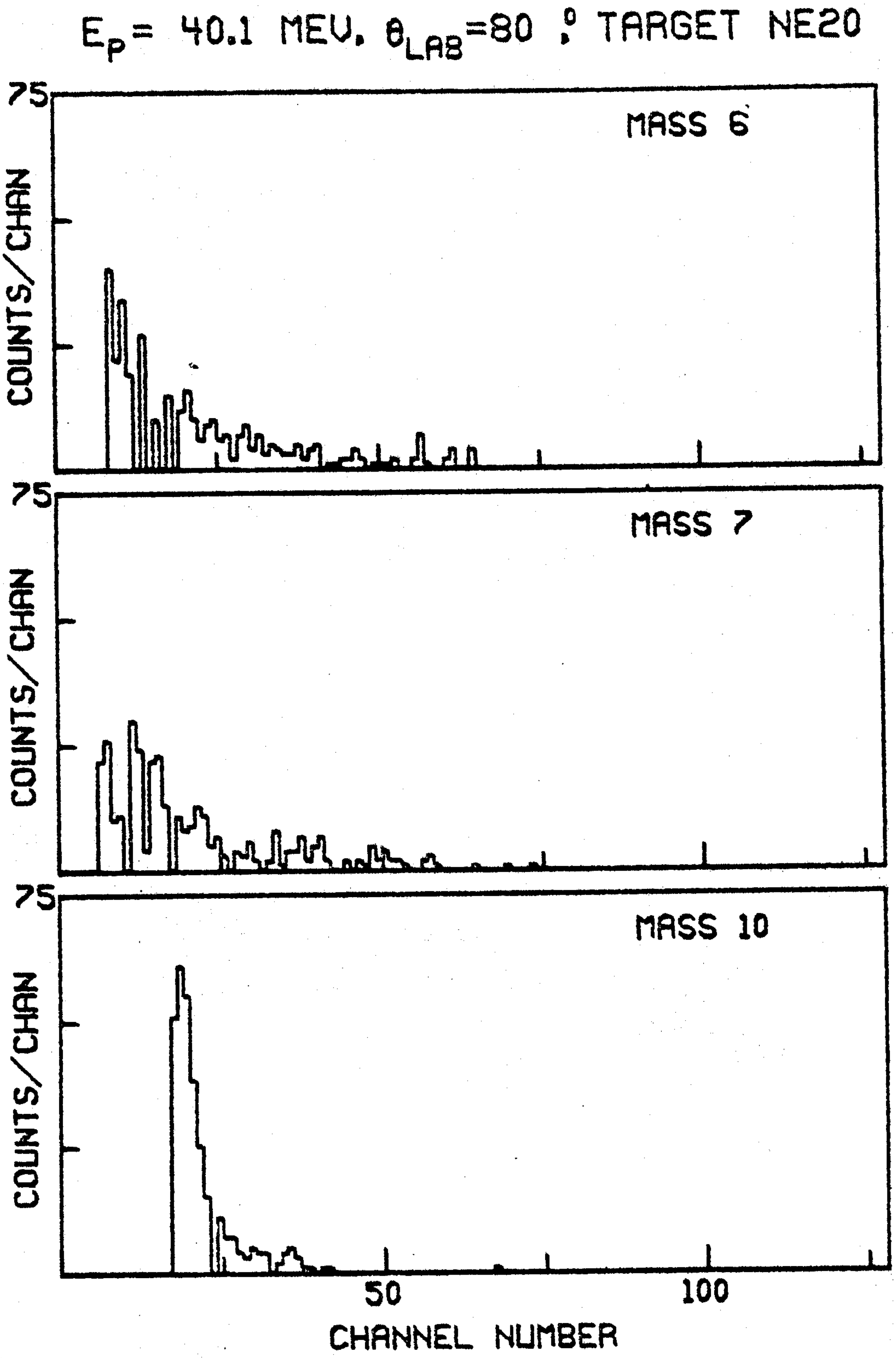

Fig. III.4.--(cont.) . . . (0.18 MeV/channel).

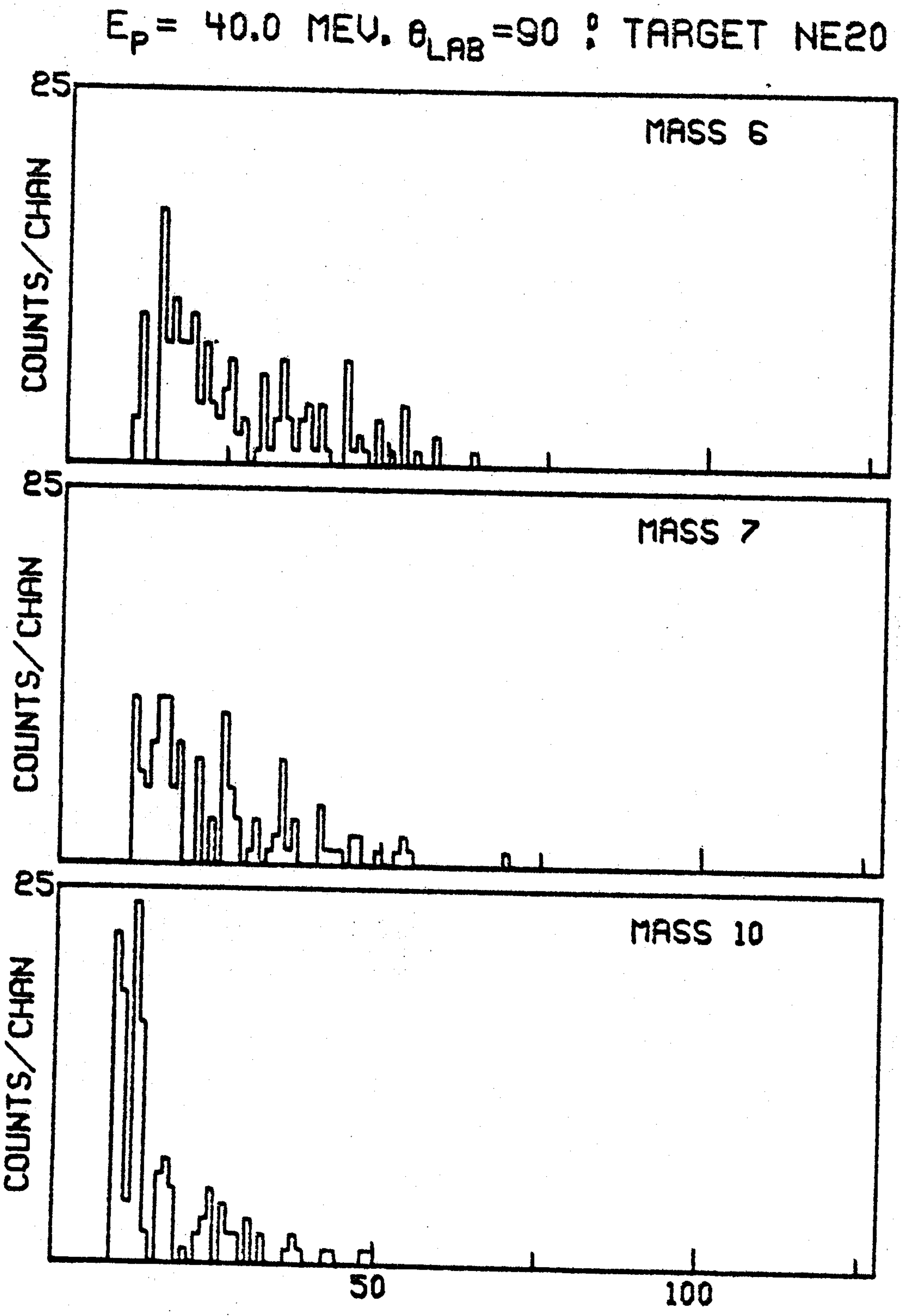

Fig. III.4.--(cont.) . . . (0.18 MeV/channel).

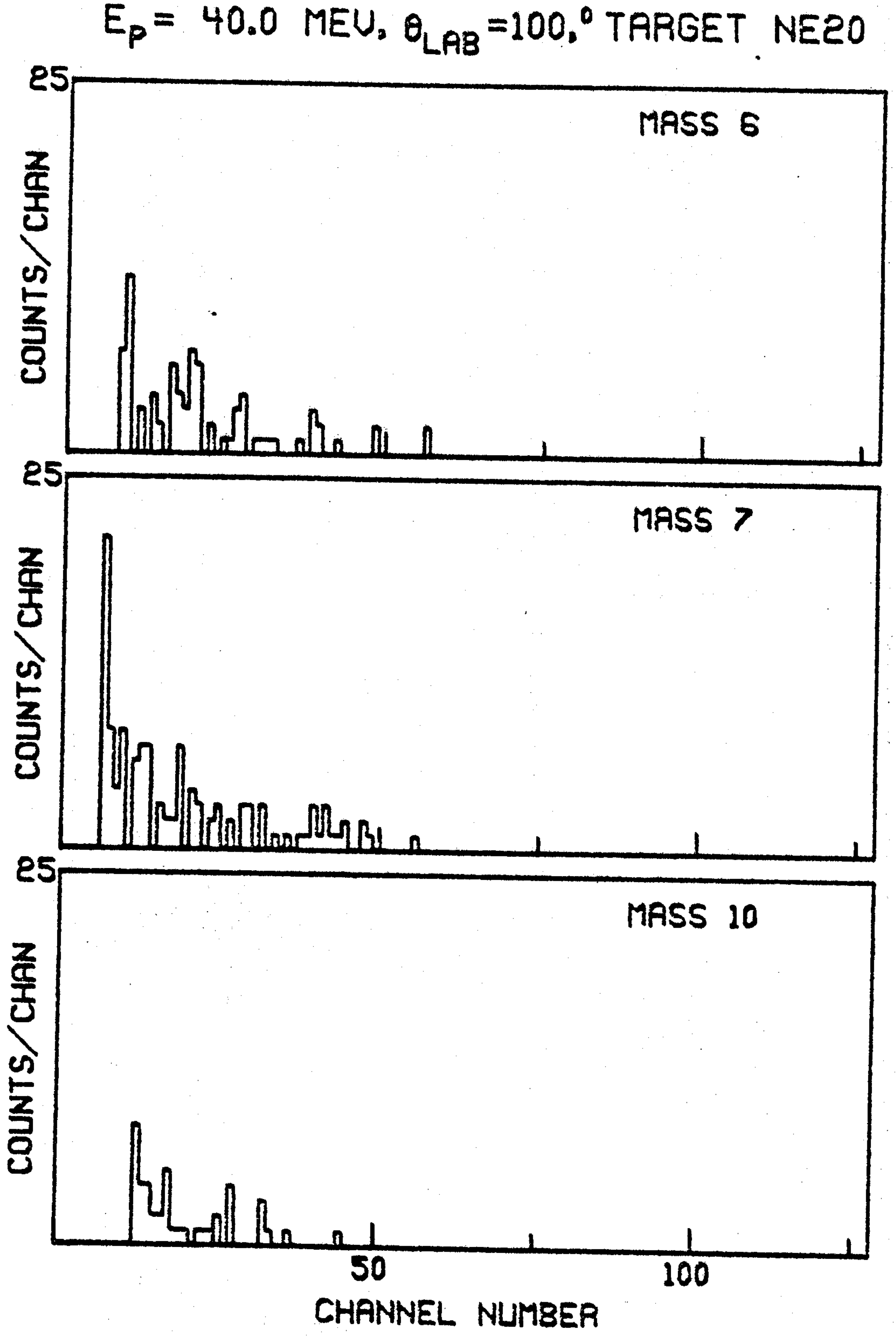

Fig. III.4.--(cont.) . . . (0.18 MeV/channel).

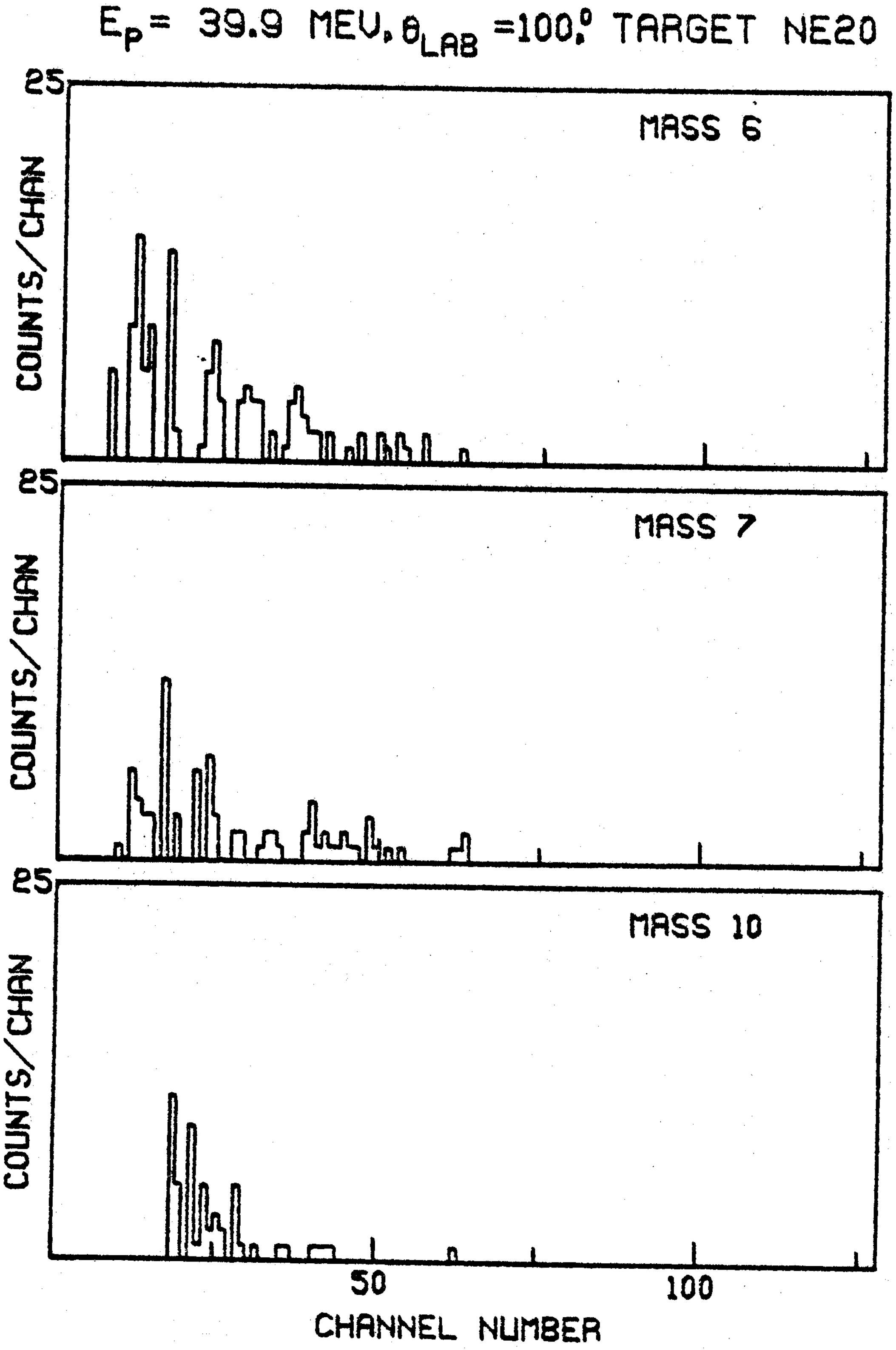

Fig. III.4.--(cont.) . . . (0.18 MeV/Channel).

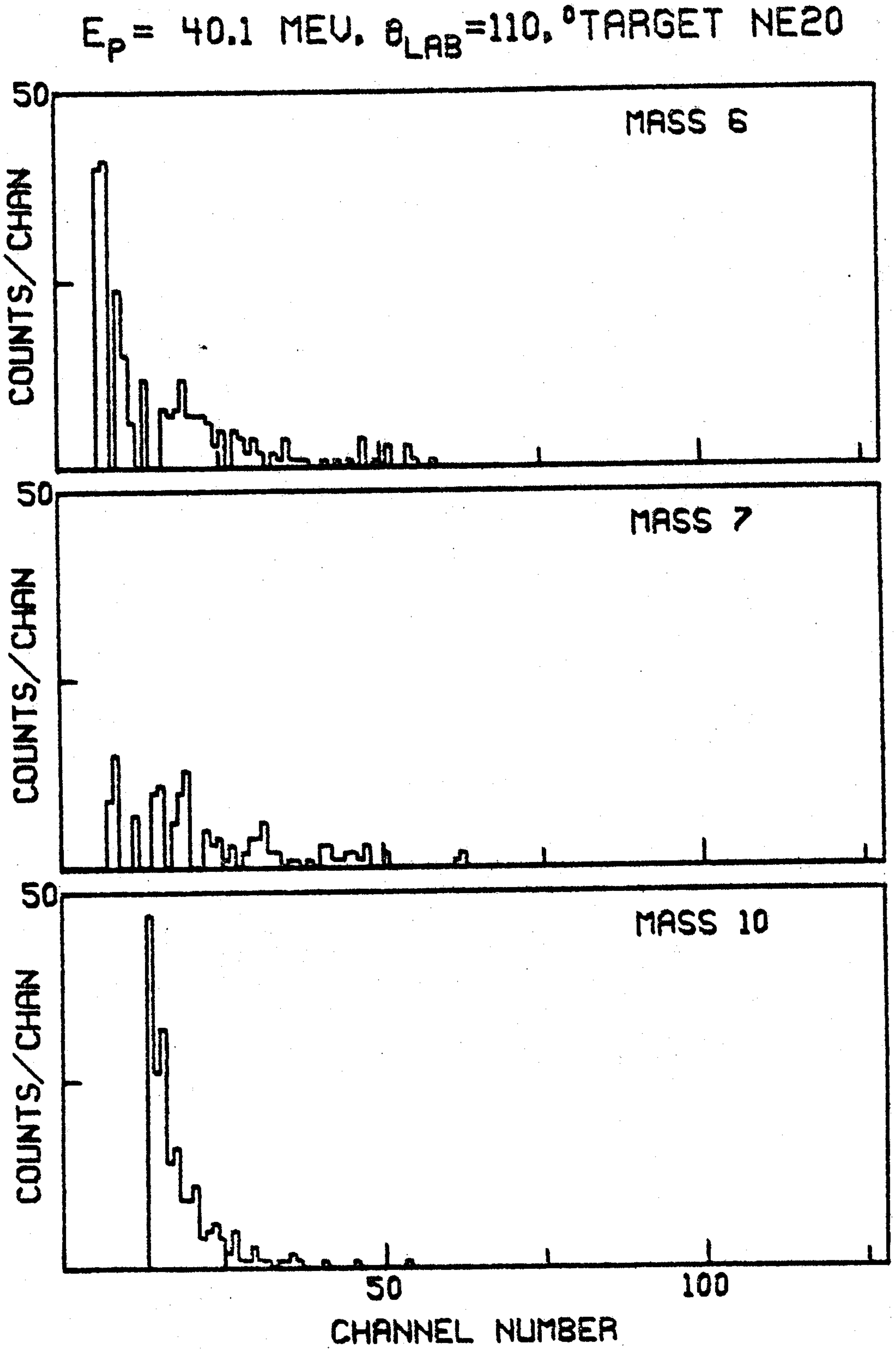

Fig. III.4.--(cont.) . . . (0.18 MeV/channel).

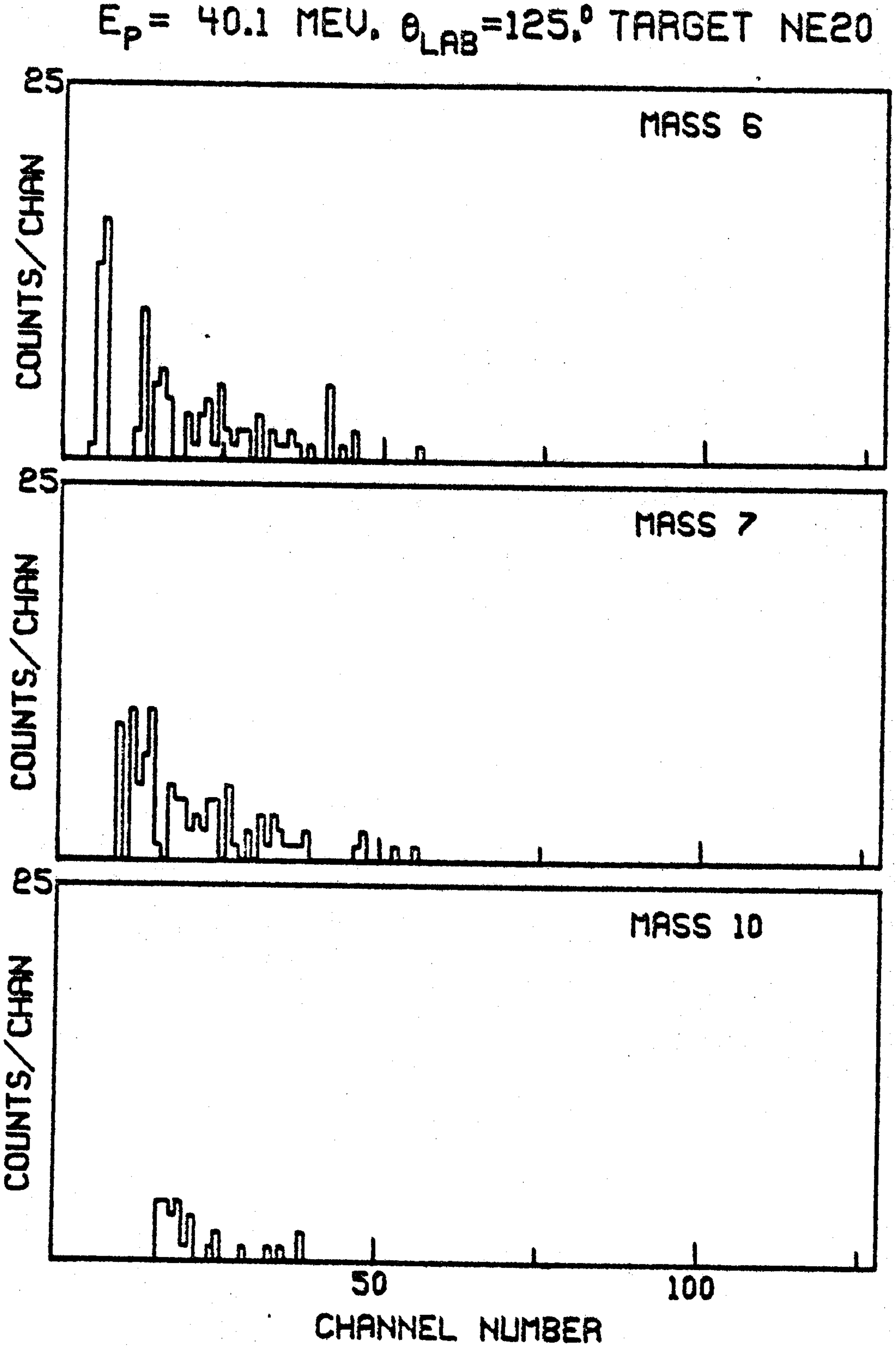

Fig. III.4.--(cont.) . . . (0.17 MeV/channel).

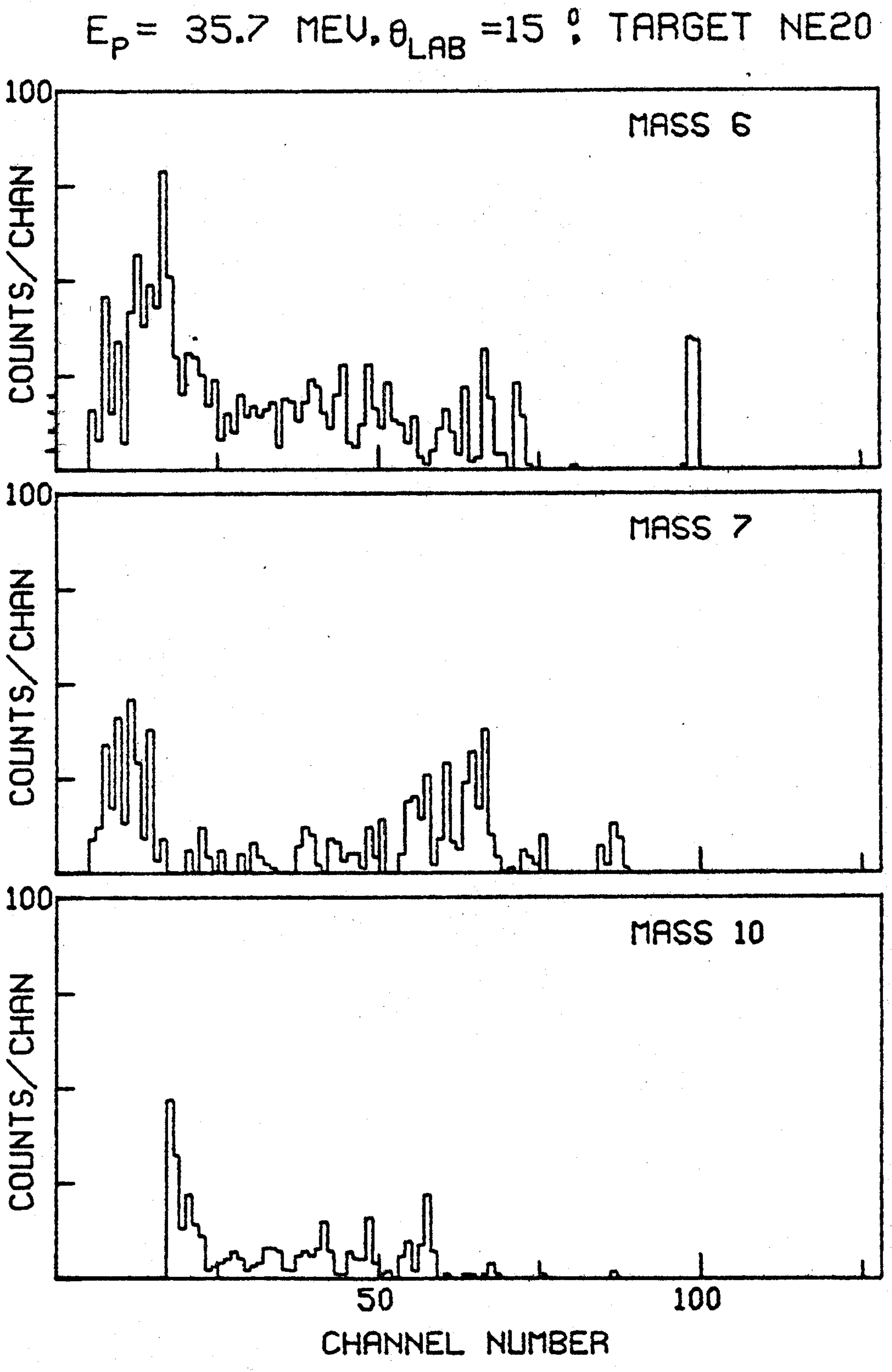

Fig. III.4.--(cont.) . . . (0.17 MeV/channel).

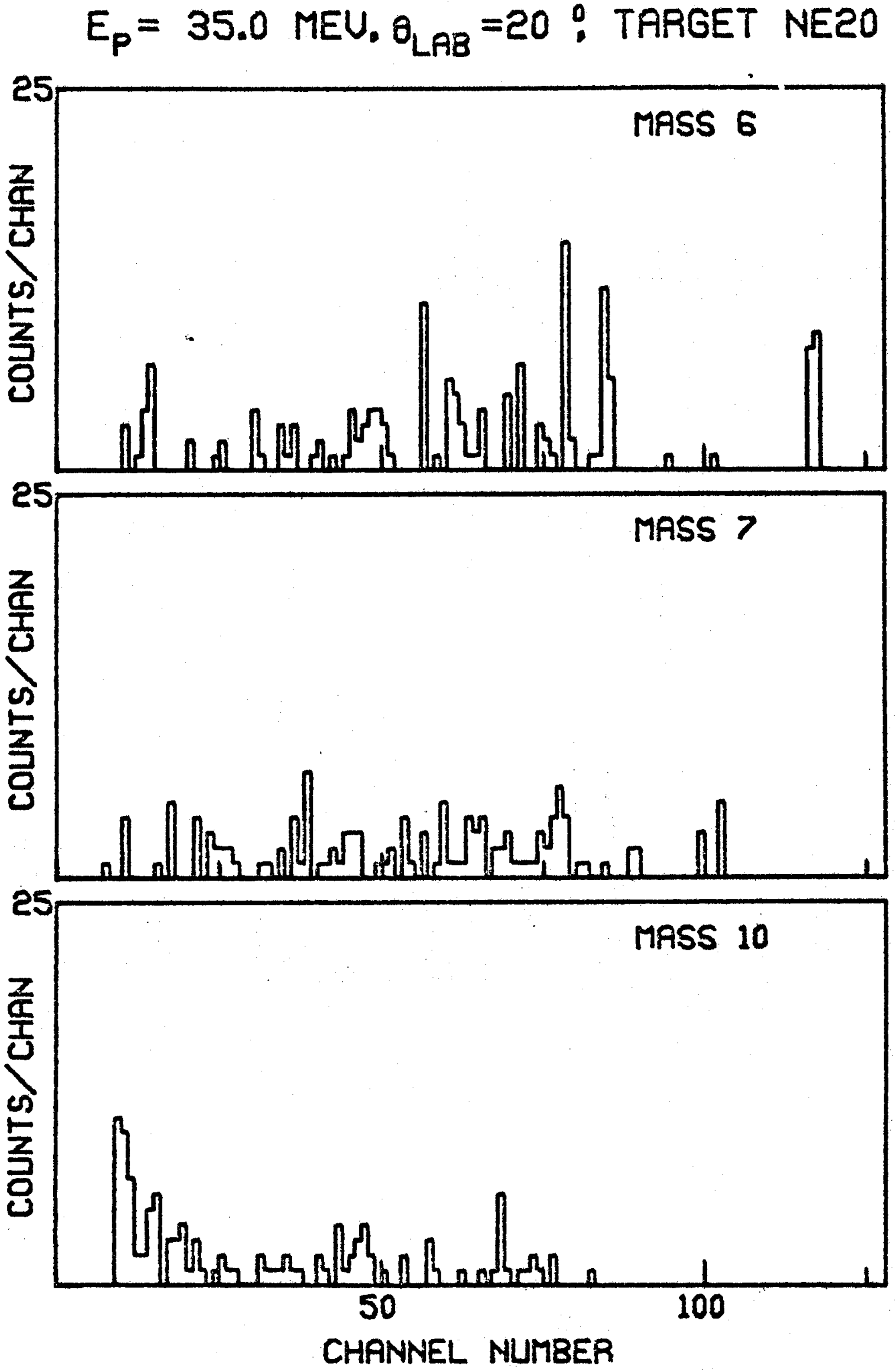

Fig. III.4.--(cont.) . . . (0.14 MeV/channel).

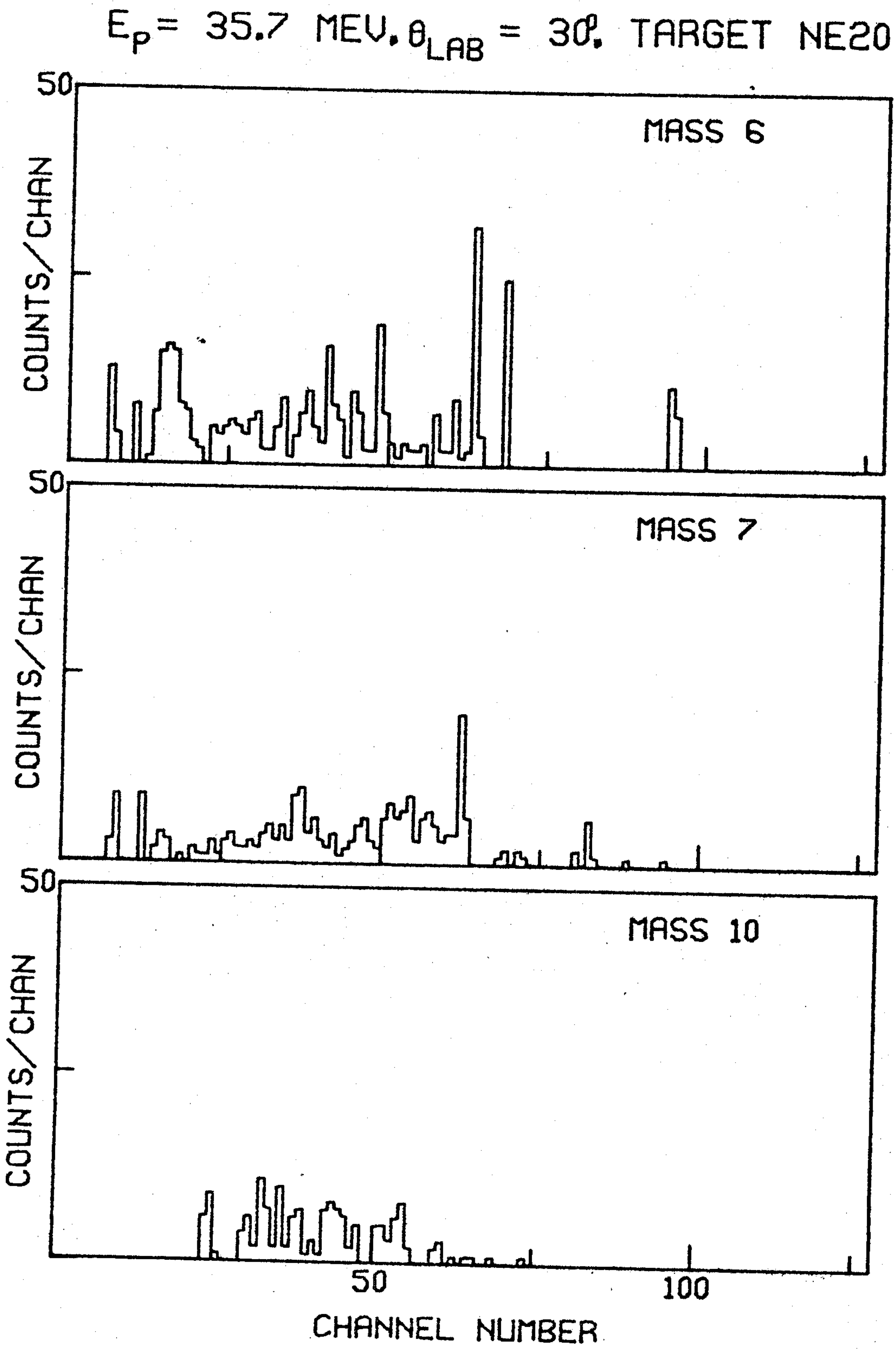

Fig. III.4.--(cont.) . . . (0.17 MeV/channel).

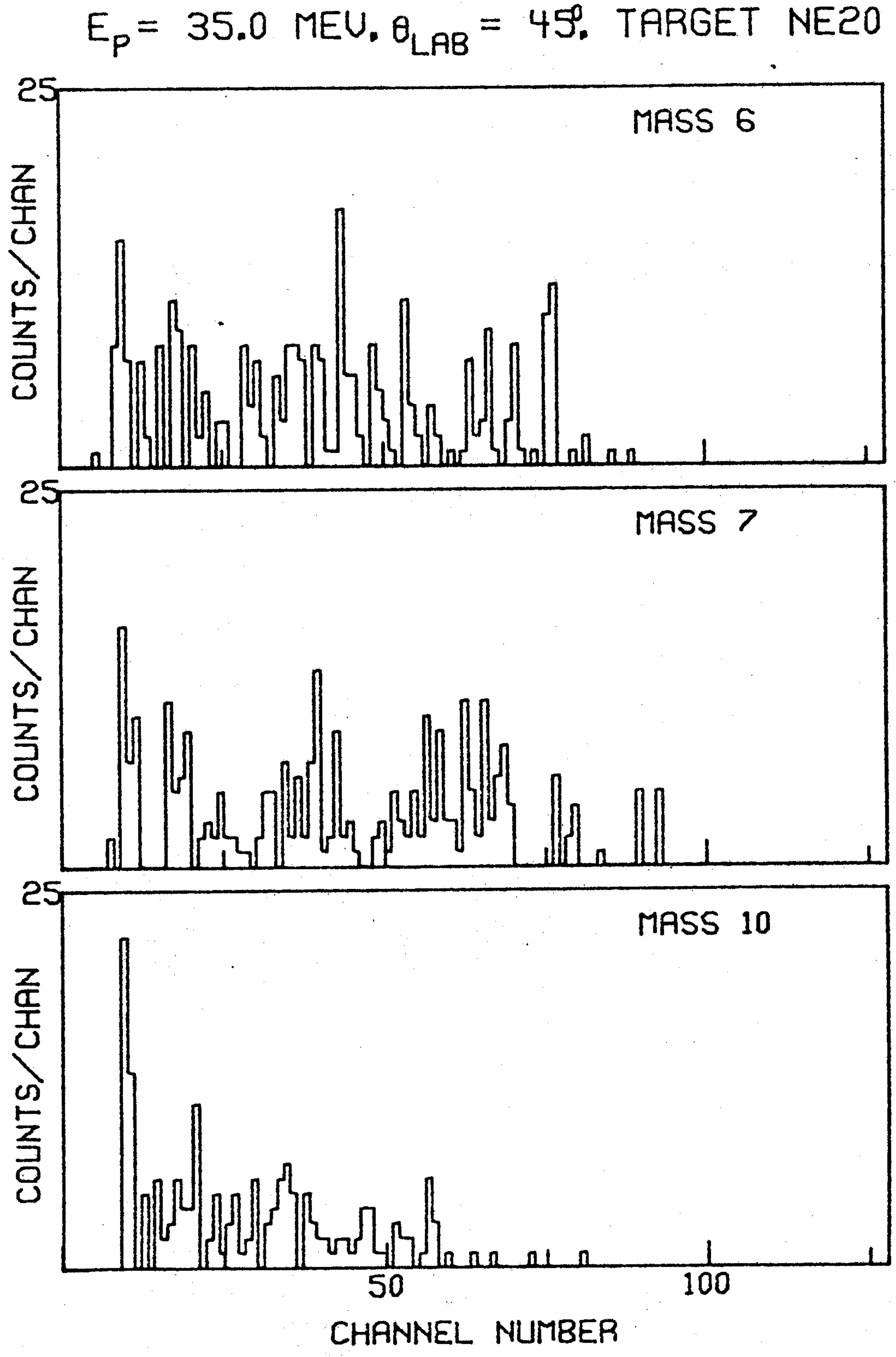

Fig. III.4.--(cont.) . . . (0.14 MeV/channel).

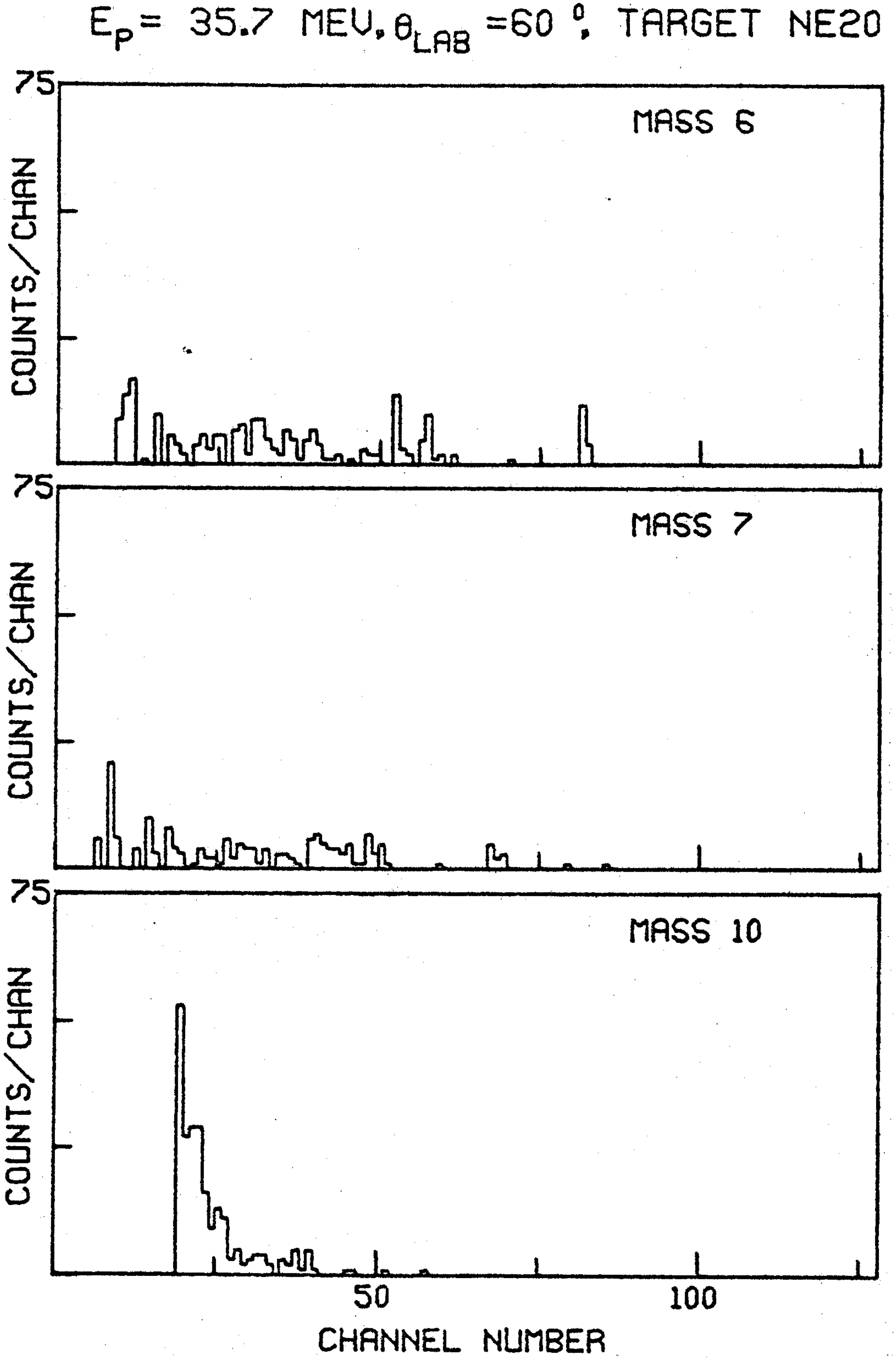

Fig. III.4.--(cont.) . . . (0.17 MeV/channel).

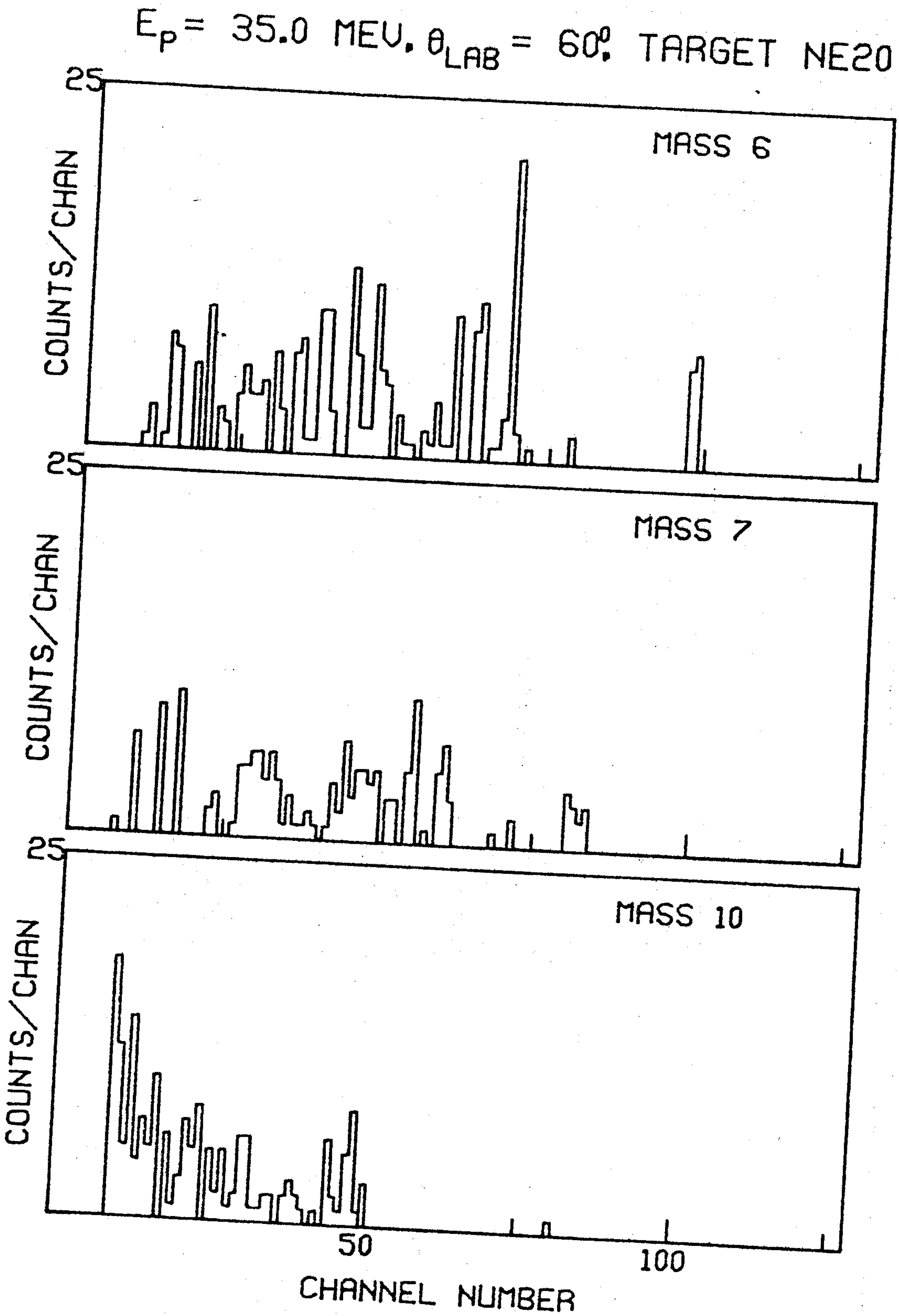

Fig. III.4.--(cont.) . . . (0.14 MeV/channel).

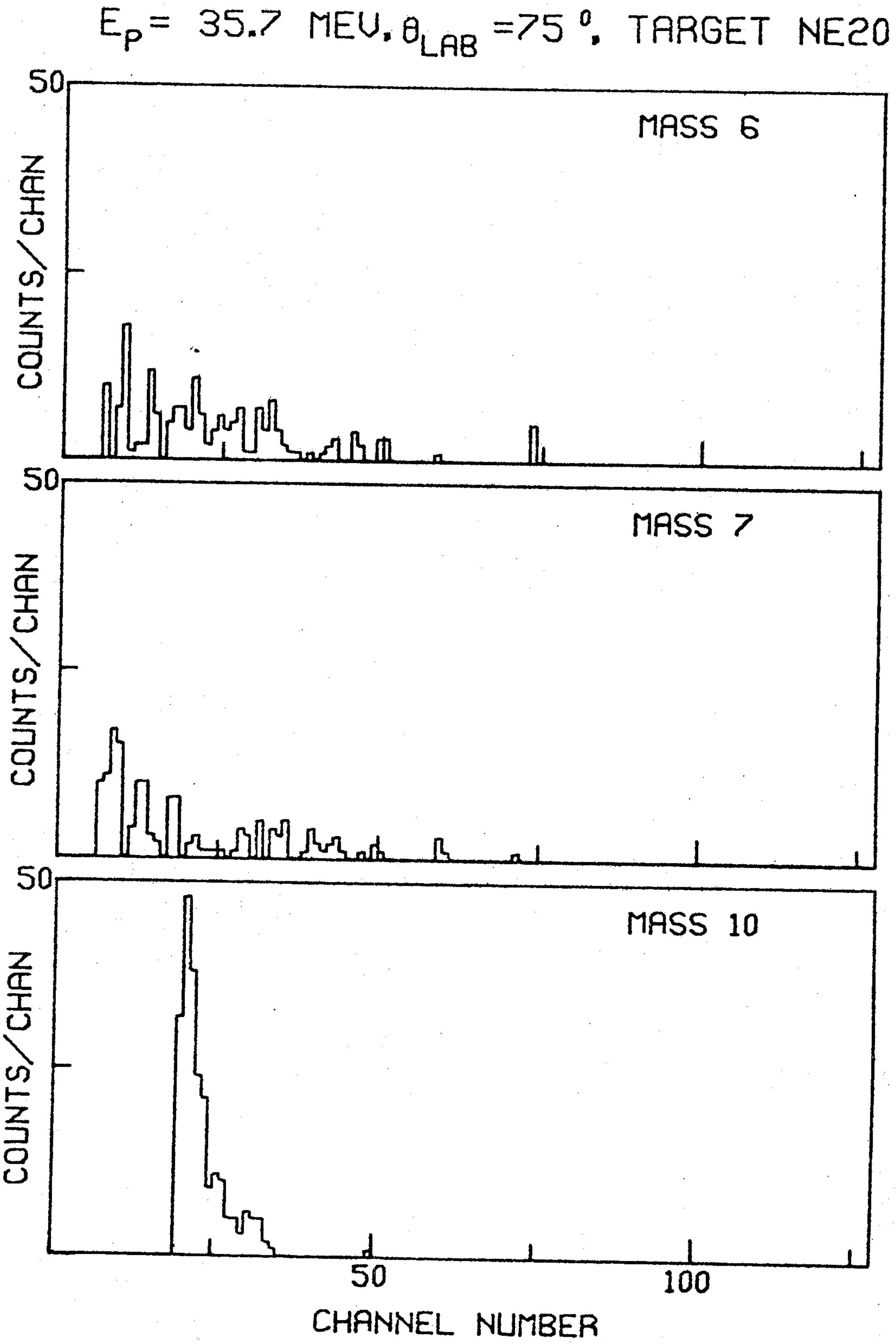

Fig. III.4.--(cont.) . . . (0.17 MeV/channel).

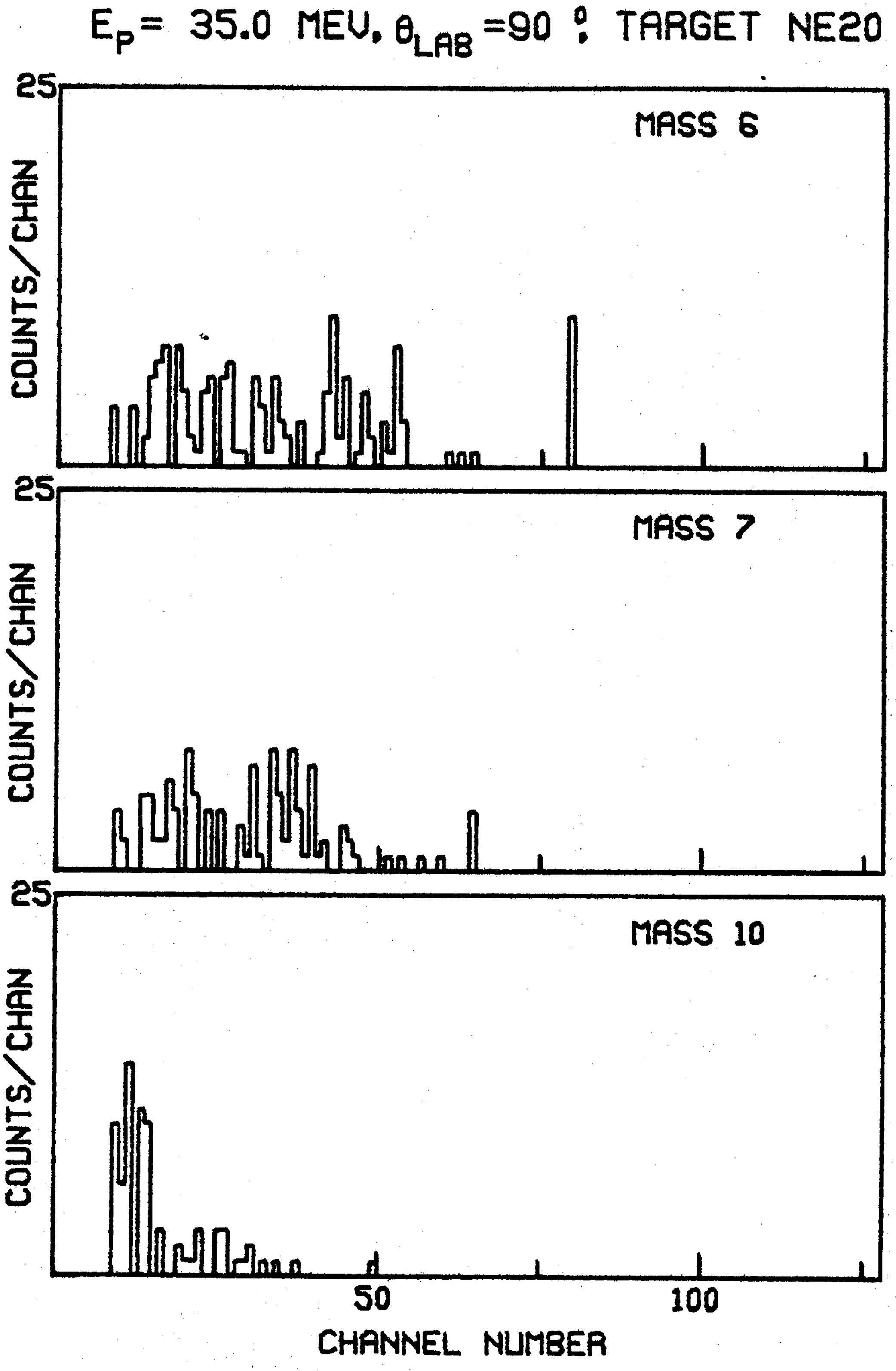

Fig. III.4.--(cont.) . . . (0.14 MeV/channel).

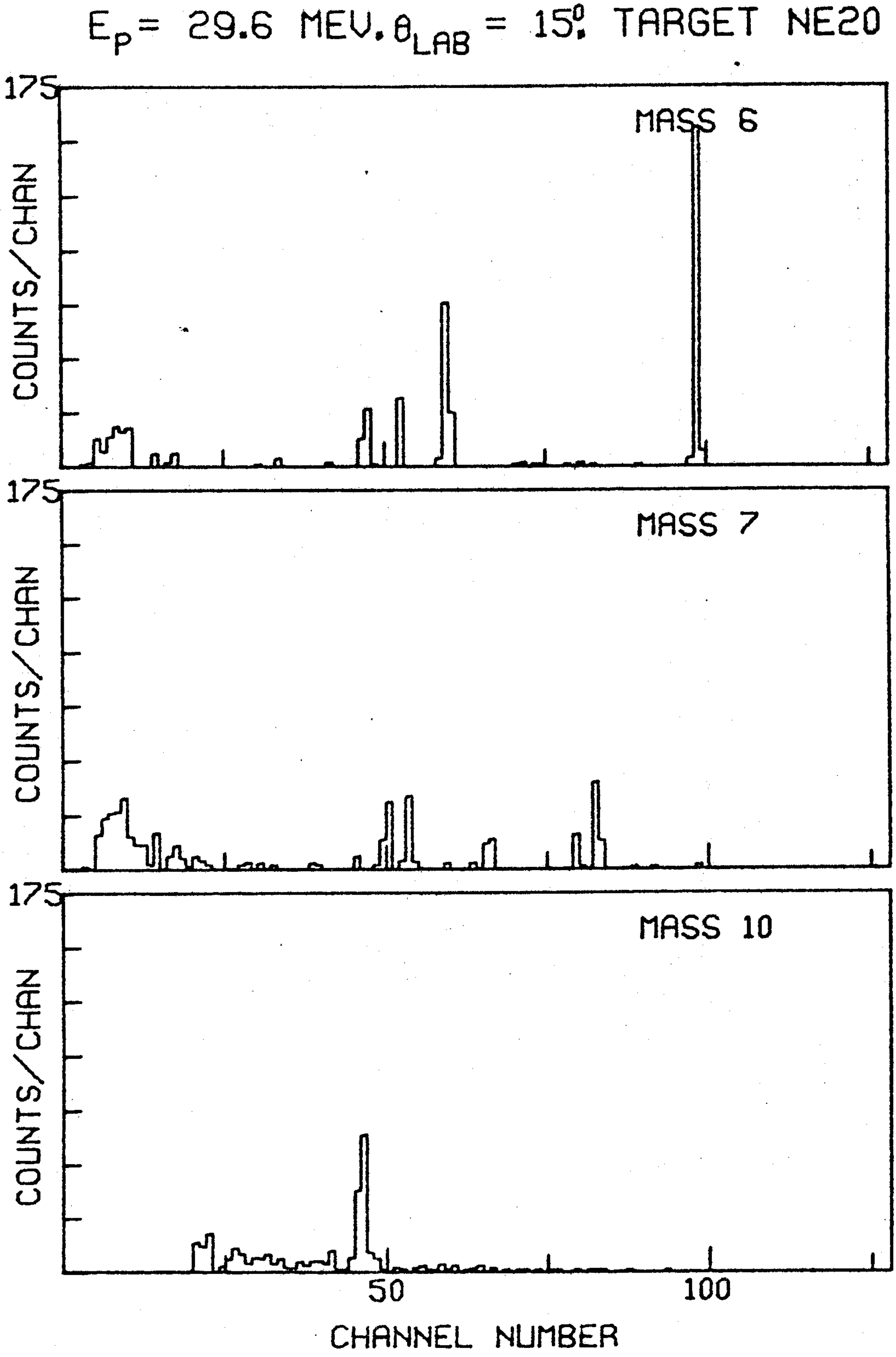

Fig. III.4.--(cont.) . . . (0.13 MeV/channel).

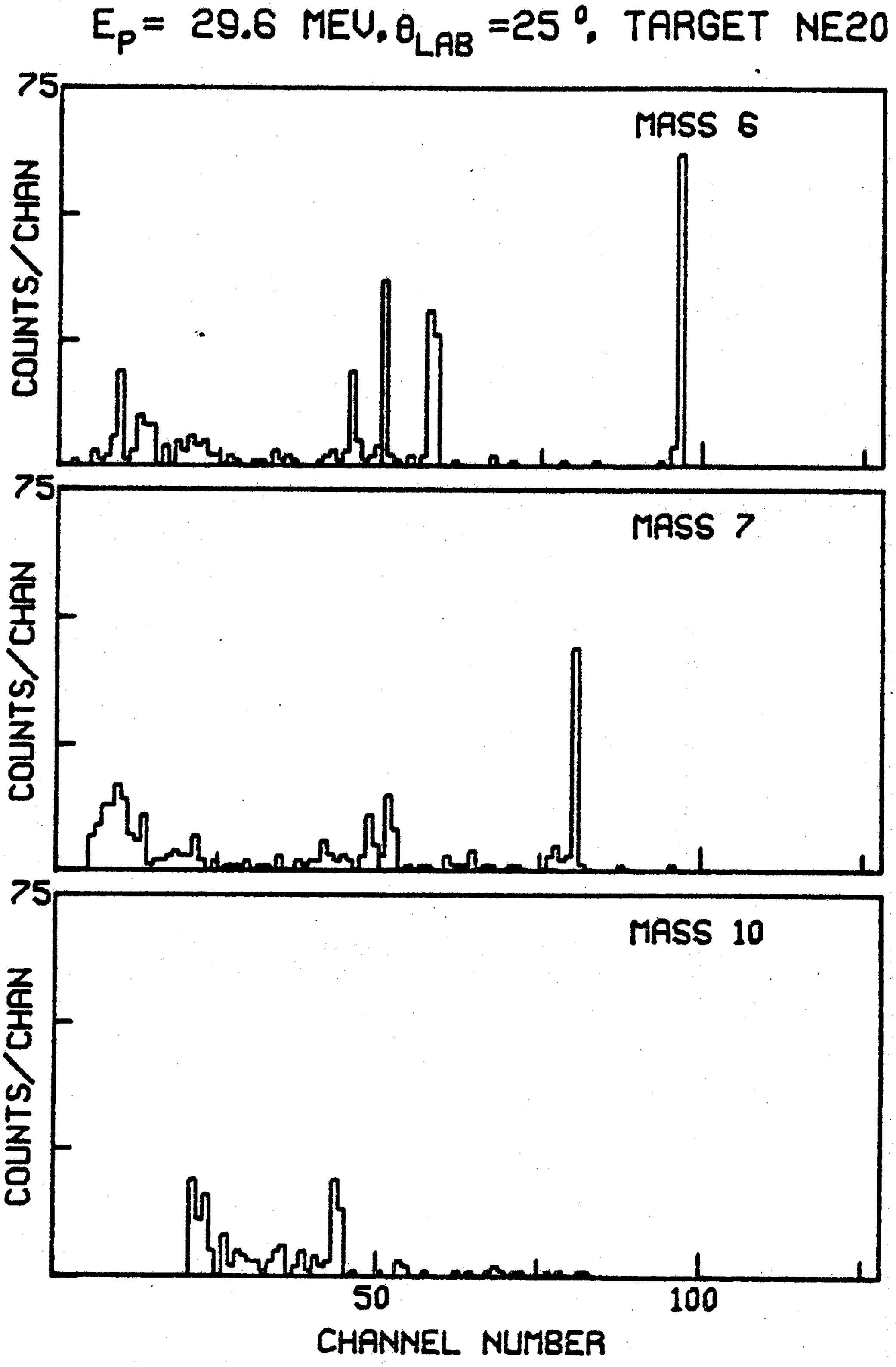

Fig. III.4.--(cont.) . . . (0.13 MeV/channel).

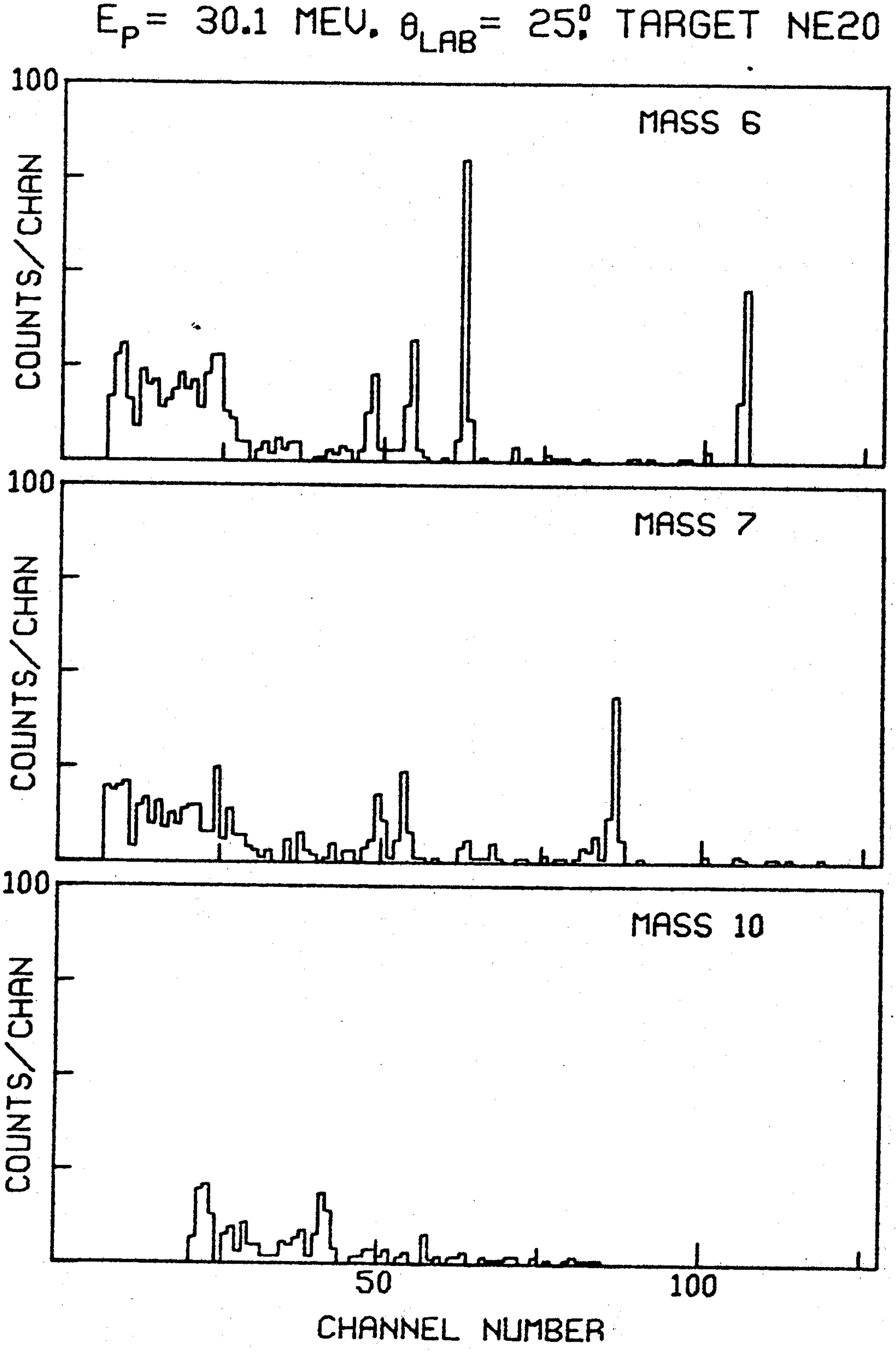

Fig. III.4.--(cont.) . . . (0.13 MeV/channel).

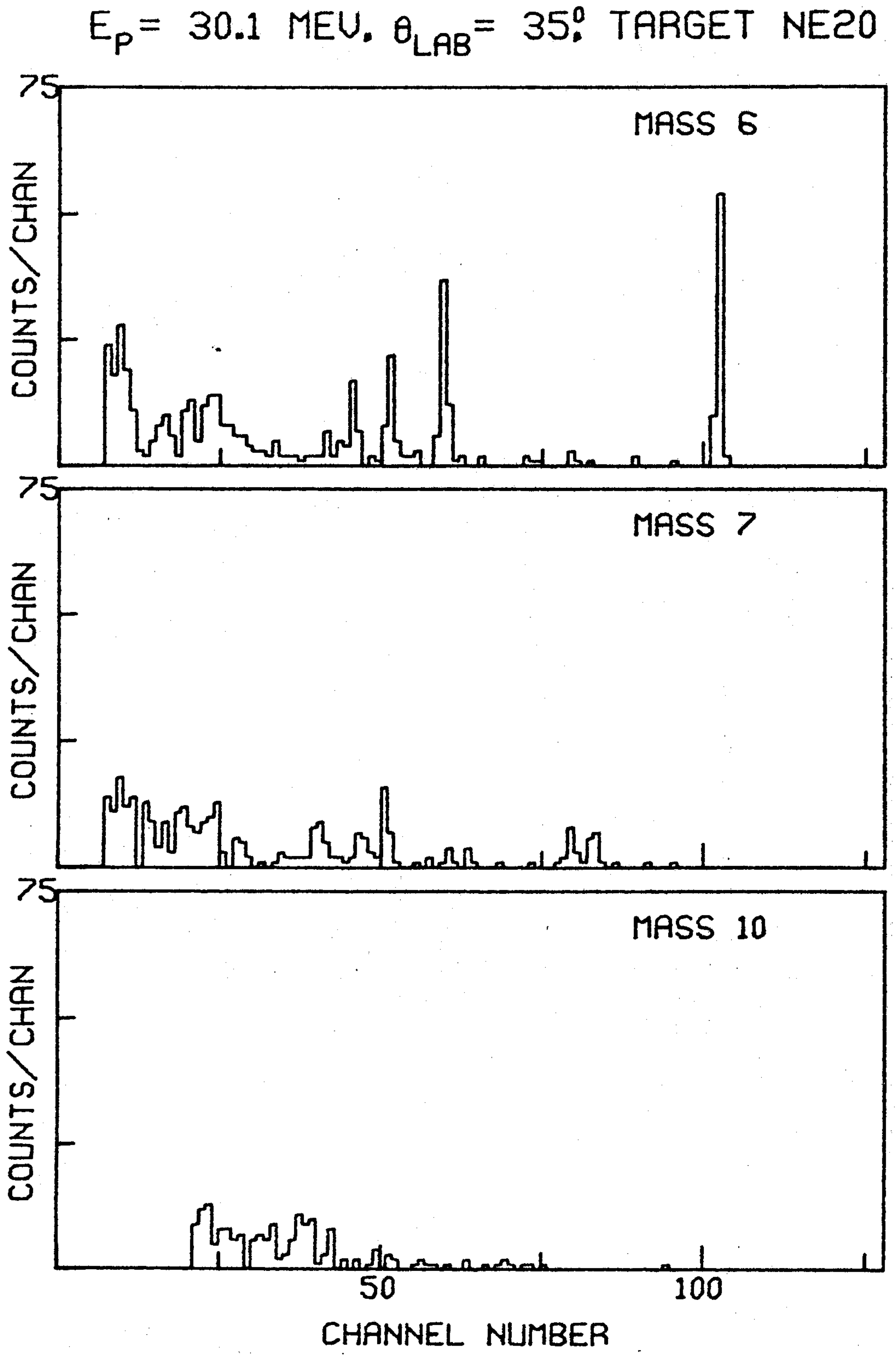

Fig. III.4.--(cont.) . . . (0.11 MeV/channel).

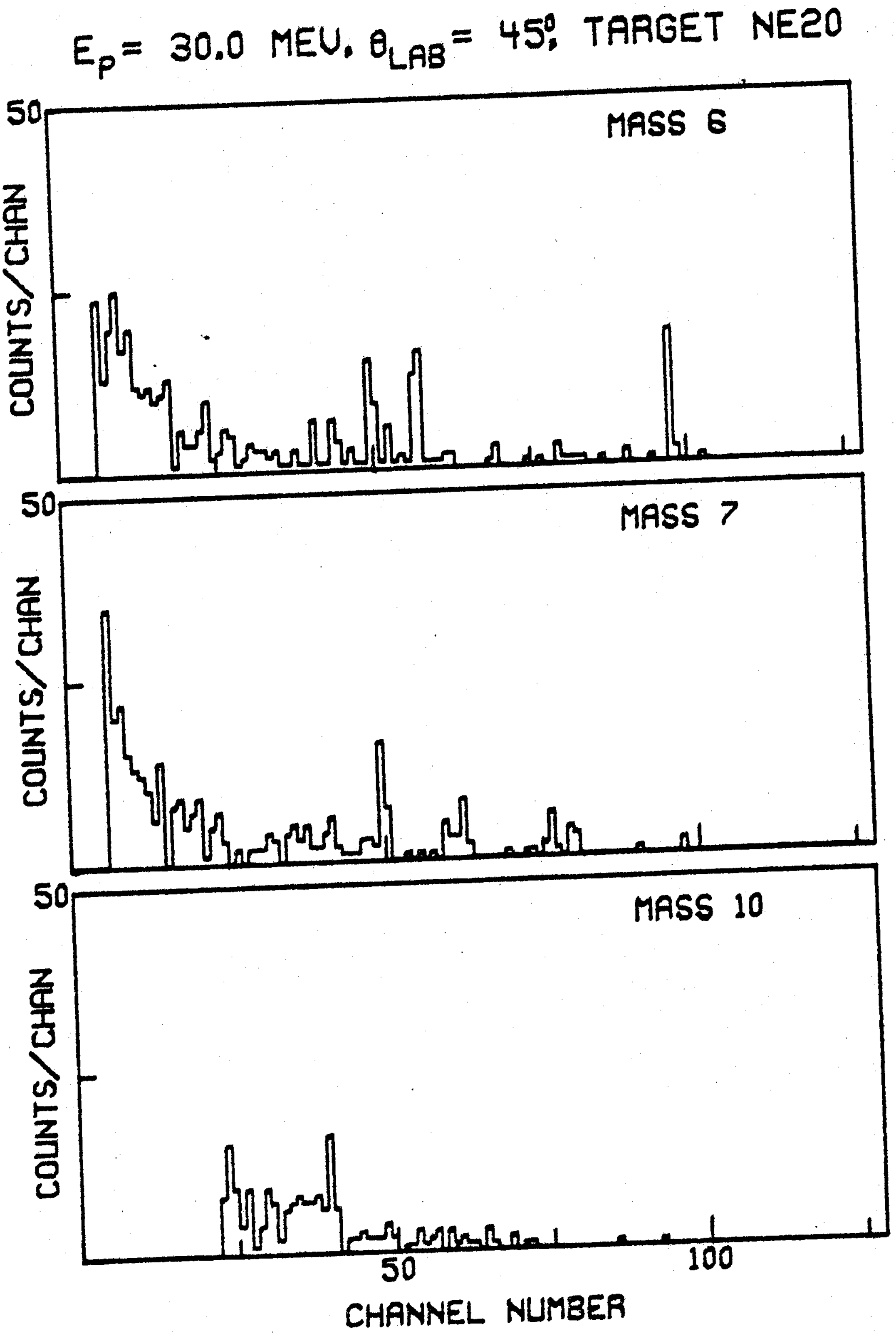

Fig. III.4.--(cont.) . . . (0.11 MeV/channel).

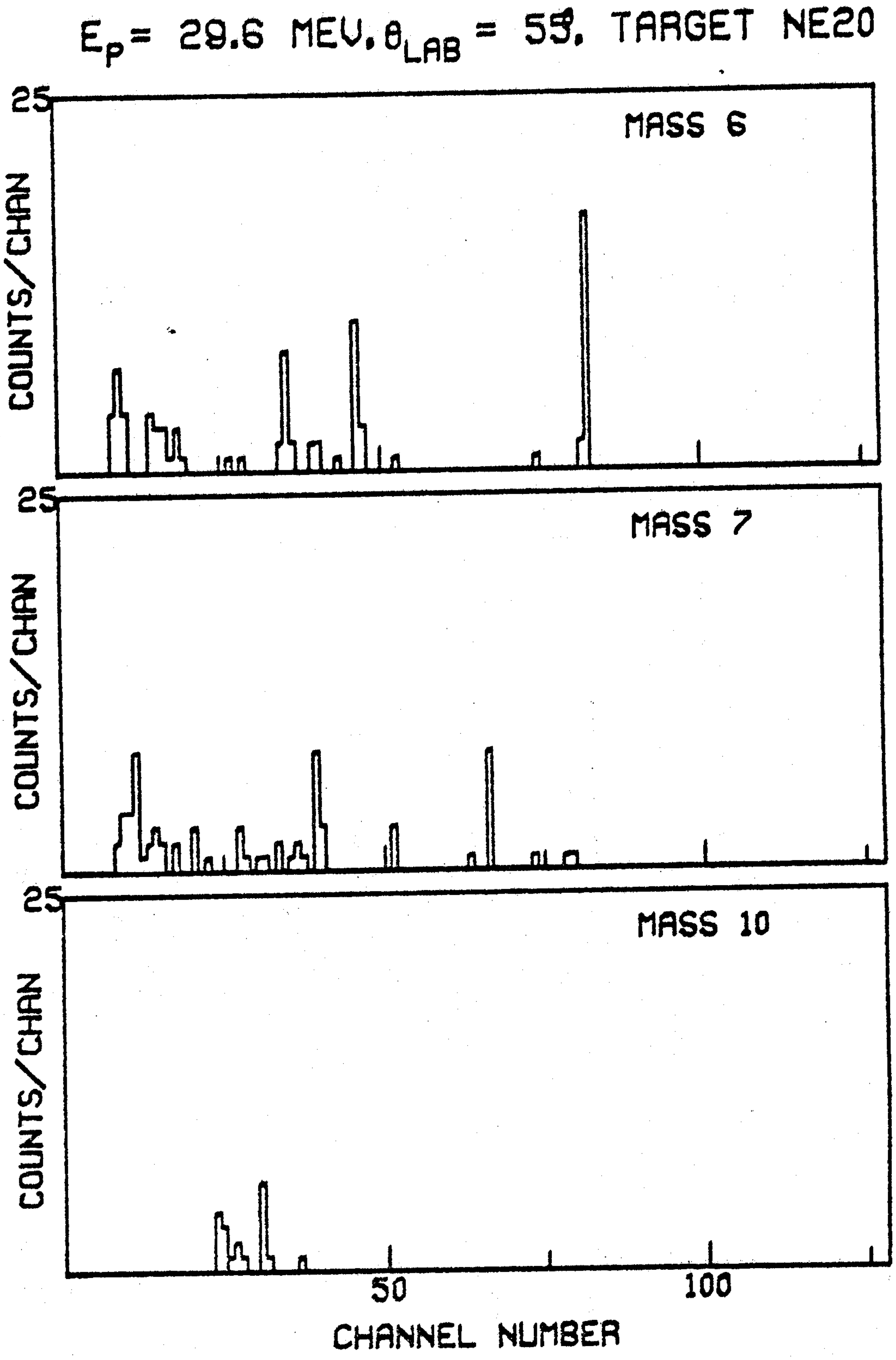

Fig. III.4.--(cont.) . . . (0.13 MeV/channel).

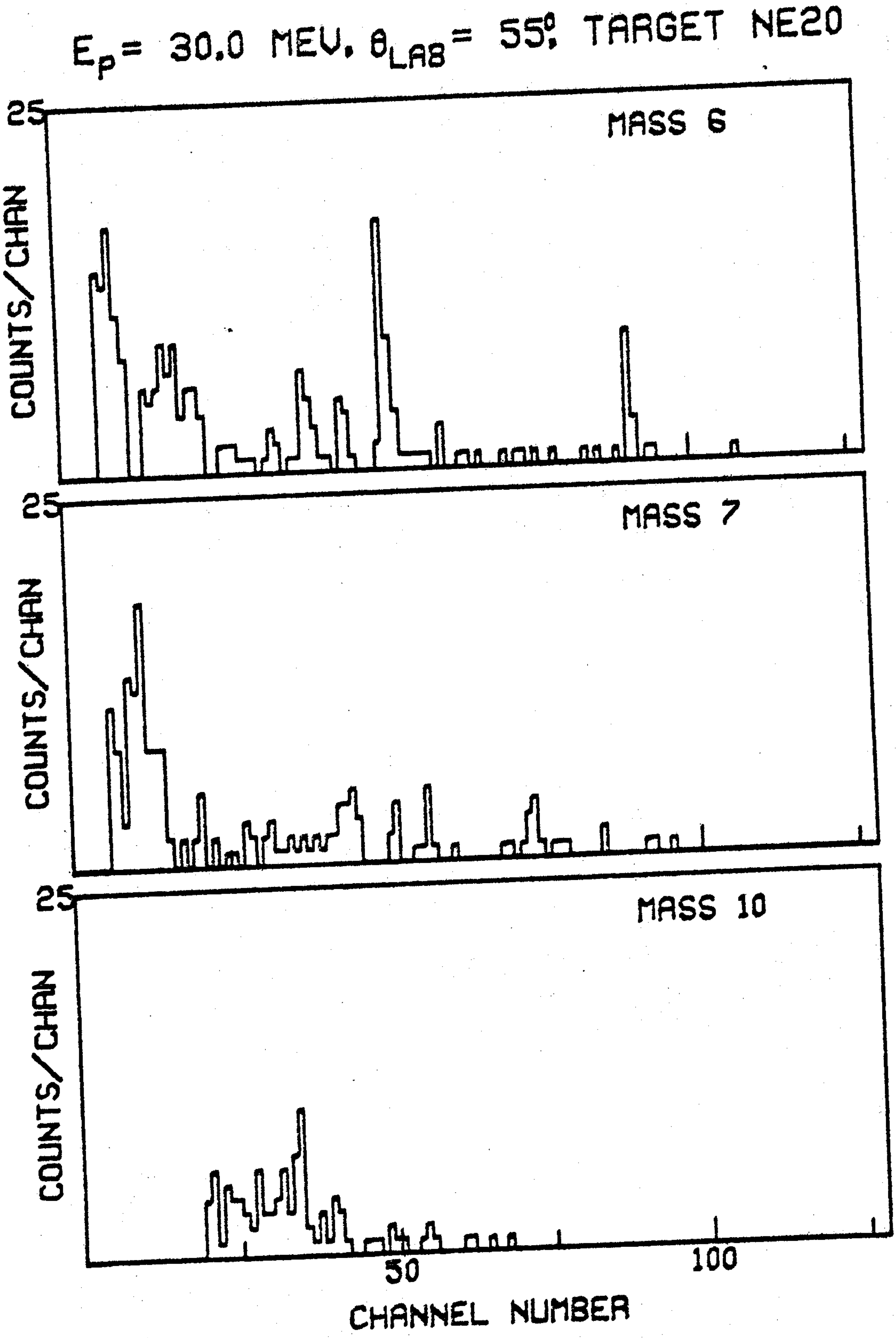

Fig. III.4.--(cont.) . . . (0.11 MeV/channel).

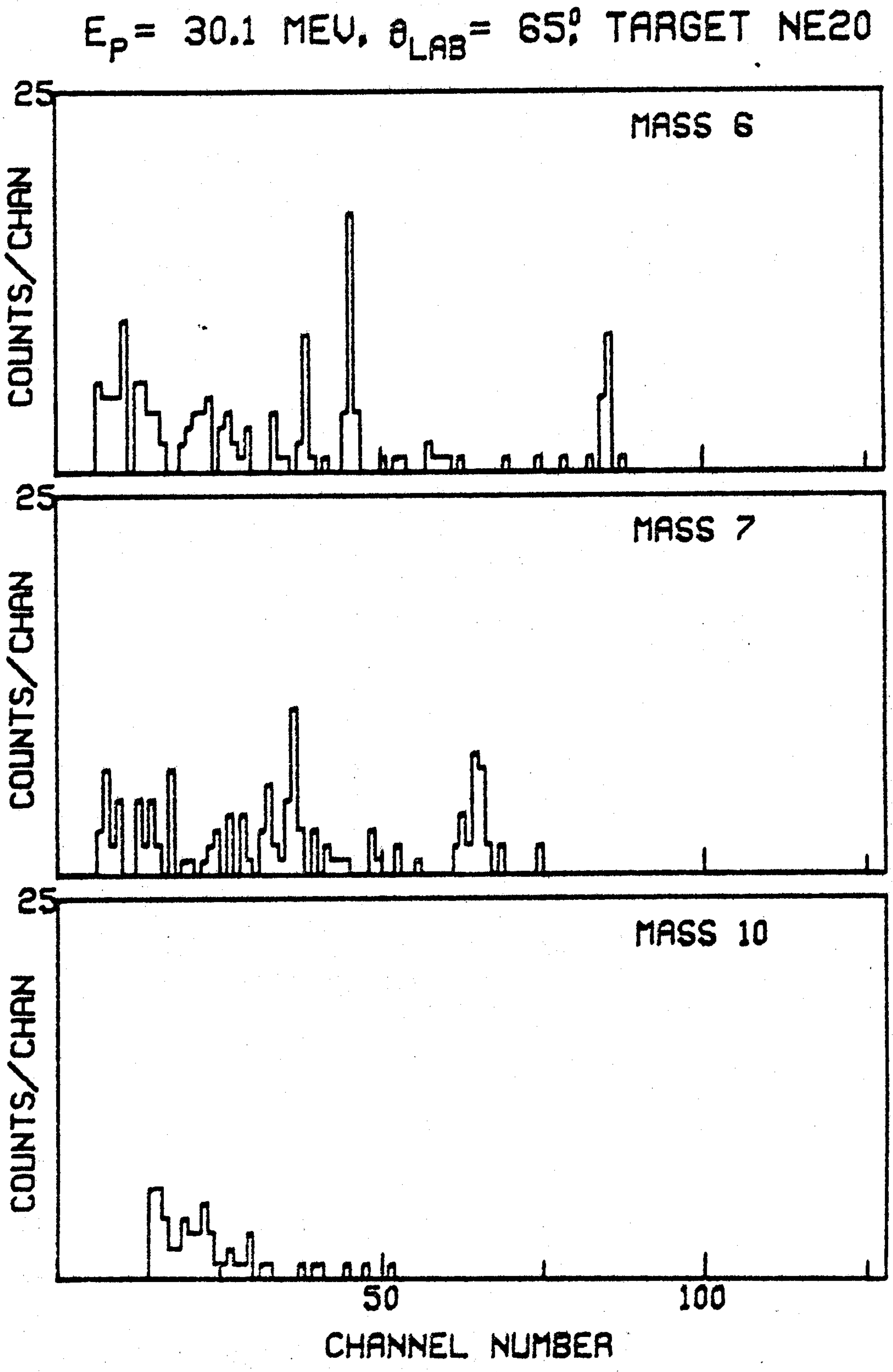

Fig. III.4.--(cont.) . . . (0.11 MeV/channel).

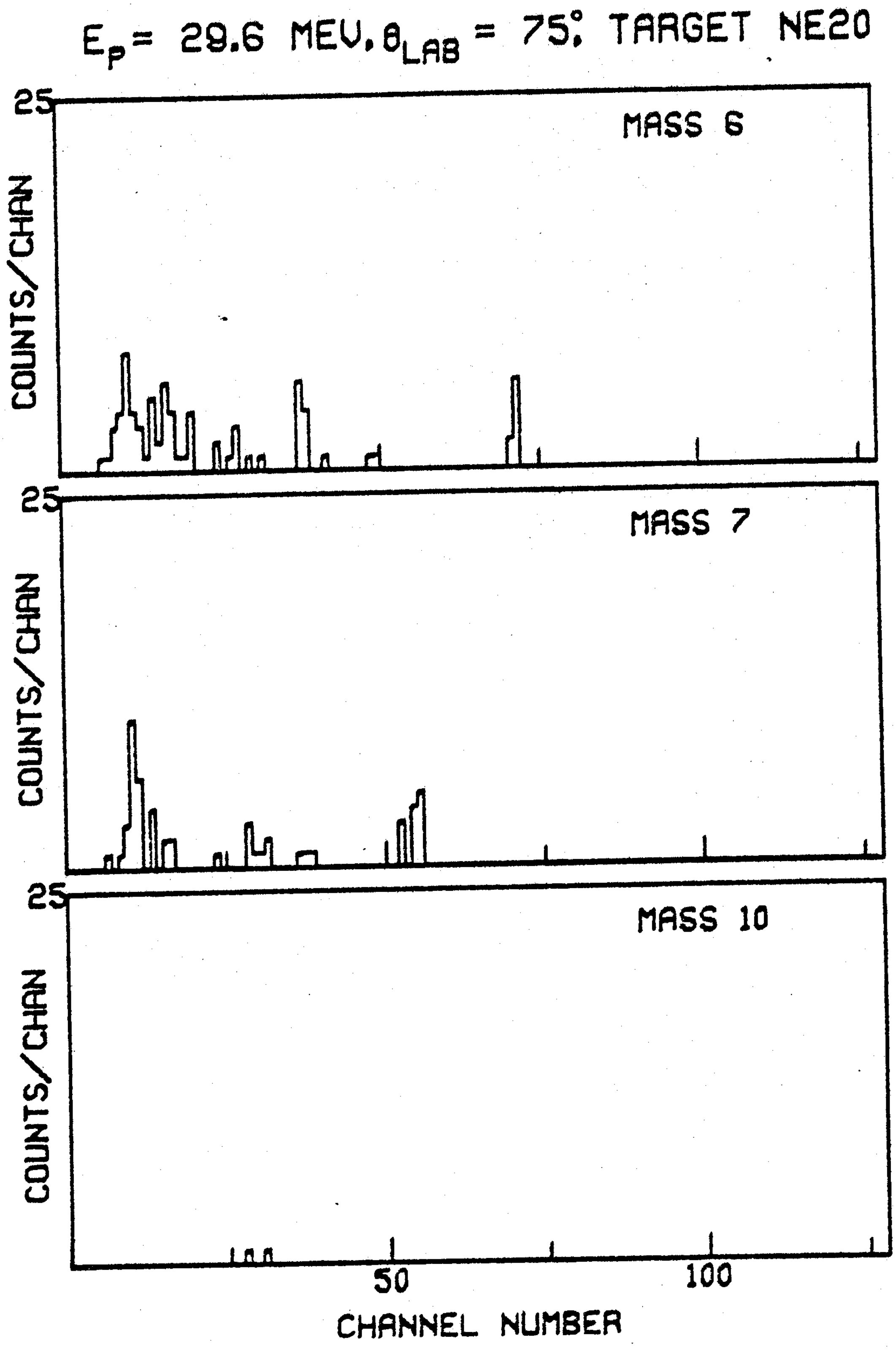

Fig. III.4.--(cont.) . . . (0.13 MeV/channel).

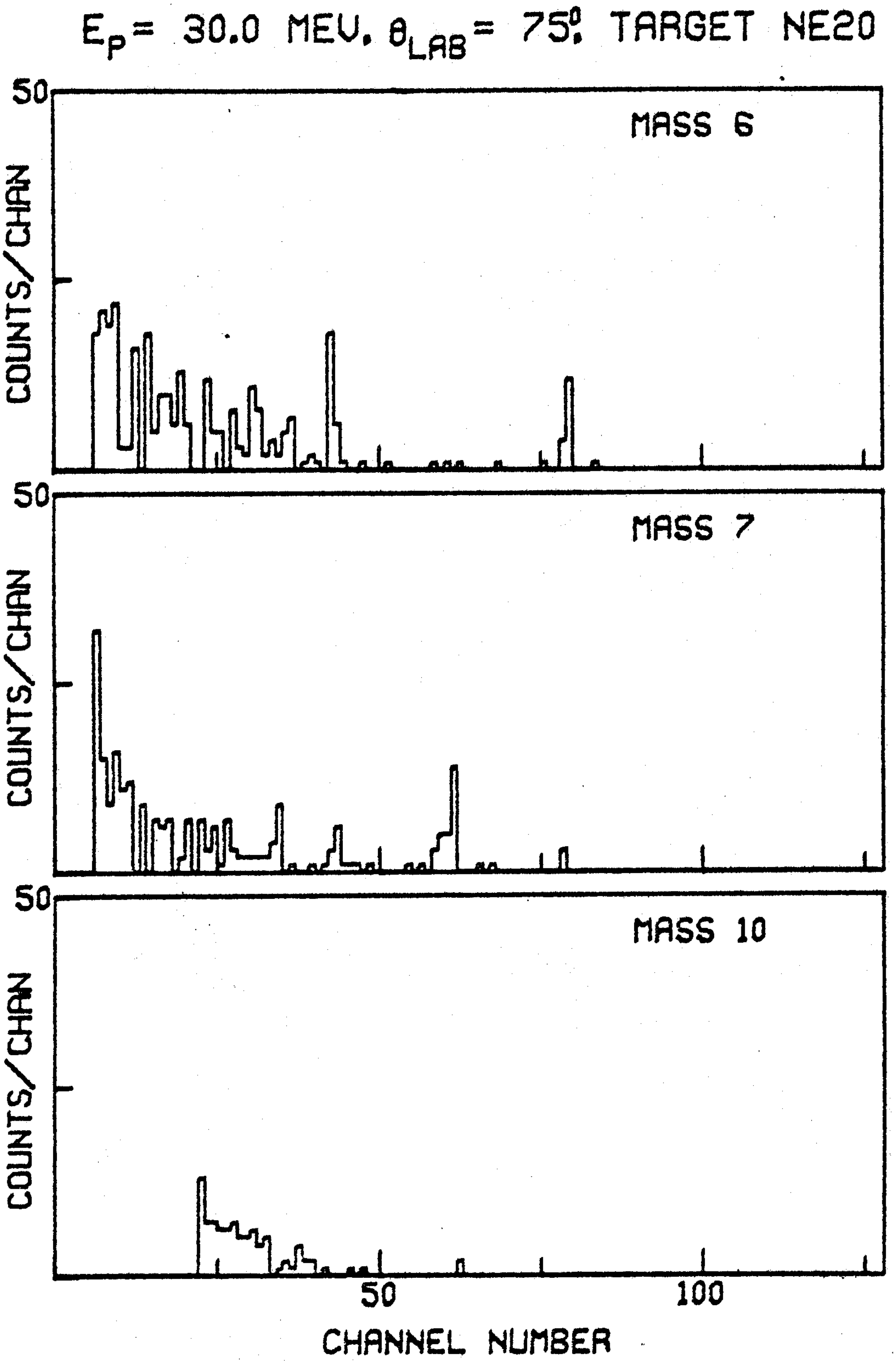

Fig. III.4.--(cont.) . . . (0.13 MeV/channel).

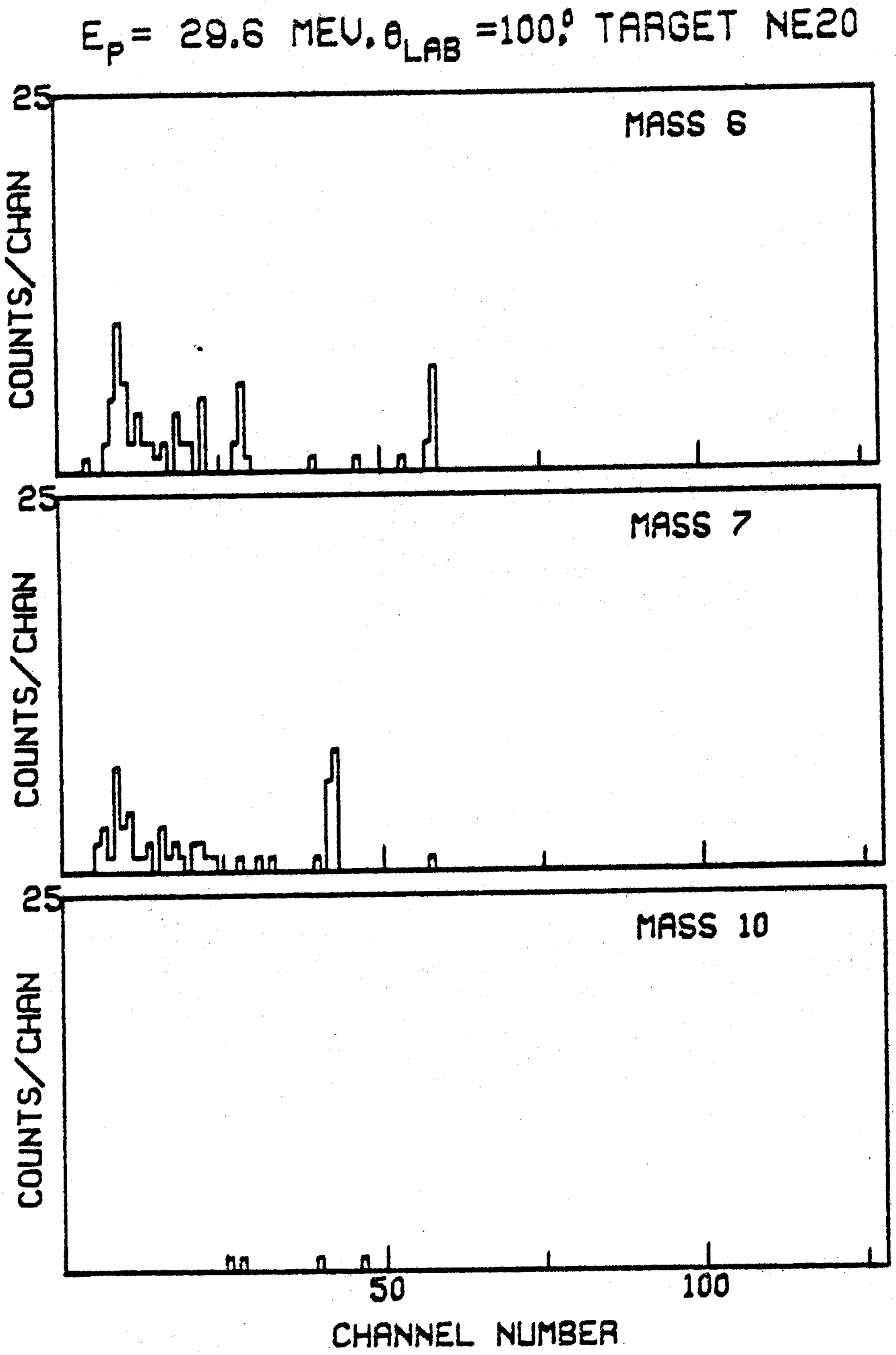

Fig. III.4.--(cont.) . . . (0.13 MeV/Channel).

The spectra are then integrated over energy to obtain the total yield. Since the spectra cut off at an energy E_{LO} of about 0.8 MeV because of the limiting sensitivity of the time-pickoff unit or because of the limit due to the finite size of the time interval between two beam bursts, these spectra must then be extrapolated to zero energy to obtain the total yield at a given angle.

Since the reaction products lose energy in going through the gas of the target and the formvar window, E_{LO} for each mass was corrected to be equal to the energies of these particles at the time they were created. The energy loss in the gold layer in front of the surface barrier Si-detector (40 $\mu g/cm^2$) was ignored since it was only 0.02 MeV for a 1 MeV ^7Li (No 70) (the energy scale is always larger than 0.1 MeV/channel), and of course it is not expected to be much different for ^6Li, compared to 0.43 MeV and 0.08 MeV for ^{20}Ne at 15° and 90° scattering angle respectively. These corrections were made by integrating the stopping power formula:

$$\frac{dE}{d(\rho x)} = 0.30711 \times \frac{Z}{W} \frac{Z_i^{\,2}(E)}{\beta^2} \left[\ln \frac{A(E)}{[1-\mathrm{esp}(-A^1/\rho(E))]\rho} - \beta^2 \right] (\mathrm{MeV\ cm^2/g})$$

(A(E) and ρ are explained in the (Wi 66)), to find the energy E_I of a particle whose energy loss is such that after traversing the total exit areal density (gas + formvar) its energy is equal to E_{LO}. This formula has been translated into FORTRAN IV language in the MSU Cyclotron Laboratory by Dr. P. S. Miller. The range in ^{20}Ne given by this program and the table by Northcliffe et al. (No 70) for 1.4 MeV ^{7}Li agree to within 8% (1.4 MeV is chosen just for convenience in reading the table, although it is very close to the value of E_I in most cases, see Table III.3). A table of initial energy, and the corresponding energy loss for every run is generated and the energy after traversing the exit areal window is matched to E_{LO} and thereby E_I is chosen. E_{LO} is found from the energy calibrations for each run based on the position of ^{6}Li ground state group. E_I found this way is the energy at creation of the particle with energy E_{LO}.

Since no particles formed with energy less than E_I are detected one has to add to the yield that is found from the net spectrum the estimated yield of the unobserved region. This is done by multiplying the number of channels corresponding to E_I by the average number of counts per channel over the first five channels in the net energy spectrum and adding this to the yield.

TABLE III.3.--Parameters Used for Extrapolation.

Run No.	Lab Angle (Deg)	Flight Path (cm)	Pressure (Atm)	Exit areal density of target (μg/cm^2)	Formvar Thickness (μg/cm^2)	E_I ^{6}Li (MeV)	En Scale (MeV/Ch)	No. Chan. to be Extrapol.
122	15	27.67	0.048	89.917	38.4	1.205	0.1256	10
124	25	25.860	0.047	58.482	38.4	1.065	0.1256	9
125	55	25.122	0.047	30.046	38.4	0.936	0.1256	7
126	75	24.902	0.047	21.406	38.4	0.897	0.1256	7
127	100	24.855	0.047	19.534	38.4	0.888	0.1256	7
152	55	25.1225	0.056	30.496	38.4	0.698	0.1131	6
153	45	25.276	0.056	37.374	38.4	0.730	0.1131	6
154	75	24.902	0.055	20.244	38.4	0.652	0.1131	6
155	25	25.860	0.112	128.864	38.4	1.244	0.1317	9
156	35	25.494	0.112	94.877	38.4	1.090	0.1131	10
157	65	25.003	0.112	50.255	38.4	0.887	0.1131	8
159	15	26.670	0.120	214.769	38.4	1.535	0.112	14
134	15	27.67	0.052	94.137	38.4	1.860	0.1674	11 ←
135	30	25.649	0.051	51.005	38.4	1.42	0.1674	8
136	60	25.060	0.051	26.330	38.4	1.315	0.1674	8
137	75	24.902	0.051	19.634	38.4	1.285	0.1674	8
144	20	26.168	0.057	82.131	38.4	1.555	0.143	11
145	60	25.060	0.057	31.116	38.4	1.335	0.143	9
146	45	25.276	0.056	40.295	38.4	1.375	0.143	10
147	90	24.765	0.055	17.162	38.4	1.275	0.143	9

99	10	27.622	0.055	134.993	38.4	1.40	0.1822	8
92	17	26.397	0.055	79.793	38.4	1.25	0.1822	7
93	30	25.611	0.055	44.407	38.4	1.15	0.1822	6
94	45	25.237	0.055	27.572	38.4	1.10	0.1822	6
95	60	25.022	0.055	17.853	38.4	1.07	0.1822	6
96	80	24.817	0.055	8.631	38.4	1.05	0.1822	6
97	110	24.913	0.055	12.946	38.4	1.070	0.1822	6
98	125	25.084	0.055	20.679	38.4	1.070	0.1822	6
108	17	26.435	0.052	81.017	38.4	1.250	0.1756	7
109	30	25.650	0.047	43.124	38.4	1.150	0.1756	7
110	50	25.193	0.049	26.194	38.4	1.100	0.1756	6
111	70	24.950	0.053	18.163	38.4	1.070	0.1756	6
118	100	24.855	0.032	8.442	38.4	1.050	0.1756	6
128	37	25.443	0.057	47.103	38.4	1.150	0.1756	7
129	90	24.765	0.057	15.625	38.4	1.070	0.1756	6
130	100	24.675	0.056	11.392	38.4	1.050	0.1756	6
77	15	26.622	0.027	49.714	38.4	1.425	0.172	8
78	30	25.601	0.027	27.033	38.4	1.325	0.172	8
79	45	25.227	0.027	18.731	38.4	1.290	0.172	8
80	65	24.955	0.027	12.679	38.4	1.260	0.172	7
81	90	24.717	0.027	7.391	38.4	1.240	0.172	7

Table III.3 shows the energy cutoff for ^{6}Li at different angles for different bombarding energies together with the number of channels to be extrapolated, which number depends in general on the angles. This averaged extrapolation is reasonable since there is no indication of a strong peaking in the low energy region and the spectrum also has to go to zero at zero energy in the laboratory system because the Jacobian of the transformation of the cross section from the center of mass system to the laboratory system is zero ($J = p_{LAB}/p_{cm}$) (St 63). Fifty percent of this extrapolating yield is assigned as the uncertainty in the extrapolation and is added in quadrature to the statistical error associated with the net yield to result in the error reported in Table III.

Since the mass resolution is worse for mass-10 than for mass-6 and mass-7, one cannot separate mass-10 from mass-11 at low energy and extrapolation has to be done from higher channels. Even though the energy cutoff for this mass is experimentally about 1.7 MeV the extrapolations have been started from the 3.4 MeV region. This large extrapolation introduces a substantial uncertainty into our measurements of the mass-10 cross sections. In addition it is impossible to reliably separate mass-11 from the large mass-12 yield, even at 3.4 MeV. For this reason we have been unable to obtain an estimate of the mass 11 cross section.

III.4 Differential Cross Section

The differential cross section of production is calculated by using the formula (Si 59, Wo 53):

$$\sigma(\theta) = \frac{Y \sin \theta}{nNG}$$

where: Y = yield for each mass at the laboratory angle θ as described above

n = number of target per cm^3

N = number of the incident protons

G = G-factor of the two-slit-system with rectangular aperture

and are calculated as follows:

$$n = \frac{6.023 \text{ X } 10^{23}}{22.414 \text{ X } 10^{3}} \times \frac{P \times \rho}{13.6 \times 76} \times \frac{273}{T} \text{ atoms}$$

P being the pressure of the gas target in cm oil and ρ the density of the oil in g/cm^3 (= 0.9812 g/cm^3).

$$N = \frac{QFC}{1.6021 \times 10^{-19}} \text{ protons}$$

QFC being the integrated charge collected in the Faraday Cup in Coulombs.

$$G = \frac{4b_1b_2l}{Rh} (1 + \Delta_o) \text{ (cm)}$$

where: b_1 = the half width of the front slit (cm)

b_2 = the half width of the rear slit

l = the height of the rear slit (cm)

R = the distance between the beam and the rear slit (cm)

h = the distance between the front and rear slits (cm)

Δ_o = slope non-dependent term (Si 59).

Table III.4 lists the various front slits used in the experiments.

TABLE III.4.--Various slit sizes (in in.) used in the experiments.

Front Slits		Rear Aperture	
Width	Height	Width	Height
0.0425	0.75	0.125	0.25
0.0430	0.75		
0.0435	0.75		

Table III.5 lists the differential cross sections for mass-6 and mass-7 and lower limits for mass-10 measured at different angles and bombarding energies while Figure III.5 shows the angular distributions. For mass-6 and mass-7, at the same bombarding energy, the angular distributions turn out to be similar both in the form and magnitude, generally monotomically decreasing with increasing angle.

Differential cross sections obtained this way agree with the cross sections given by the program Gas Cell (written by Dr. R. A. Paddock in this laboratory) to within 1.4%.

TABLE III.5a.--Differential Cross Sections (MB/SR) (E_p = 42 MeV).

	Lab. Angle (θ)	$\frac{d\sigma}{d\Omega}(\theta)$	Error (%)
Mass 6:	15.0	0.40374	19.4
	30.0	0.78126	14.2
	45.0	0.51040	23.1
	65.0	0.58811	15.3
	90.0	0.16257	70.0
Mass 7:	15.0	0.58397	13.7
	30.0	0.47428	24.7
	45.0	0.32170	33.6
	65.0	0.41696	22.6
	90.0	0.23884	40.8
Mass 10:	15.0	0.31275	16.5
	30.0	0.17936	65.3
	45.0	0.31810	32.1
	65.0	0.21667	43.6
	90.0	0.08831	88.1

TABLE III.5b.--Differential Cross Sections (MB/SR) (E_p = 40 MeV).

Mass 6:	10.0	0.56932	9.7
	17.0	0.42410	5.5
	17.0	0.44788	6.4
	30.0	0.48506	8.8
	30.0	0.40964	9.0
	37.0	0.38636	9.1
	45.0	0.24482	23.2
	50.0	0.33637	11.3
	60.0	0.29054	17.5
	70.0	0.21264	18.1
	80.0	0.23568	16.4
	90.0	0.15871	26.3
	100.0	0.14693	28.9
	100.0	0.11306	33
	110.0	0.11272	43.5
	125.0	0.05453	73.2

TABLE III.5b.--Cont.

	Lab. Angle (θ)	$\frac{d\sigma}{d\Omega}(\theta)$	Error (%)
Mass 7:	10.0	0.77269	6.4
	17.0	0.45030	8.1
	17.0	0.51125	4.8
	30.0	0.42168	9.6
	30.0	0.35882	9.4
	37.0	0.26535	13.1
	45.0	0.34236	12.9
	50.0	0.27076	16.1
	60.0	0.25229	17.9
	70.0	0.16078	24.8
	80.0	0.21552	18.0
	90.0	0.02897	77.4
	100.0	0.06905	59.5
	110.0	0.04196	11.7
	125.0	0.02994	32.8
Mass 10:	10.0	0.59674	5.7
	17.0	0.42534	3.0
	17.0	0.42232	4.2
	30.0	0.39365	4.6
	30.0	0.41657	5.0
	37.0	0.50122	5.1
	45.0	0.40889	6.4
	50.0	0.38812	7.4
	60.0	0.33612	9.8
	70.0	0.24168	12.4
	80.0	0.26782	9.1
	90.0	0.20784	17.5
	100.0	0.08522	19.4
	100.0	0.06338	43.2
	110.0	0.07240	10.1
	125.0	0.02780	37.9

TABLE III.5c.--Differential Cross Sections (MB/SR) (E_p = 35 MeV).

	Lab. Angle (θ)	$\frac{d\sigma}{d\Omega}(\theta)$	Error (%)
Mass 6:	15.0	0.66974	7.1
	20.0	0.25473	13.9
	30.0	0.28732	8.5
	45.0	0.17209	13.2
	60.0	0.13990	22.7
	60.0	0.14335	16.5
	75.0	0.18407	15.9
	90.0	0.06882	26.6
Mass 7:	15.0	0.62895	7.3
	20.0	0.21001	16.2
	30.0	0.15788	14.8
	45.0	0.18122	10.7
	60.0	0.10836	27.3
	60.0	0.07949	25
	75.0	0.15408	18.9
	90.0	0.06423	26.3
Mass 10:	15.0	0.48208	3.7
	20.0	0.25084	12.2
	30.0	0.12720	10.4
	45.0	0.13697	14.9
	60.0	0.16578	6.2
	60.0	0.15082	11.8
	75.0	0.10237	11.9
	90.0	0.06817	18.1

TABLE III.5d.--Differential Cross Sections (MB/SR) (E_p = 30 MeV).

Mass 6:	15.0	0.32729	4.2
	25.0	0.22388	7.2
	25.0	0.22293	3.6
	35.0	0.15373	5.7
	45.0	0.10010	5.2
	55.0	0.11815	18.9
	55.0	0.13333	13.2
	65.0	0.05769	14.2
	75.0	0.17192	13.7
	75.0	0.17627	10.0
	100.0	0.10285	14.4

TABLE III.5d.--Cont.

	Lab. Angle (θ)	$\frac{d\sigma}{d\Omega}(\theta)$	Error (%)
Mass 7:	15.0	0.25274	4.6
	25.0	0.18287	8.7
	25.0	0.16530	4.6
	35.0	0.11733	6.2
	45.0	0.08997	5.4
	55.0	0.09240	21.9
	55.0	0.11707	14.0
	65.0	0.04447	18.8
	75.0	0.09670	21.9
	75.0	0.12647	13.3
	100.0	0.07640	16.7
Mass 10:	15.0	0.52923	2.4
	25.0	0.12976	11.9
	25.0	0.10905	5.7
	35.0	0.05532	11.6
	45.0	0.04758	7.8
	55.0	0.03787	30.6
	55.0	0.04878	33.6
	65.0	0.02925	16.9
	75.0	0.07880	19.4
	75.0	0.06267	18.4
	100.0	0.01469	52.4

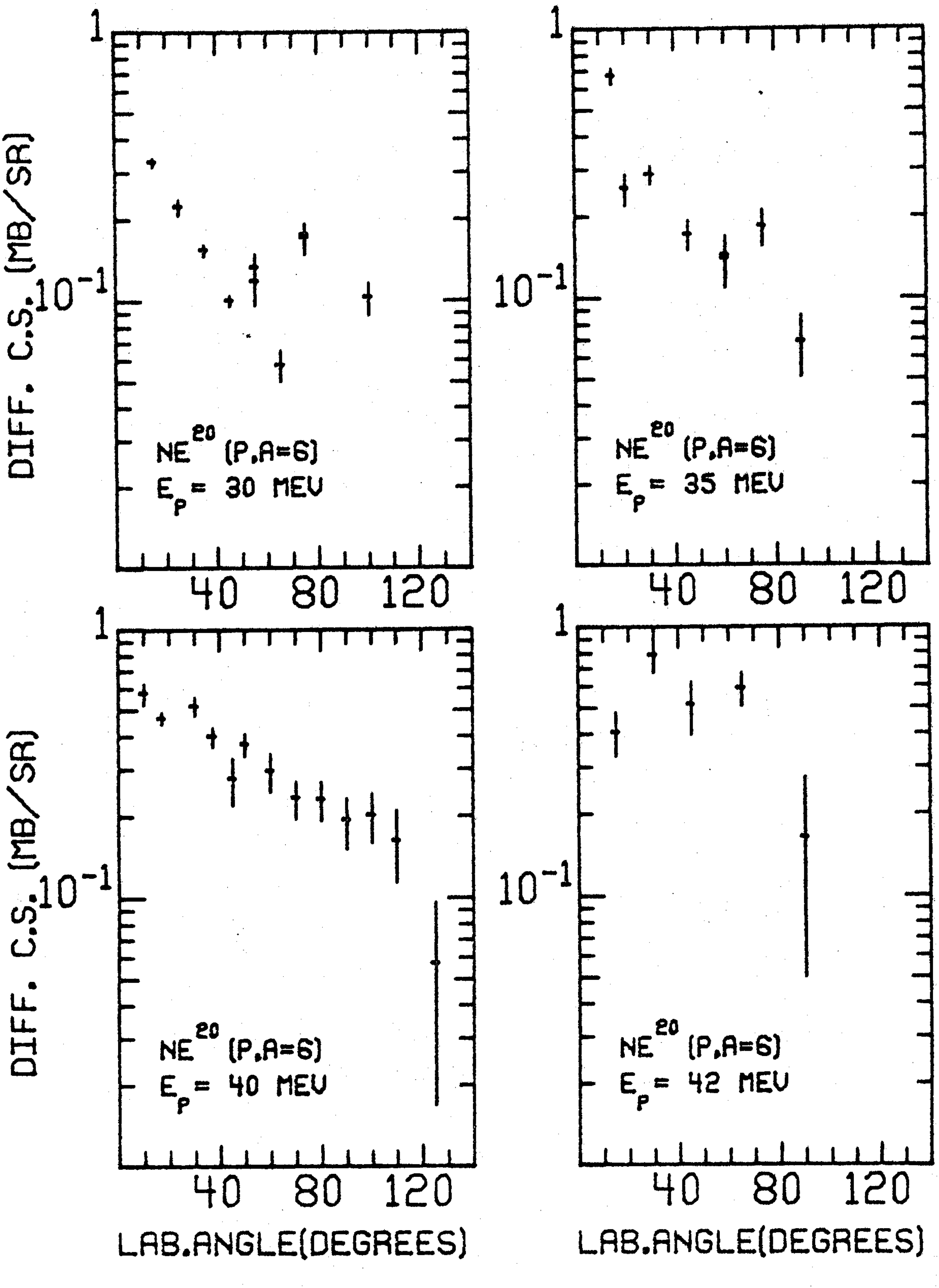

Fig. III.5a.--Angular Distributions for Mass-6. Ep = Bombarding Energy.

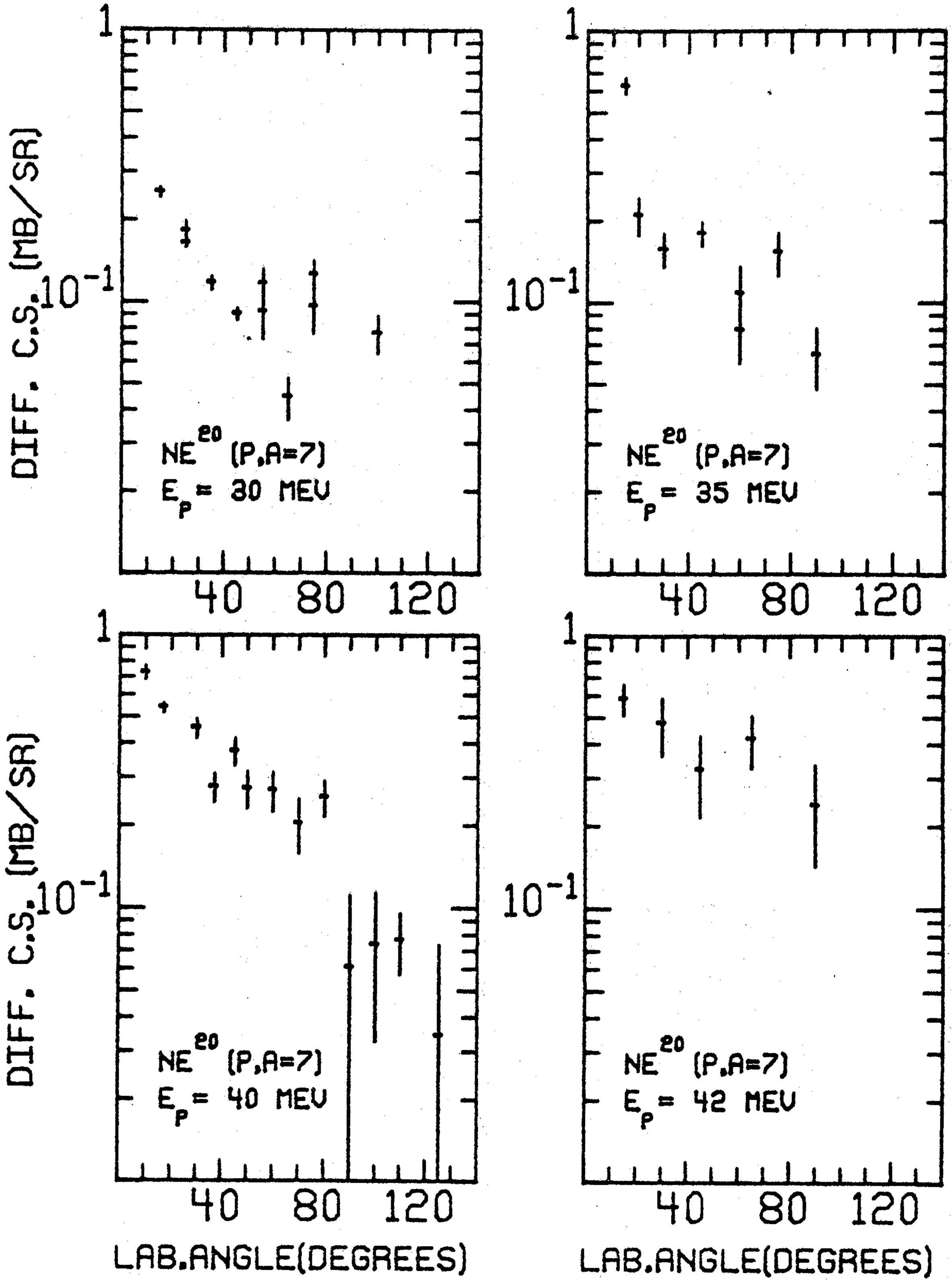

Fig. III.5b.--Angular Distributions for Mass-7. Ep = Bombarding Energy.

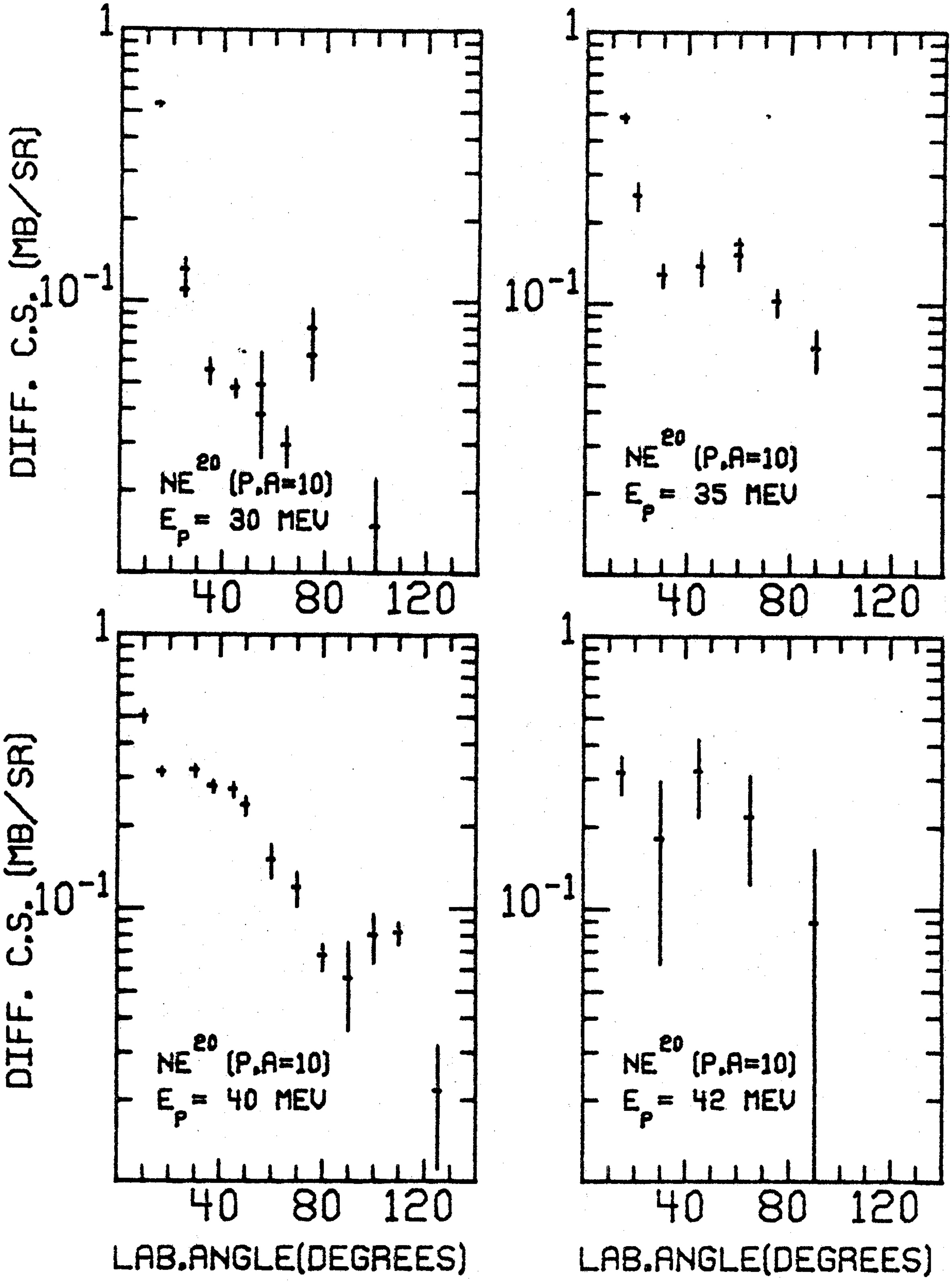

Fig. III.5c.--Angular Distributions for Mass-10. Ep = Bombarding Energy.

III.5 Total Cross Section

For each mass and bombarding energy the total cross section is calculated by summing the areas of the trapezoids under the straight lines connecting the points of the measured cross sections in the $\sigma(\theta)$ - cos (θ) plane. According to the formula

$$\sigma_T(E) = \int_0^{180} \sigma(\theta) \sin\theta d\theta d\phi$$

$$= 2\pi \int_0^{180} \sigma(\theta) \sin\theta d\theta$$

$$\sigma_T(E) = 2\pi \int_{-1}^{1} \sigma(\theta)\, d(\cos\theta)$$

where $\sigma(\theta)$ is the average value of both cross sections defining a trapezoid. For the backward angles for which there is no data taken it is assumed that the cross section is the same as the cross section at the largest angle where measurement is made. For 30 MeV it is 100 degrees in the laboratory system, for 35 and 42 MeV it is 90 degrees while for 40 MeV it is 125 degrees. It is also assumed that the cross section at 0 degrees is the same as it is at the smallest angle where the cross section is measured which is 10 degrees for 40 MeV and 15 degrees for the rest. Results of this calculation is listed in Table III.6 and plotted in Figure III.6.

TABLE III.6.--Integrated Cross Sections.

E_p (MeV)	Mass	σ(mb)	Tot. Error (%)	Contribution from Front[1] (%)	Contribution from Back (%)
42	6	4.1031	±28.8	2.1	24.9
	7	3.8861	±36.6	3.2	38.6
	10	1.9075	±46.0	3.5	29.1
40	6	2.4485	±21.2	2.2	6.0
	7	1.9142	±20.1	3.9	4.2
	10	2.5356	±11.4	2.2	2.9
35	6	1.6411	±24.8	3.9	26.3
	7	1.4017	±27.9	4.3	28.8
	10	1.3364	±24.5	3.4	32.1
30	6	1.5882	±25.1	4.4	33.6
	7	1.2156	±25.9	4.6	32.6
	10	0.65995	±25.7	17.2	11.6

[1] Front = Area in the σ(θ) - θ between θ = 0° and the smallest angle where measurement is made.
Back = Area between the largest angle (where measurement is made) and θ = 180°.

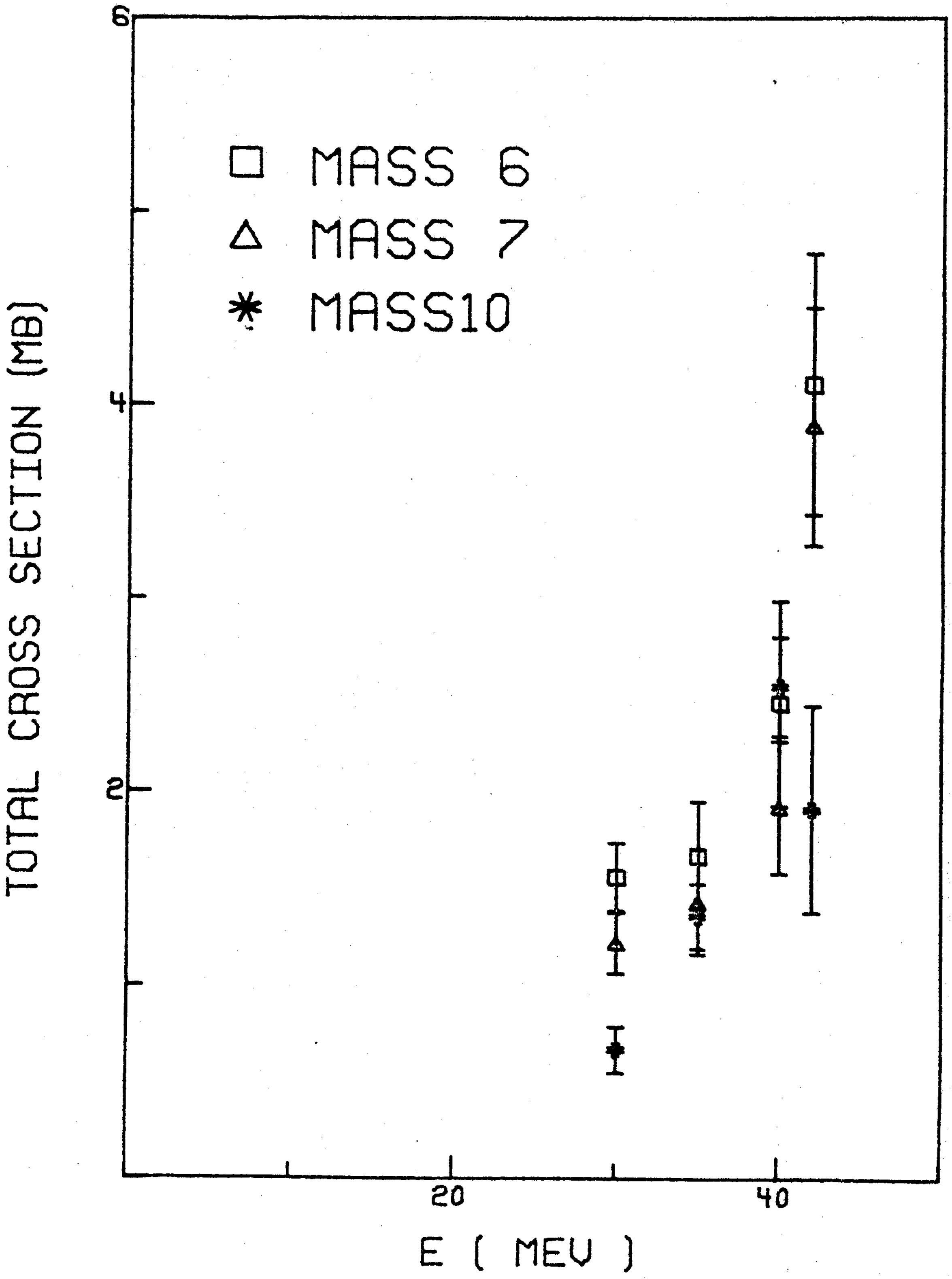

Fig. III.6.--Production Cross Sections for Mass 6, 7, and 10 from Proton Spallation of ^{20}Ne in the Energy Range E_p = 30 to 42 MeV.

To estimate the error in the integrated cross sections 50% of the contribution from front and back angles where there is no measurement made have been assigned as an error and included in the error tabulated in Table III.6 after combining it with the error of the differential cross sections. Systematic errors are listed in Table III.7.

TABLE III.7.--Systematic error in percent.

Source of Error	Error (%)	Measuring apparatus
Area of rear aperture	0.39	Traveling microscope
Front slit width	1.2 to 1.7	Feeler gauge
R distance between beam and Rear Aperture	1.0	Steel rule and micrometer
h distance between front and rear slit	0.3	Steel rule and micrometer
T temperature	1.5	
P gas pressure	0.17	Oil manometer
QFC integrated charge	3.0	Elcor A310B current integrator

Added in quadrature these errors contributions yield: 3.9%. This error is small compared to error due to the extrapolation of the cross sections to front and back angle (see Table III.6). The total error in Table III.6 includes both the statistical and the extrapolation error. If these error combined with the systematic error it is clear that latter is negligible. Due to the extrapolation procedure that was applied to the yield of mass-10, the numbers listed in Table III.6 for mass-10 are probably less reliable than the other results.

Chapter IV

CALCULATION OF THE PRODUCTION OF LI, BE, AND B IN THE SOLAR SYSTEM

IV.1 Previous Calculations

Even in the absence of the experimental cross section from ^{20}Ne H. E. Miller (Mi 70) and R. Bernas et al. (BGRS 67) have attempted to calculate the production of Li, Be, and B by spallation reactions.

H. E. Mitler assumes the galactic cosmic-ray particles coming on the CNONe targets in the interstellar medium to initiate nuclear reactions thereby producing Li, Be, and B. The contributions both from the reaction of protons on CNONe and from CNONe ions on hydrogen are taken into consideration. The production cross sections used in the calculation are mostly from the compilation by Audouze (AERS 67). Recently Epherre and Seide (ES 71) have published the cross section for ^{7}Be of ^{14}N from 13 through 40 MeV. It peaks to 40 mb at 20 MeV, contrary to the cross section used by Mitler which is a smoothly rising curve reaching the value of 10 mb at 10 GeV. Mitler attempted to account for the contribution from the α-reactions using cross section estimates based on the cross sections measured from ^{12}C, ^{14}N at 90 MeV (Jung 69) and at 100 through 137 MeV (Fo 71). The cross sections for α-reactions on ^{16}O and ^{20}Ne have been assumed to be equal to the corresponding cross section from ^{14}N. The reaction products are assumed to have a maximum path length of 4 g/cm^2. This reflects the fact that Li with energy greater than 120 MeV/nucleon (and hence range > 4g/cm^2) will escape the galactic disk and will not contribute to the abundance of lithium in the solar system. Taking into account also the possibility of an interchange between the interstellar medium and the material of the star as a function of time Mitler concludes that ^6Li, ^9Be, ^{10}B, and ^{11}B may be produced by spallation reactions initiated by the galactic cosmic ray particles on ^{12}C, ^{14}N, ^{16}O, and ^{20}Ne in the interstellar medium, but that the abundance of ^7Li remains unexplained.

Bernas et al. (BGRS 67) have examined a rather different mechanism. They assume that the protons in the solar cosmic rays are the bombarding particles and that the

C, N, O, and Ne in the photosphere are the targets. They assume the energy spectrum of the solar particle as being $E^{-\gamma}$, where E is the kinetic energy and γ is a constant taken to have a value that ranges from 3 to 5 according to the measurements of Freier and Webber (Fr 63). The cross section is assumed to be zero at energies lower than Q_{eff}, the threshold energy for the production of the maximum number of α particles, and equal to $\bar{\sigma}$, whose values are tabulated in Table IV.1, p. 127, for energy above Q_{eff}. They find that the production ratio for n11/n10 agrees with the observed solar system abundance ratio (4.0), while n7/n6 (2.5) is much too small compared to the observed ratio (12.5).

IV.2 Calculation of the Relative Production Rate of ^{6}Li and ^{7}Li Associated with Solar Flares

The production rate of a light element L (L represents ^{6,7}Li, ^{6}He, ^{7}Be) by the solar protons bombarding the target M (M represents ^{12}C, ^{14}N, ^{16}O, ^{20}Ne) in the solar surroundings can be expressed as follows:

$$PR(L) = 4\pi \sum_M n_M \int_{E_{thres}}^{E_{max}} \phi_p(E)\ \sigma_{L,M}(E)\ dE \quad (\mathrm{sec}^{-1})$$

where: $PR(L)$ = production rate of the element L

n_M = relative abundance of the element M in the solar system

$\phi_p(E)$ = proton flux in the solar cosmic rays $(\mathrm{sec\text{-}cm^2\text{-}ster\text{-}MeV/sec})^{-1}$

$\sigma_{L,M}(E)$ = production cross section of the element L by proton bombardment of the target M at bombarding energy E(cm^2)

E_{thres} = threshold energy for the nuclear reaction M(p,)L

E_{max} = maximum value for the energy used in the integration

The values for n_M are available in the literature. Bernas et al. (BGRS 67) used the ratios $n_C:n_N:n_O:n_{Ne}$ = 30:1:10:30, while Mitler (Mi 70) used another set of values, i.e. $n_C:n_N:n_O:n_{Ne}$ = 3.7:1:6.5:0.78. The abundance of these elements in the solar cosmic rays has also been measured. Bertsch et al. (Be 72) reported the abundances of the same elements in the solar cosmic rays as $n_C:n_N:n_O:n_{Ne}$ = 2.95:1:5.26:0.84. In this section the calculation is carried out for the values of both Mitler and Bertsch et al.

The flux of solar protons has also been measured. The variation of flux with energy can be expressed in several ways. In the early work it was represented as an exponential function of the rigidity R (the momentum per unit charge) of the proton, $\exp(-R/R_O(t))$, where R is the rigidity of the proton and $R_O(t)$ is the characteristic rigidity. The value of R_O depends on time, i.e. on the age of the flare activity and seems to vary from one flare to another (Fr 63). The characteristic rigidity gets smaller as the flare activity gets older, i.e. the rigidity spectrum peaks more strongly to the low energy region as the flare activity progresses (Fr 63).

More recently, it has become common to describe the spectrum by a power law $E^{-\gamma}$ (Fr 63, Hs 70, Be 72) where E is the energy of the proton and γ is a constant whose value differs from one event to another. Simpson (Si 70) has observed proton spectra over the period of June 1966 to January 1967 with values for γ that range from 1.6 to 5.6.

The production cross sections for the isobars A = 6, A = 7, A = 10, and A = 11 have been collected. They are tabulated in Table IV.2, p. 128, and plotted in Figure IV.1. Out of this collection I have chosen a set of cross sections for each of the isobars A = 6 and A = 7 to be used in this calculation (see Figure IV.2).

The procedure followed in choosing the cross section has been to compare with the rest of the data over a wide energy range. Data that follow the general trend are favored over those which do not. The latest data by the same author are favored over his old ones. Where there is no data available I either have consulted the calculated value by Bernas et al. (for the high energy region E > 150 MeV) or made an interpolation. In either case a fifty percent error is assigned.

In the low energy region, from the threshold to 42 or 44 MeV, data are available in the form of isobaric cross sections. (The data of Epherre et al. (ES 71) on ^{14}N was actually measured for ^{7}Be only, but other mass-7 producing reactions are not energetically allowed below 30 MeV.)

For ^{12}C, the $\sigma(^{6}He + ^{6}Li)$ data of Davids et al. are used below 50 MeV (Da 70). At higher energies $\sigma(^{6}Li)$ is taken from Table IV.2 and $\sigma(^{6}He)$ is taken to be 0.5 mb (BGRS 67). For A = 7 there are isobaric yield data available for the energy range 28 to 44 MeV (Da 70) and together with $\sigma(^{7}Be)$ from Table IV.2 $\sigma(^{7}Li)$ is

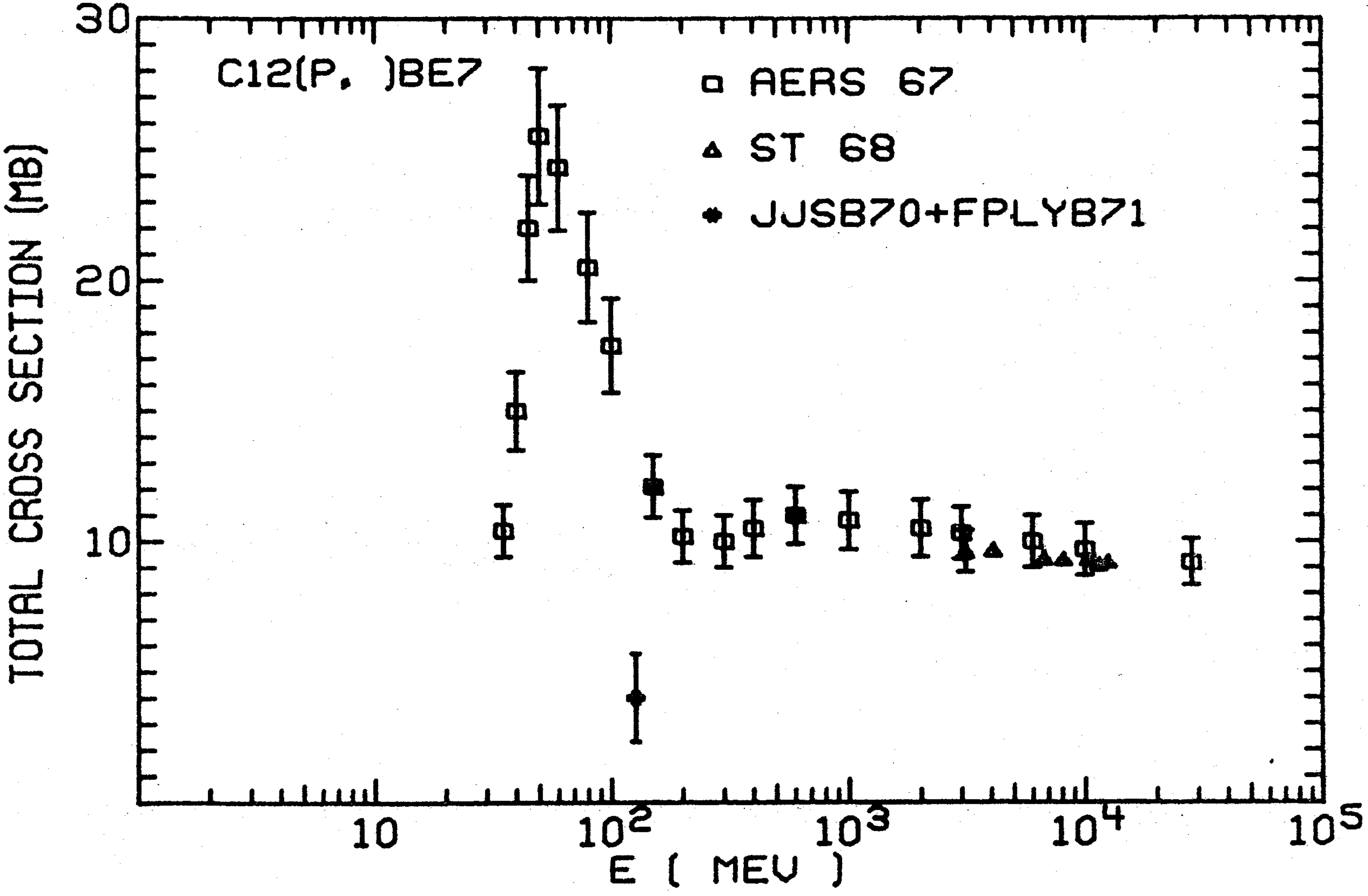

Fig. IV.1.--Production Cross Sections as a Function of Energy.

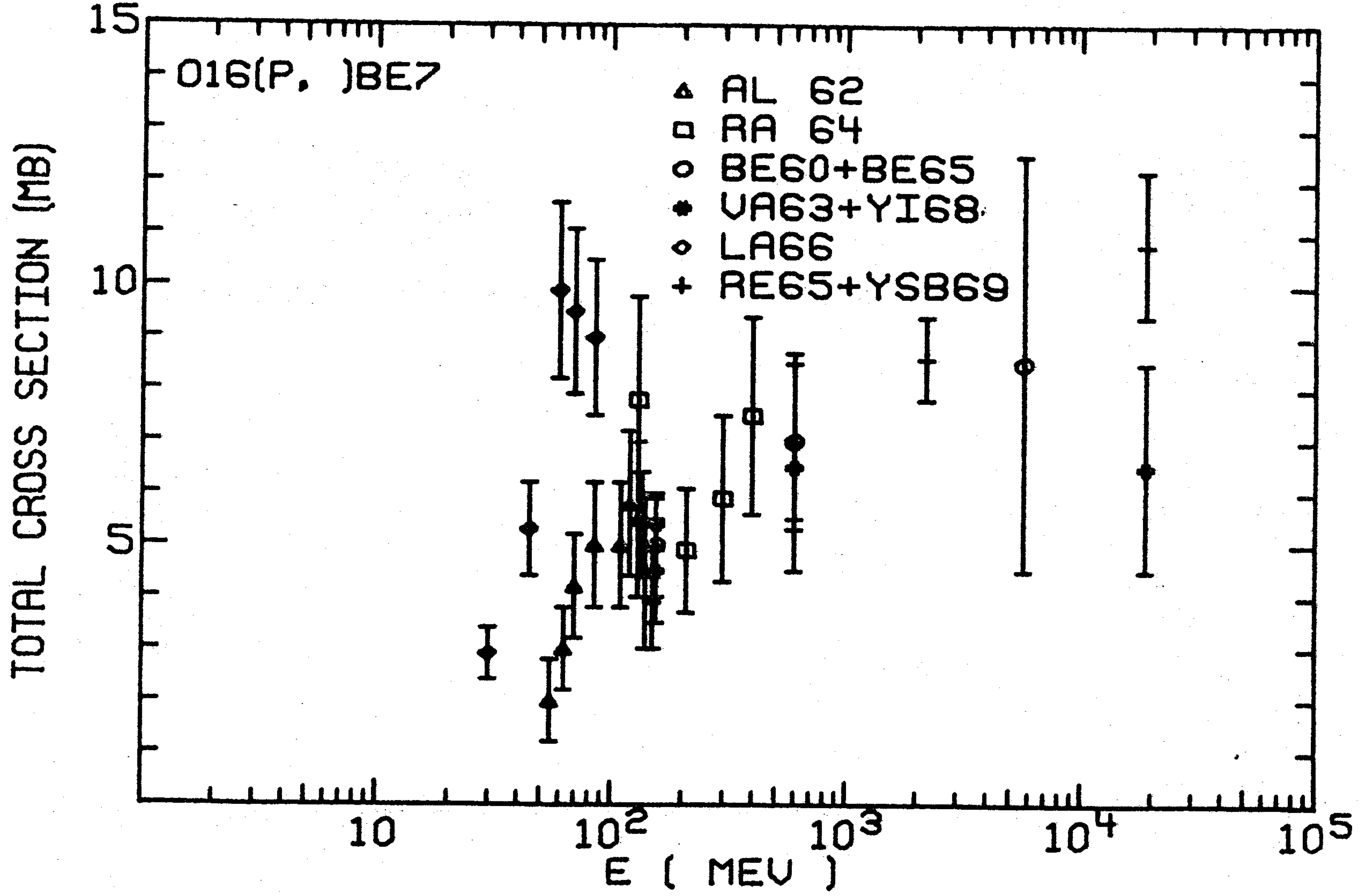
O16(P,)BE7
▲ AL 62
□ RA 64
○ BE60+BE65
✱ VA63+YI68
◇ LA66
+ RE65+YSB69
TOTAL CROSS SECTION (MB)
15
10
5
10
10^2
10^3
10^4
10^5
E (MEV)

Fig. IV.1.--(cont.)

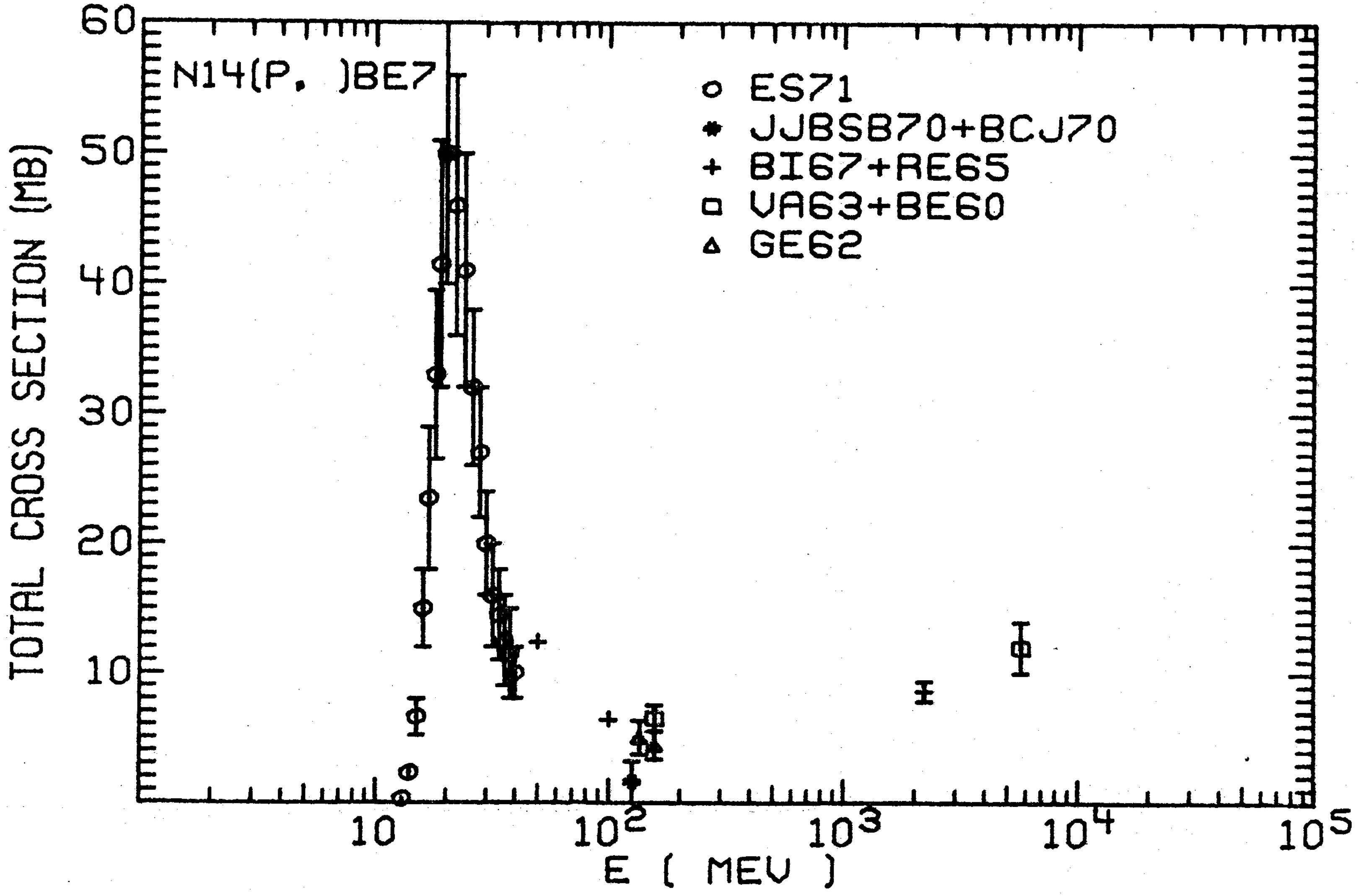
N14(P,)BE7
ES71
JJBSB70+BCJ70
BI67+RE65
VA63+BE60
GE62
TOTAL CROSS SECTION (MB)
60
50
40
30
20
10
10
10^2
10^3
10^4
10^5
E (MEV)

Fig. IV.1.--(cont.)

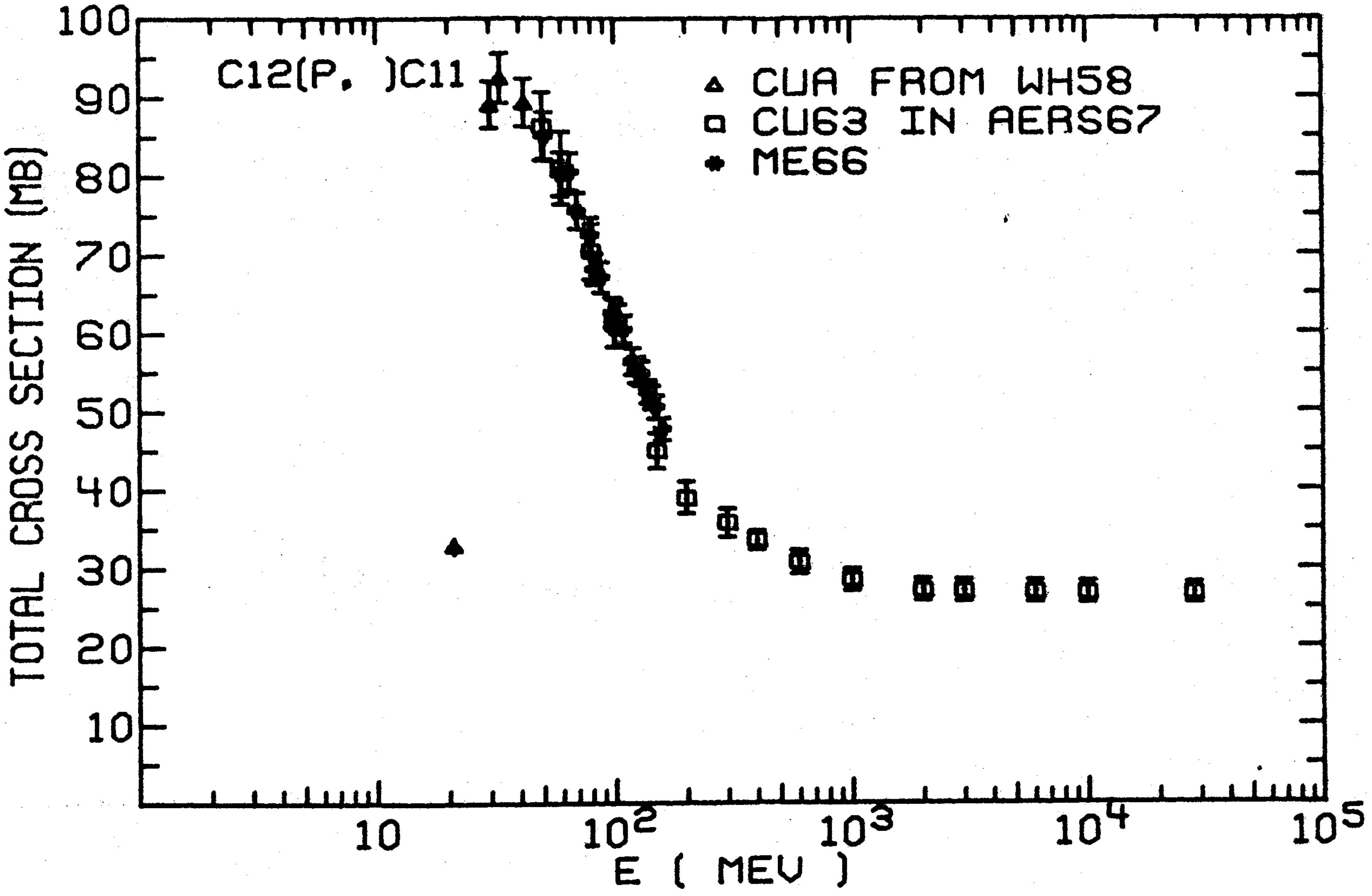
C12(P,)C11
▲ CUA FROM WH58
□ CU63 IN AERS67
✱ ME66
TOTAL CROSS SECTION (MB)
100
90
80
70
60
50
40
30
20
10
10
10^2
10^3
10^4
10^5
E (MEV)

Fig. IV.1.--Cont.

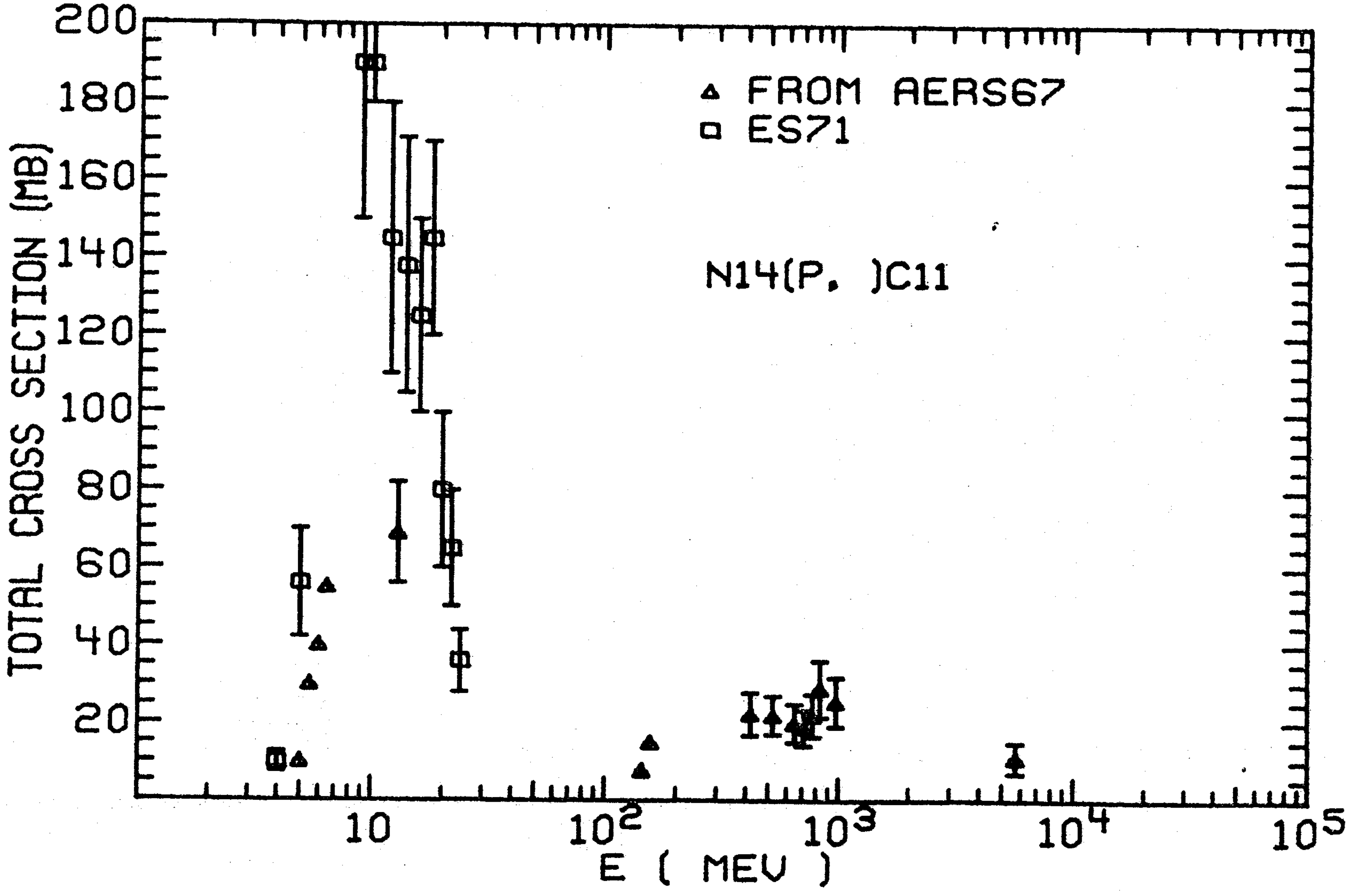
TOTAL CROSS SECTION (MB)
200
180
160
140
120
100
80
60
40
20
E (MEV)
10
10^2
10^3
10^4
10^5
▲ FROM AERS67
□ ES71
N14(P,)C11

Fig. IV.1.--ĉont.)

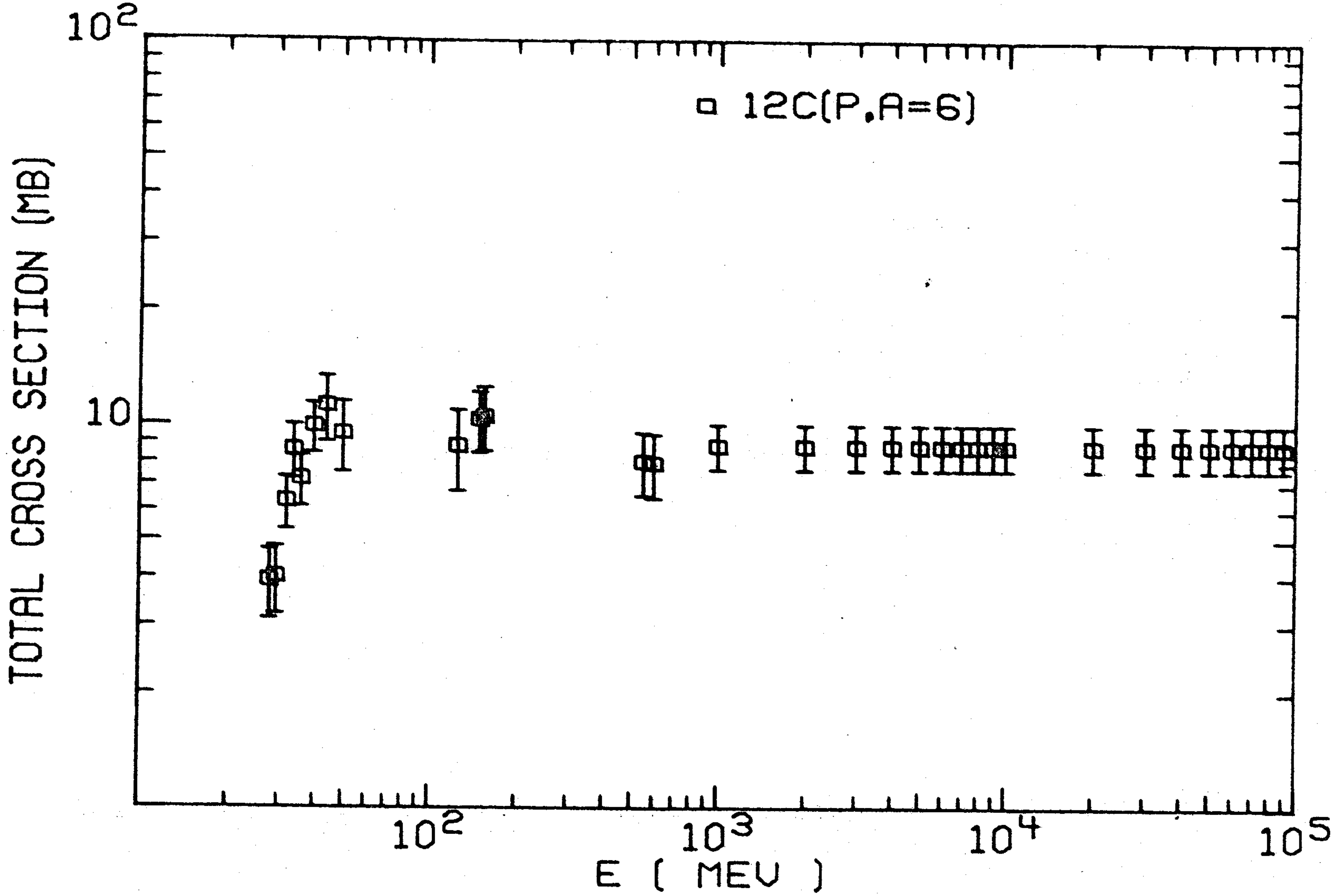

Fig. IV.2.--Production Cross Sections Used for the Calculation of the Production Rate of Lithium.

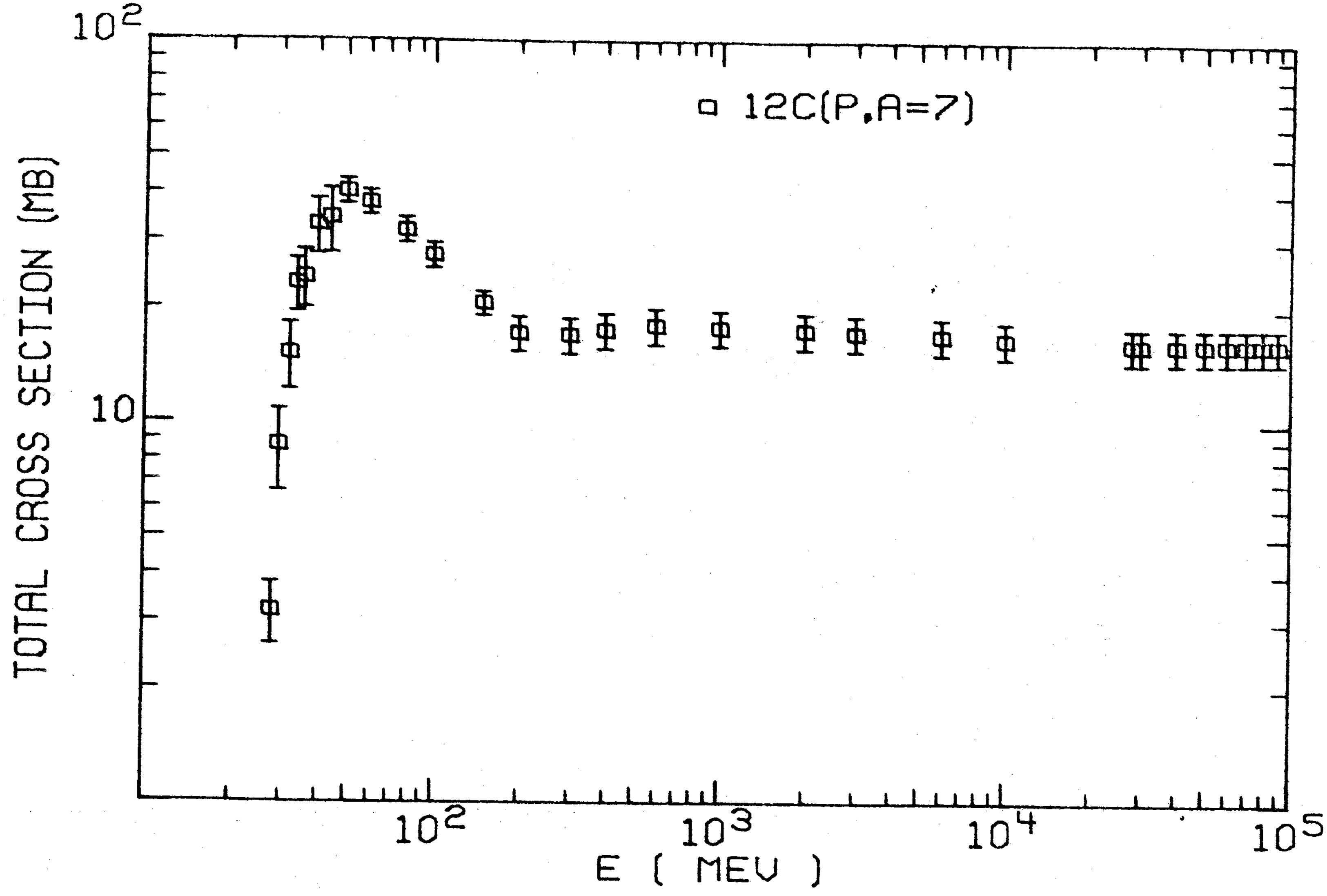

Fig. IV.2.--(cont.)

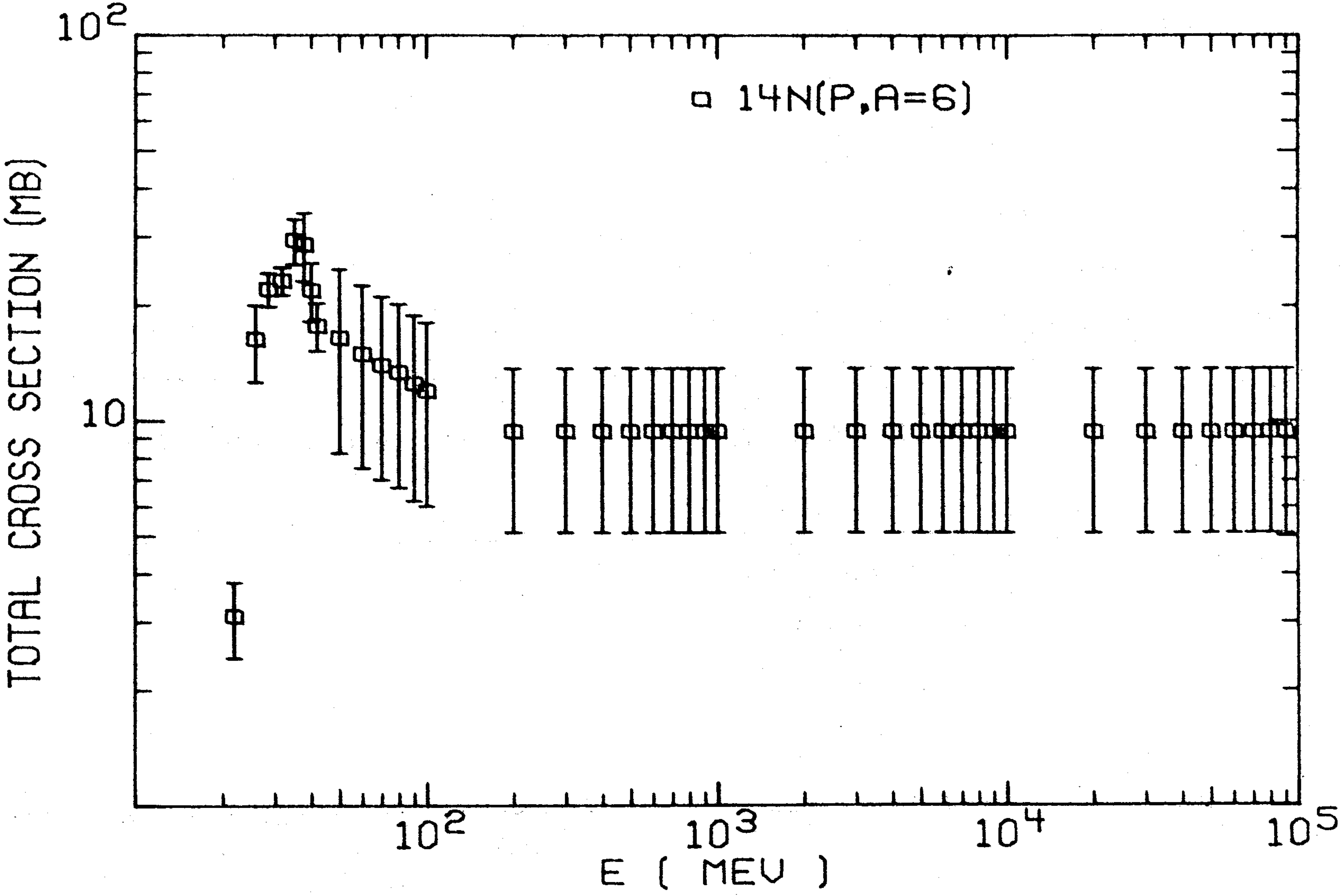

Fig. IV.2.--(cont.)

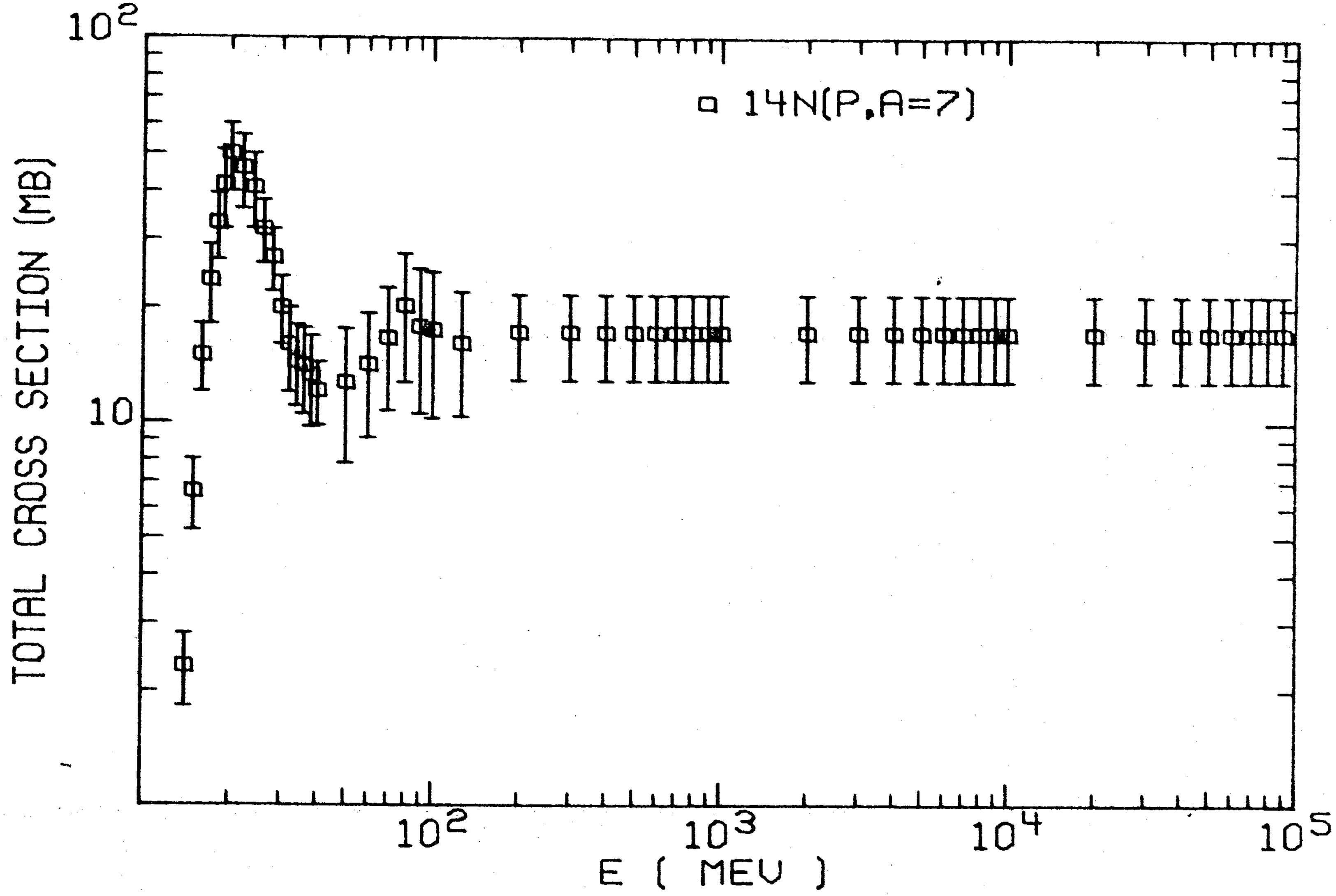

Fig. IV.2.--(cont.)

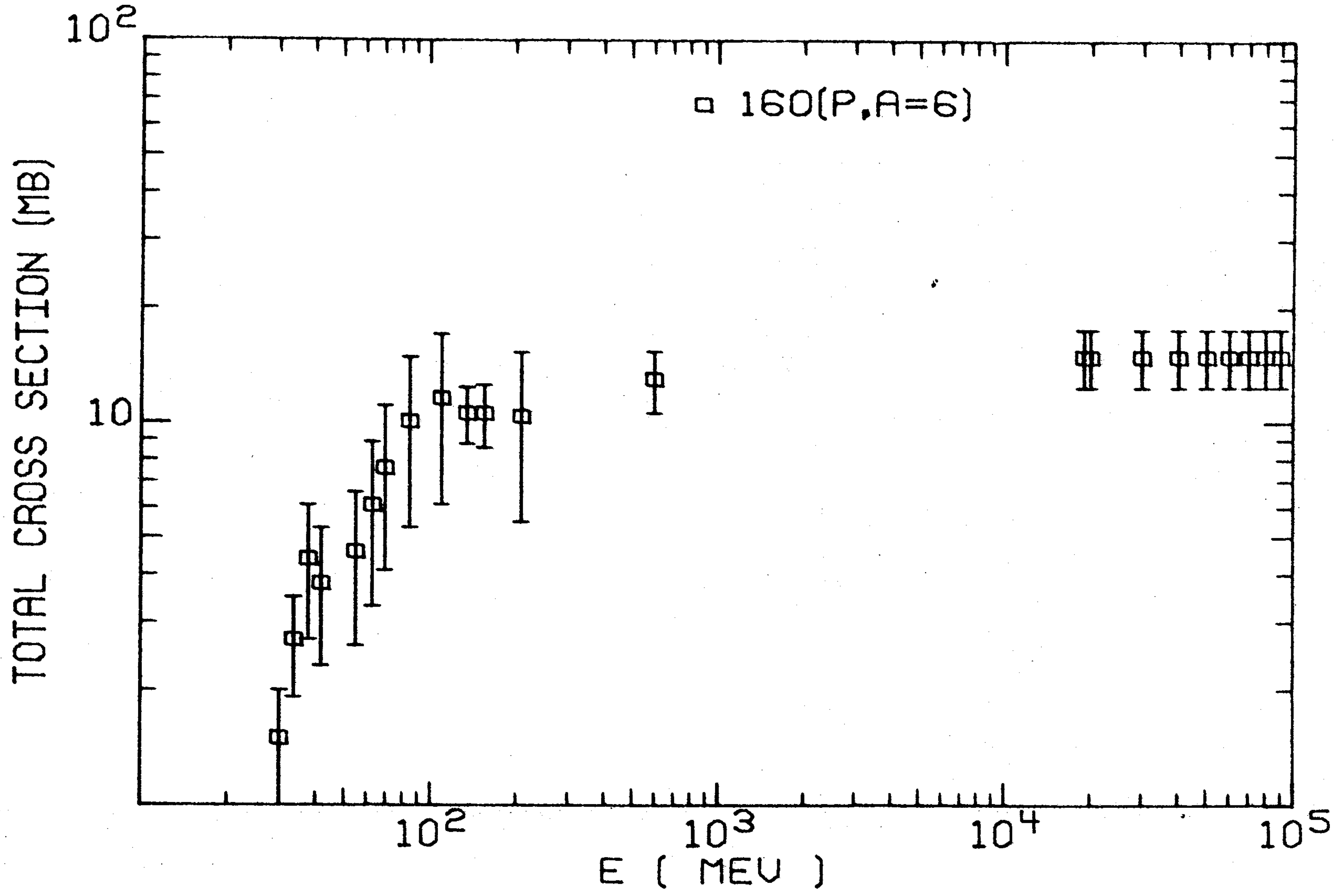

Fig. IV.2.--(cont.)

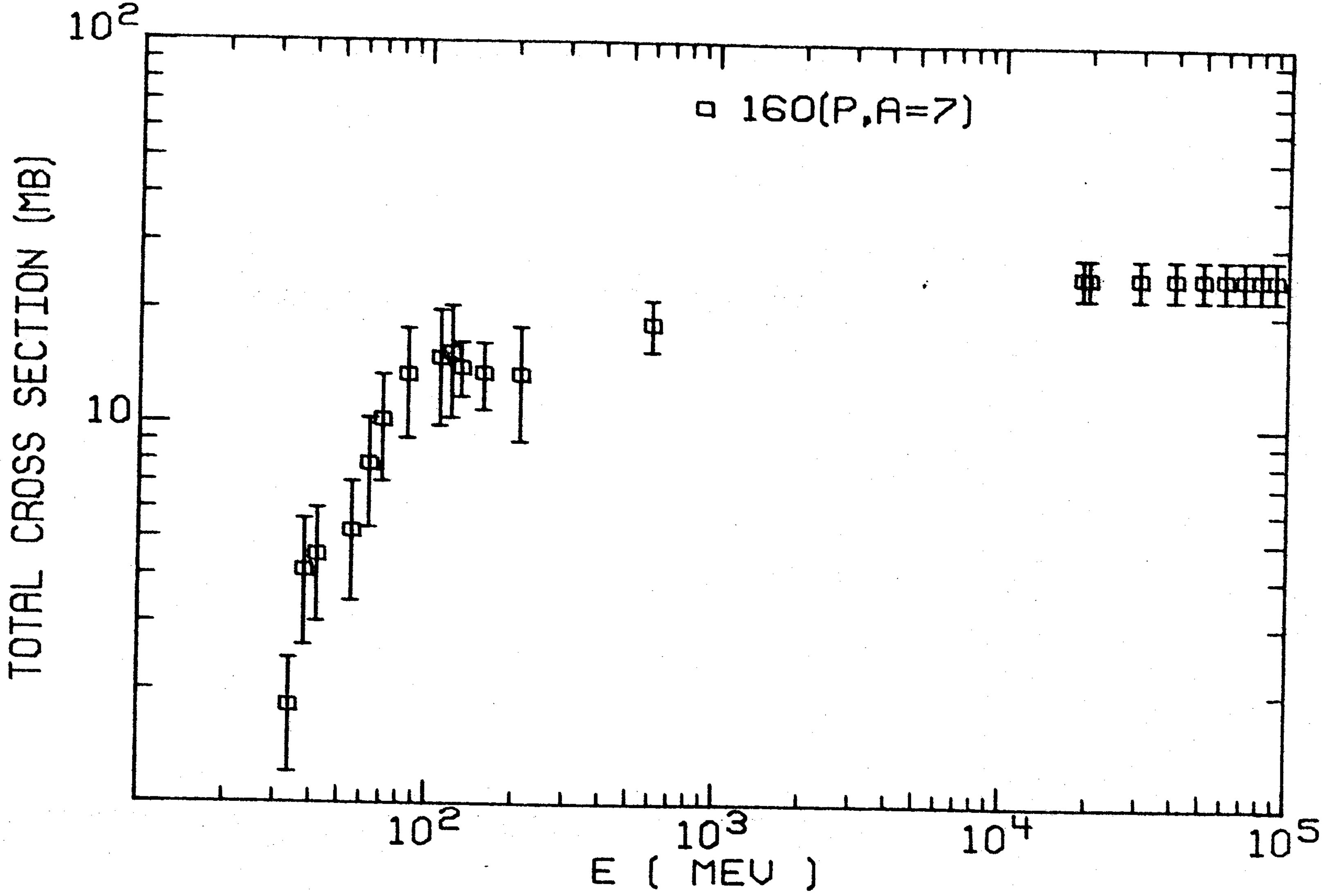

Fig. IV.2.--(cont.)

constructed by subtracting $\sigma(^7Be)$ from $\sigma(^7Li + ^7Be)$. For energy higher than 155 MeV $\sigma(^7Li) = (7 \pm 1.5)$ mb (BGRS 67) while for energy between 44 and 155 MeV I assume the cross sections follows a straight line in a log-log scale. Table IV.2 supplies $\sigma(^7Be)$. These chosen cross sections are plotted in Figure IV.2.

With the similar procedure the cross sections from ^{14}N are constructed. The data by Laumer (La 71) and Epherre et al. (ES 71) are used to construct $\sigma(^7Li)$. At high energy the estimated values for $\sigma(^6Li)$, $\sigma(^7Li)$, and $\sigma(^7Be)$ are all 10 mb (BGRS 67) but the measured value for $\sigma(^7Be)$ at 2200 MeV is (8.6 ± 0.8) mb (see Table IV.2, p. 128) and hence I have assumed that $\sigma(^6Li) = \sigma(^7Li) = \sigma(^7Be) = (8.6 \pm 0.8)$ mb. The maximum value of the cross sections for ^6Li and ^7Li have been assumed to be equal to 1.5 times the value of the cross section at high energy, and the value of $\sigma(^6He)$ is taken to be 0.8 mb (BGRS 67).

In the calculation by Mitler (Mi 70) the cross sections for ^6Li, ^7Li, and ^7Be from ^{16}O are plotted. They are taken from the compilations by Audouze (see Table IV.2, p. 128). His extrapolation to lower energy is comparable to the data by Laumer (La 71) and hence I have used those values in this calculation and taken $\sigma(^{6}\text{He})$ to be 0.6 mb (BGRS 67).

The cross sections from ^{20}Ne and ^{16}O between 30 and 42 MeV are comparable. Furthermore there is no known resonance in the proton reactions on both ^{16}O and ^{20}Ne that lead to the production of any of these isobars and hence it is expected that the excitation function for such isobars, in both cases, will be smooth and similar. Based on these considerations I have assumed for the purpose of this calculation that the cross section from ^{20}Ne and ^{16}O are equal.

The integration is carried out from the threshold energy up to 100 BeV (contributions from higher energies are negligible) and the ratio of the production rate is calculated for $\gamma = 1.5$ to 7.2 for the solar abundances by Bertsch (Be 72) and up to 7.4 for the abundances of Mitler (Mi 70).

The ratio of the production rate for the isobar A = 7 and A = 6, PR(7)/PR(6), rises from 1.6 for $\gamma = 1.5$ in both cases to 14 for $\gamma = 7.2$ or 7.4 respectively. The value 12.5 for the production rate is obtained for $\gamma = 7.1$ with Bertsch's solar abundance data and for $\gamma = 7.2$ with Mitler's solar abundance data (see

Table IV.3, p. 139). This value is comparable to the value for chondritic meteorites which is 12.2.

This value of γ seems to be high compared to the highest observed value of 5.6 (Si 70). It is somewhat premature, however, to make any strong comment on the value $\gamma = 7.2$ without knowing more about the cross sections from the relevant targets at higher energy.

Table IV.3, p. 139, shows that the production rate ratio increases as the value of γ increases which behavior has also been shown by Laumer (La 71) where the contributions of ^{20}Ne to the production rate was ignored, the difference being the slower rate of increase of the ratio in this calculation.

According to the model of Wagoner, Fowler, and Hoyle (WFH 67) a certain amount of Li can also be produced in the primeval big-bangs. This will decrease the production ratio PR(7)/PR(6) required from the spallation reactions and will permit production at a lower γ.

Regardless of the value of γ that will lead to the correct production ratio, however, it is clearly seen that the later stage of the flare activity is very important in the matter of production ratio, so it is important to know the value of γ as a function of time, and do the calculation of the production rate as an average over time.

TABLE IV.1.--Average Cross Section (in mb) for the Production of Li, Be, B by Spallation of CNONe.[1]

		^{6}Li	^{7}Li	^{7}Be	^{9}Be	^{10}B	^{11}B	^{11}C
^{12}C	$\bar{\sigma}$	10	7	12	2	10	16	60
^{14}N	$\bar{\sigma}$	10	10	10	2	10	10	30
^{16}O	$\bar{\sigma}$	10	12	4	2	10	10	15
^{20}Ne	$\bar{\sigma}$	8	8	8	2	12	12	12

[1] Taken from (BGRS 67).

TABLE IV.2a.--Proton Spallation Cross Sections (MB) for ^{6}Li.

Target	E(MeV)	$\sigma(^{6}Li)$	Refer.	Remarks:
^{12}C	44	11 ± 2	Be 65	[1]*, Brochure on Survey of Spallation Cross Section by Andouze et al.
	50	9 ± 2	"	*, Brochure on Survey of Spallation Cross Section by Andouze et al.
	155	10 ± 2	"	*, Brochure on Survey of Spallation Cross Section by Andouze et al.
	550	7.5 ± 1.5	"	Brochure on Survey of Spallation Cross Section by Andouze et al.
	3000	8.3 ± 1.2	Kl 67	
	126	8.3 ± 2.1	JJBSB70	
	150	9.8 ± 1.9	FPLYB71	
	600	7.4 ± 1.5	"	
^{14}N	126	12.7 ± 4.9	JJBSB70	
^{16}O	155	10 ± 2	Yi 68	
	600	18 ± 5	"	
	155	10 ± 2	Be 65	
	600	12.4	Yi 67	
	19000	14.1	"	
	135	10 ± 1.8	YSB 69	
	600	12.4 ± 2.4	"	
	19000	14.4 ± 2.6	"	
	135	10 ± 2	YBDFGB68	

[1] *means: Data have been renormalized a la Cumming (Cu 63).

TABLE IV.2b.--Proton Spallation Cross Section (MB) for ^{7}Li.

Target	E(MeV)	$\sigma(^{7}\text{Li})$	Refer.	Remarks:
^{12}C	44	11 ± 2	Be 65	Brochure on Survey of Spallation Cross Section by Andouze et al.
	50	7 ± 1.5	"	Brochure on Survey of Spallation Cross Section by Andouze et al.
	155	8 ± 1.7	"	Brochure on Survey of Spallation Cross Section by Andouze et al.
	550	5.6 ± 1.2	"	Brochure on Survey of Spallation Cross Section by Andouze et al.
	3000	9.1 ± 1.4	Kl 67	Brochure on Survey of Spallation Cross Section by Andouze et al.
	126	6.5 ± 1.9	JJBSB70	
	150	7.8 ± 1.6	FPLYB71	
	600	5.6 ± 1.1	"	
^{14}N	126	9.5 ± 4.2	JJBSB70	
^{16}O	155	8.5 ± 2.5	Yi 67	
	600	11.3	"	
	19000	13.9	"	
	135	8.5 ± 1.7	YSB 69	
	600	11.3 ± 2.2	"	
	19000	14.2 ± 2.7	"	
	135	8.0 ± 2.5	YBDFGB68	

TABLE IV.2c.--Proton Spallation Cross Sections (MB) for ^{7}Be.

Target	E(MeV)	$\sigma(^{7}\text{Be})$	Refer.	Remarks:
^{12}C	35	10.4 ± 1	AERS 67	*, from Br 62
	40	15 ± 1.5	"	*, from Br 62
	45	22 ± 2	"	*, from Br 62
	50	25.5 ± 2.6	Cu 63	
	60	24.3 ± 2.4	AERS 67	
	80	20.5 ± 2.1	"	
	100	17.5 ± 1.8	"	
	150	12.1 ± 1.2	"	
	200	10.2 ± 1.0	"	
	300	10.0 ± 1.0	"	
	400	10.5 ± 1.1	"	
	600	11.0 ± 1.1	"	
	1000	10.8 ± 1.1	"	
	2000	10.5 ± 1.1	"	
	3000	10.3 ± 1.0	"	
	6000	10.0 ± 1.0	"	
	10000	9.7 ± 1.0	"	
	28000	9.2 ± .9	"	
	3100	9.6 ± .8	ST 68	
	4100	9.65	"	
	6700	9.35	"	
	8100	9.3	"	
	10300	9.3	"	
	11500	9.1	"	
	12500	9.2	"	
	126	4.0 ± 1.7	JJBSB70	
	150	12.1 ± 1.2	FPLYB71	
	600	11.0 ± 1.1	"	
	155.0	9.5	Wi 67	
	150.3	9.4	"	
	145.3	8.9	"	
	139.6	9.9	"	
	134.0	10.3	"	
	128.2	10.8	"	
	122.3	10.8	"	
	116.0	10.8	"	
	109.6	11.6	"	
	102.9	11.4	"	
	95.7	11.6	"	

TABLE IV.2c.--Cont.

Target	E(MeV)	$\sigma(^{7}Be)$	Refer.	Remarks:
	88.0	11.7	Wi 67	
	80.0	12.7	"	
	71.2	13.9	"	
	61.5	14.6	"	
	60.0	15.5	"	
	59.0	16.0	"	
	56.0	16.3	"	
	53.3	18.5	"	
	53.1	16.9	"	
	50.5	17.3	"	
	47.0	19.1	"	
	47.0	18.0	"	
	44.6	18.5	"	
	41.5	18.9	"	
	39.5	19.2	"	
	37.5	19.3	"	
	35.8	18.2	"	
	34.0	16.3	"	
	31.9	11.1	"	
	29.8	3.4	"	
	27.4	0.42	"	
	24.5	0.05	"	
^{14}N	21	50	BCJ 70	
	50	12.4	Bi 67	
	100	6.4	Bi 67	
	2200	8.6 ± .8	Re 65	
	126	1.6 ± 1.6	JJBSB70	
	13	.32± .08	ES 71	Read from a graph
	14	2.3 ± .5	"	
	15	6.6 ± 1.4	"	
	16	15.0 ± 3.0	"	
	17	23.5 ± 5.5	"	
	18	33.0 ± 6.5	"	
	19	41.5 ± 9.5	"	
	20	50.0 ±10.0	"	
	22	46.0 ±10.0	"	
	24	41.0 ± 9.0	"	
	26	32.0 ± 6.0	"	
	28	27.0 ± 5.0	"	
	30	20.0 ± 4.0	"	

TABLE IV.2c.--Cont.

Target	E(MeV)	$\sigma(^7Be)$	Refer.	Remarks:
	32	16.0 ± 4.0	ES 71	
	34	14.5 ± 3.5	"	
	36	12.5 ± 3.5	"	
	38	11.5 ± 3.5	"	
	40	10.0 ± 2.0	"	
^{16}O	55	3 ± .8	Al 62	From AERS 67
	63	3 ± .8	"	"
	70	4.2 ± 1	"	"
	85	5 ± 1.2	"	"
	110	5 ± 1.2	"	"
	120	5.8 ± 1.4	"	"
	130	5.5 ± 1.5	"	"
	130	7.8 ± 2	Ra 64	"
	140	4.5 ± 1.5	Al 62	"
	150	4 ± 1	"	"
	155	4.5 ± 1	Va 63	"
	155	5 ± 1	Be 65	"
	208	4.9 ± 1.2	Ra 64	"
	297	5.9 ± 1.6	"	*, From AERS 67
	396	7.5 ± 1.9	"	"
	600	7 ± 1.5	Be 65	"
	5700	8.5 ± 4	Be 60	*, From AERS 67
	155	5.4 ± .5	Yi 68	"
	600	6.5 ± 2	"	"
	19000	6.5 ± 2	"	"
	30	2.9 ± .5	La 66	
	45	5.3 ± .9	"	
	60	9.9 ± 1.7	"	
	70	9.5 ± 1.6	"	
	85	9.0 ± 1.5	"	
	2200	8.8 ± .4	Re 65	
	19000	10.8 ± 1.4	Yi 67	
	135	5.4 ± 1	YSB 69	
	600	7.0 ± 1.7	"	
	19000	10.8 ± 1.4	"	

TABLE IV.2d.--Proton Spallation Cross Sections (MB) for ^{9}Be.

Target	E(MeV)	$\sigma(^{9}Be)$	Refer:	Remarks
^{12}C	126	2.5 ± 1.0	JJBSB 70	
	150	3.2 ± 0.4	FPLYB 71	
	600	5.3 ± 0.7	"	
^{14}N	126	4.8 ± 2.8	JJBSB 70	
^{16}O	155	1.7 ± 0.5	Yi 68	
	600	2.4 ± 1.2	"	
	19000	2.2 ± 1.1	"	
	135	1.9 ± 0.6	YBDFGB 68	
	135	1.7 ± 0.5	"	
	600	2.4 ± 1.2	"	
	19000	2.2 ± 1.1	"	
	135	1.7 ± 0.4	YSB 69	
	600	2.6 ± 0.9	"	
	1000	3.6 ± 1.0	"	

TABLE IV.2e.--Proton Spallation Cross Sections (BM) for ^{10}Be.

Target	E(MeV)	$\sigma(^{10}Be)$	Refer.	Remarks
^{12}C	220	2.2 ± 0.8	Ho 64	*, AERS 67
	126	<0.4	JJBSB 70	
	150	1.1 ± 0.1	FPLYB 71	
	600	2.8 ± 0.4	"	
^{14}N	126	1.6 ± 1.6	JJBSB 70	
^{16}O	155	0.37 ± 0.20	Yi 68	
	600	0.6 ± 0.4	"	
	19000	0.64 ± 0.50	"	
	135	0.35 ± 0.20	YBDFGB 68	
	600	0.60 ± 0.40	"	
	19000	0.64 ± 0.50	"	

TABLE IV.2f.--Proton Spallation Cross Sections (MB) for ^{10}B.

Target	E(MeV)	$\sigma(^{10}B)$	Refer..	Remarks
^{12}C	150	> 6	Cl 61	
^{14}N	150	> 3	Cl 61	
^{16}O	155	11 ± 3	Yi 68	
	600	12 ± 5	"	
	146	> 12	Fo 62	
	135	11 ± 3	YBDFGB 68	
	600	12 ± 5	"	

TABLE IV.2g.--Proton Spallation Cross Sections (MB) for ^{10}C.

Target	E(MeV)	$\sigma(^{10}C)$	Refer.	Remarks
^{12}C	143	2.8 ± 1.3	Cl 61	AERS 67, *
	156	2.6 ± 0.3	Va 63	" , *
	365	3.7 ± 0.4	Sy 57	" , *
	420	3.5 ± 0.3	"	" , *
	522	3.3 ± 0.3	"	" , *
	648	3.2 ± 0.3	"	" , *
	832	2.9 ± 0.2	"	" , *
	980	3.3 ± 0.3	"	" , *
^{14}N	156	1.6 ± 0.3	Va 63	"
^{16}O	155	1 ± 0.2	"	"
	420	6 ± 2	Sy 57	" , *
	980	4 ± 0.2	"	" , *

TABLE IV.2h.--Proton Spallation Cross Sections (MB) for ^{11}B.

Target	E(MeV)	$\sigma(^{11}B)$	Refer.	Remarks:
^{12}C	153	16 ± 4	Go 60	
	120-150	2.8 ± 1.1	Au 62	
	660	<28 ± 2	Zh 60	From the Supplement of Survey of C.S. by Audouze et al.
^{16}O	155	25 ± 8	Yi 68	
	600	25 ± 12	"	
	135	25 ± 8	YBDFGB 68	
	600	25 ± 8	"	

TABLE IV.2i.--Proton Spallation Cross Sections (MB) for ^{11}C.

Target	E (MeV)	$\sigma(^{11}C)$	Refer.	Remarks:
^{12}C	21.1	32.9 ± 1.1	Cu 63a	from Wh 58
	30.1	89.1 ± 3.0	"	
	33.3	92.5 ± 3.1	"	
	42.0	89.4 ± 3.0	"	
	50	86.4 ± 4.3	Cu 63	from AERS 67
	60	81.1 ± 4.6	"	"
	80	70.5 ± 3.6	"	"
	100	61.3 ± 3.1	"	"
	150	45.0 ± 2.3	"	"
	200	39.0 ± 2.0	"	"
	300	35.8 ± 1.8	"	"
	400	33.6 ± 1.2	"	"
	600	30.8 ± 1.5	"	"
	1000	28.5 ± 1.4	"	"
	2000	27.2 ± 1.4	"	"
	3000	27.1 ± 1.4	"	"
	6000	27.0 ± 1.4	"	"
	10000	26.9 ± 1.4	"	"
	28000	26.8 ± 1.3	"	"
	50.7	85.2 ± 3.0	Me 66	
	59.5	80.3 ± 2.8	"	
	64.7	80.6 ± 2.4	"	
	69.7	75.6 ± 2.3	"	
	79.2	72.6 ± 2.2	"	
	82.7	68.2 ± 2.0	"	
	88.2	67.2 ± 2.0	"	
	98.5	62.7 ± 1.9	"	

TABLE IV. 2i.--Cont.

Target	E (MeV)	$\sigma(^{11}C)$	Refer.	Remarks:
	103.8	61.9 ± 1.9	Me 66	
	108.8	60.5 ± 1.8	"	
	119.4	56.4 ± 1.7	"	
	124.3	55.3 ± 1.7	"	
	128.7	54.9 ± 1.6	"	
	138.3	52.5 ± 1.5	"	
	143.4	51.8 ± 1.5	"	
	149.2	50.6 ± 1.5	"	
	158.6	47.8 ± 1.4	"	
^{14}N	5	10	Bl 51	AERS 67, values obtained from a graph
	5.5	30	"	" , "
	6	40	"	" , "
	6.5	55	"	" , "
	13	69 ± 13	Ma 66	" , $^{14}N\ (p,\alpha)^{11}C$
	145	7.7 ± 1.5	Cl 61	" , *
	156	15 ± 1	Va 63	"
	420	22.4 ± 5.6	Sy 57	" , *
	522	22 ± 5	"	" , *
	648	20 ± 5	"	" , *
	710	18.9 ± 4.7	"	" , *
	835	28.9 ± 7.2	"	" , *
	980	25.5 ± 6.4	"	" , *
	5700	11 ± 4	Be 59	"
	4	10.05 ± 2.45	Es 71	Values obtained from a graph
	5	56.0 ± 14.0	"	"
	6	190 ± 50	"	"
	7	250 ± 50	"	"

TABLE IV.2i.--Cont.

Target	E(MeV)	$\sigma(^{11}C)$	Refer.	Remarks:
	8	225 ± 55	Es 71	Values obtained from a graph
	9	190 ± 40	"	"
	10	190 ± 40	"	"
	12	145 ± 35	"	"
	14	138 ± 33	"	"
	16	125 ± 25	"	"
	18	145 ± 25	"	"
	20	80 ± 20	"	"
	22	65 ± 15	"	"
	24	36 ± 8	"	"
^{16}O	35	2.5 ± 1	Va 64	AERS 67, values obtained from a graph
	38	3.5 ± 1	"	" , "
	45	10 ± 1	"	" , "
	50	13 ± 1	"	" , "
	70	18 ± 1	"	" , "
	100	15 ± 1	"	" , "
	146	12.7 ± 2	Fo 62	"
	155	11 ± 1	Va 63	"
	383	13.6 ± 1.4	Pa 60	"
	420	31 ± 7	Ma 52	"
	420	8.3 ± 2.1	Sy 57	" , *
	522	13 ± 3.2	"	" , *
	648	8.5 ± 2.1	"	" , *
	835	12.1 ± 3	"	" , *
	5700	10 ± 3	Be 60	"

TABLE IV.3.--Production Rate Ratio of ^{7}Li and ^{6}Li (PR(7)/PR(6)) as a Function of γ.

γ	PR(7)/PR(6) Solar Abundance Data	
	Bertsch et al.	Mitler
1.5	1.62	1.60
2.0	1.73	1.72
2.5	1.95	1.78
3.0	2.27	2.21
3.5	2.68	2.58
4.0	3.23	3.07
4.5	3.95	3.72
5.0	4.90	4.59
5.5	6.12	5.62
6.0	7.68	7.18
6.5	9.67	9.04
7.0	12.15	11.41
7.1	12.72	11.95
7.2	14.17	12.52

Chapter V

SUMMARY AND CONCLUSIONS

Production cross sections of ^{20}Ne for mass-6 and mass-7 have been measured at 30, 35, 40, and 42 MeV proton bombarding energies. At each energy the cross sections for mass-6 and mass-7 are, within the experimental uncertainties, equal, and rise from about 1.5 mb at 30 MeV to 4 mb at 42 MeV (see Table III.6 and Figure III.6).

Together with the cross sections of ^{12}C, ^{14}N, and ^{16}O measured in this laboratory and the cross sections compiled in Table IV.2, the ratios of the production rate of ^{7}Li and ^{6}Li by protons in the stellar cosmic rays were calculated. The proton flux was assumed to be proportional to $E^{-\gamma}$ and calculations were made for various values of γ. The observed abundance ratio $n7/n6 = 12.5$ can be achieved only for a $\gamma = 7.1$, while the steepest proton flux that so far has been observed for the sun is $E^{-5.6}$ (Si 70). This means that for this model to be correct there need to be other sources of ^{7}Li or selective depletion of ^{6}Li.

Possible additional sources amenable to laboratory study are the $\alpha + \alpha$ reactions $^4He(\alpha,p)^7Li$ and $^4He(\alpha,d)^6Li$ which favor the production of ^7Li over ^6Li according to Mitler's estimate (Mi 70) based on the inverse reactions $^7Li(p,\alpha)^4He$ and $^6Li(d,\alpha)^4He$. Taking into consideration the abundance of ^4He in the surface of the stars (for the sun it is 2 orders of magnitude more abundant than ^{12}C) the contribution from the $\alpha + \alpha$ reactions can be significant.

APPENDICES

APPENDIX A

FORMULA TO ESTIMATE RANGE OF ^{6}Li IN Si

To estimate the range of ^{6}Li ground state in Si, the following formula was used:

$$R_{Li}(E)_{\alpha} = R\,(E_{\alpha})\left(\frac{M_{Li}}{M_{\alpha}}\right)\left(\frac{Z_{\alpha}}{Z_{Li}}\right)^2$$

$$\text{where } E = E_{\alpha}\left(\frac{M_{Li}}{M_{\alpha}}\right)$$

The energy E of ^{6}Li is known from the kinematics of a two-body final state reaction and hence E_{α} can be calculated and then R_{α} is read from the graph (see Instruction Manual for Surface Barrier Detector, ORTEC).

The formula is based on the assumption that the relative stopping of two materials is independent of ion identity at a given velocity i.e. a given value of E/M (No 70). Explicity, if A and B are two different materials and p and q are two different ions, then at the same velocity:

$$\frac{E_p}{M_p} = \frac{E_q}{M_q}$$

$$\text{or } E_p = E_q \frac{M_p}{M_q}$$

and $$\frac{(dE/dx)p,A}{(dE/dx)p,B} = \frac{(dE/dx)q,A}{(dE/dx)q,B}$$

where $$(dE/dx)p,B \sim \frac{Z_p^{\,2}}{M_p} \; Z_B \qquad \text{(Wi 66)}$$

$$(dE/dx)q,B \sim \frac{Z_q^{\,2}}{M_q} \; Z_B$$

$$(dE/dx)p,A = (dE/dx)q,A \; \frac{(dE/dx)p,B}{(dE/dx)q,B}$$

$$(dE/dx)p,A \simeq (dE/dx)q,A \; \left(\frac{Z_p}{Z_q}\right)^2 \left(\frac{M_q}{M_p}\right)$$

$$R_p(E_p) \approx R_q(E_q) \; \left(\frac{Z_q}{Z_p}\right)^2 \left(\frac{M_p}{M_q}\right)$$

where $E_p = E_q \frac{M_p}{M_q}$

R_p = range of ion p with energy E_p

R_q = range ion q with energy E_q

Z = atomic number of the ion

M = mass of the ion

APPENDIX B

SELECTION OF STOP PULSE AND ITS CONSEQUENCES

Let at $t = 0$ a start pulse arrives at the FD. Assume that the time needed to travel from FD to LRS to DUCO is t_1 nsec. and from there to LRS and back to DUCO and on to TAC is t_2 nsec. ($t_1 + t_2 \approx 18$ nsec.) (see Figure II.5). Delay is then set to $t_1 + t_2$ hence at $t = t_1 + t_2$ TAC will be started.

From $t = t_1$ through $t = (t_1 + 25)$ nsec. DUCO will be closed and no stop pulse is accepted. The first stop pulse to be accepted is the one that arrives at DUCO (coincidence mode) just after $t = (t_1 + 25)$ nsec. and it will arrive at TAC at $t = (t_1 + 25 + t_2)$ nsec. Hence the length of the time signal by TAC is $(t_1 + 25 + t_2)$ nsec. $- (t_1 + t_2)$ nsec. = 25 nsec.

A stop pulse that arrives just before $t = (t_1 + 25)$ nsec. will be rejected and the succeeding stop pulse will be accepted. This corresponds to the maximum TAC signal, equal to 25 nsec. plus T_{RF} (see Figure B.1).

Since the TAC is started by the pulse from the detector and stopped by the RF pulse its output is equal to a T_{RF}-related-constant minus time-of-flight (see Figure B.2). The time interval $\Delta\tau_1$ is adjusted such that the fastest particle corresponds to the maximum TAC output signal as depicted by case I in Figure B.3. The time signals corresponding to slow particles can be obtained by moving the t = 0 position in the direction of increasing time (case II and III) while keeping the positions of the stop pulses the same. Case IV the minimum TAC signal for the slowest of the four particles. The next slower particle, that is with a time of flight difference just greater than T_{RF} from the fastest particle, will have a TAC signal equal to T_{max}. This case will cause an error since $E(T - To)^2$ for this particle will be too small due to a too-small value of $(T-To)^2$. In general every two particles whose time of flights differ by one period of the RF have the same time signal T.

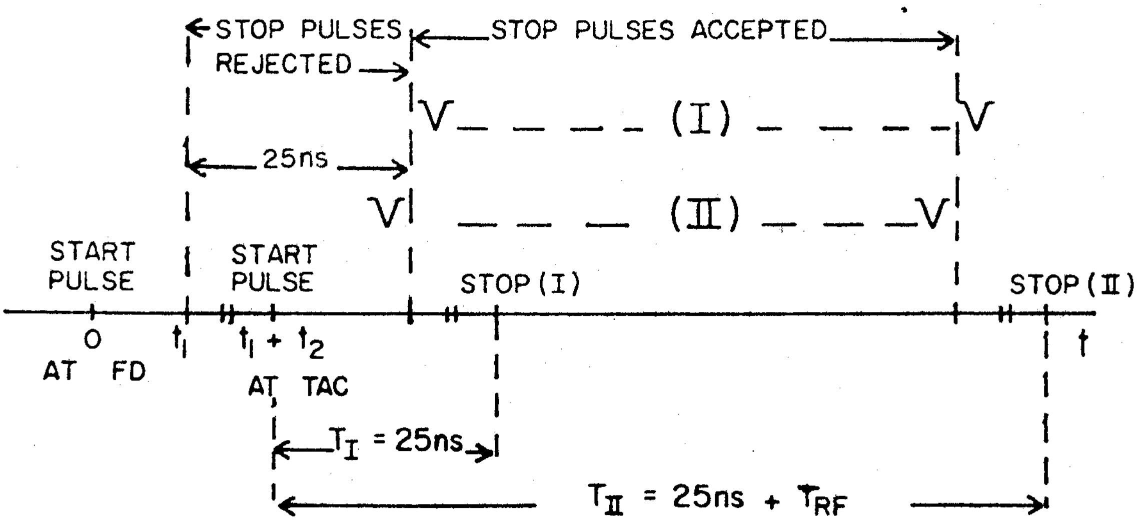

Fig. B1.--Schematic Diagram showing the minimum (T_I) and the maximum (T_{II}) time signals.

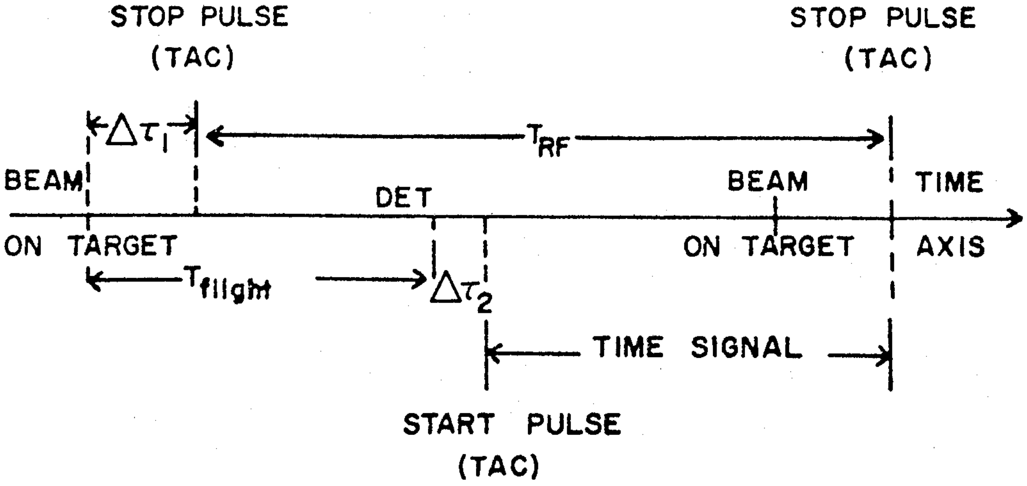

Fig. B2.--$T_S = T_{RF} - T_{flight} + (\Delta\tau_1 - \Delta\tau_2)$.

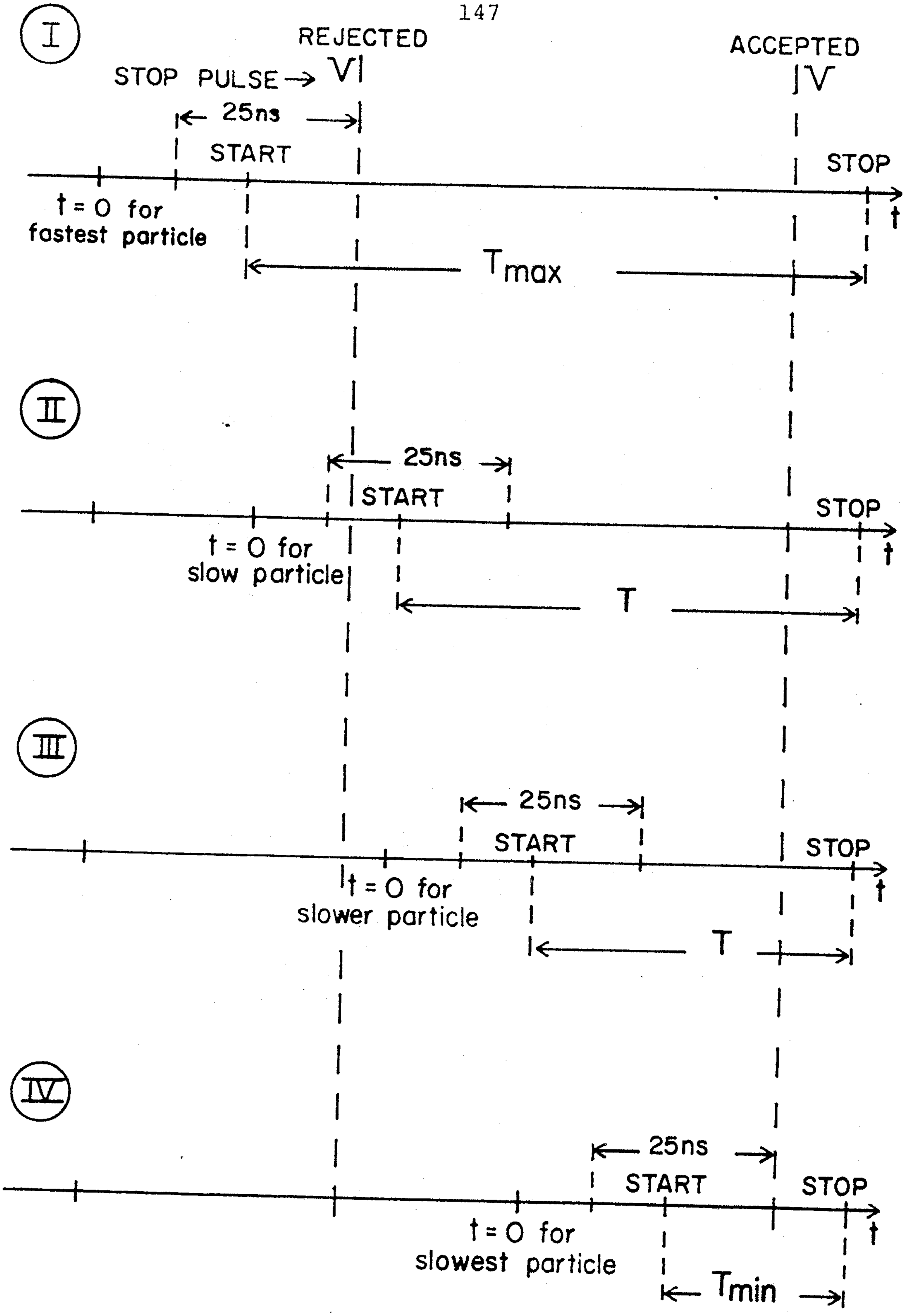

Fig. B3.--Schematic Diagram of the Choice of the Stop Pulse and the Corresponding Time Signal (T).

APPENDIX C

Run No.	Theta	E Proton	Charge (10**-6C)	Pressure (MM Oil)	Monitor	Constant[1]	Percent Error
77.0	15.0	42.1	2092.60	28.80	28708	.476	3.7
78.0	30.0	42.1	1991.70	28.80	27289	.475	3.7
79.0	45.0	42.1	2663.60	28.80	36986	.482	3.7
80.0	65.0	42.1	3333.40	28.80	46365	.482	3.6
81.0	90.0	42.1	3304.80	28.80	46281	.486	3.7
92.0	17.0	40.1	4172.99	58.40	101568	.416	3.2
93.0	30.0	40.1	3969.30	58.10	95928	.415	3.2
94.0	45.0	40.1	3692.20	57.80	90423	.423	3.1
95.0	60.0	40.1	3558.60	57.50	86340	.421	3.1
96.0	80.0	40.1	5183.50	57.40	123170	.413	3.0
97.0	110.0	40.1	3802.80	57.00	48322	.222[2]	3.2
98.0	125.0	40.1	2568.50	56.90	14522	.099[2]	3.4
99.0	10.0	40.1	957.90	56.60	22014	.406	3.2
108.0	17.0	39.9	2000.10	55.11	42375	.384	3.4
109.0	30.0	39.9	2535.20	49.90	45816	.362	3.8
110.0	50.0	39.9	3104.40	51.10	61845	.389	3.4
111.0	70.0	39.9	3076.90	55.80	64877	.377	4.0
189.0	100.0	39.9	3725.60	33.55	51008	.408	3.6
123.0	15.0	29.6	1757.60	50.10	148234	1.683	3.3
124.0	25.0	29.6	2508.30	50.00	202688	1.616	3.8
125.0	55.0	29.6	2096.40	50.00	175851	1.677	3.4
126.0	75.0	29.6	2085.30	49.70	174653	1.685	3.4
127.0	100.0	29.6	1674.80	49.80	137604	1.649	3.5
128.0	37.0	40.0	3216.30	60.00	83327	.431	3.9
129.0	90.0	40.0	2557.20	59.52	67548	.443	3.9
130.0	100.0	40.0	1861.30	59.00	48950	.445	4.0

[1] Constant = Monitor/(Pressure x Charge).
Percent Error = Error assigned to Constant; it includes error in the integrated charge (3%), fit error and statistical error to the fitted peak returned by SAMPO which are added in quadratures.

[2] Monitor counter was positioned at 60° for the runs no. 92 through 99, except for runs no. 96 and 97 where it was positioned at 50°.

Appendix C.--Cont.

Run No.	Theta	E Proton	Charge (10**-6C)	Pressure (MM Oil)	Monitor	Constant	Percent Error
134.0	15.0	35.7	2295.30	54.35	86640	.694	3.6
135.0	30.0	35.7	2457.10	54.00	94081	.709	3.9
136.0	60.0	35.7	3865.30	53.75	137160	.660	4.0
137.0	75.0	35.7	3375.40	53.35	129147	.717	3.8
144.0	20.0	35.0	595.80	59.70	28302	.795	3.2
145.0	60.0	35.0	4135.60	59.70	199394	.807	3.1
146.0	45.0	35.0	3355.80	58.60	154933	.787	3.2
147.0	90.0	35.0	5000.40	58.40	246441	.843	3.1
152.0	55.0	30.0	3259.58	58.80	240563	1.255	3.3
153.0	45.0	30.0	3791.20	58.70	282206	1.268	3.2
154.0	75.0	30.0	5601.70	58.10	415454	1.276	3.4
155.0	25.0	30.1	3028.40	118.51	382353	1.065	3.2
156.0	35.0	30.1	3227.60	117.82	412493	1.084	3.1
157.0	65.0	30.1	3634.70	117.82	477620	1.115	3.1

APPENDIX D

DERIVATION OF MASS RESOLUTION FORMULA

The time-of-flight of a particle is the sum of the time the particle needs to travel over the specified distance D plus the electronic delay and the finite time width of the proton beam burst:

$$T = T_D + T_{BEAM} + T_{TPU} \tag{1}$$

(see Section III.2).

$$\left[\Delta(ET^2)\right]^2 = (\Delta E)^2\left[\frac{\partial(ET^2)}{\partial E}\right]^2 + (\Delta T_D)^2\left[\frac{\partial(ET^2)}{\partial T_D}\right]^2 + (\Delta T_{BEAM})^2\left[(\frac{\partial(ET^2)}{\partial T_{BEAM}}\right]^2 + (\Delta T_{TPU})^2\left[(\frac{\partial(ET^2)}{\partial T_{TPU}}\right]^2$$

$$\frac{\Delta(ET^2)}{ET^2} = \left[\left(\frac{\Delta E}{E}\right)^2 + 4\left[\left(\frac{\Delta T_D}{T}\right)^2 + \left(\frac{\Delta T_{BEAM}}{T}\right)^2 + \left(\frac{\Delta T_{TPU}}{T}\right)^2\right]\right]^{1/2} \tag{2}$$

BIBLIOGRAPHY

BIBLIOGRAPHY

AERS 67 J. Audouze, M. Epherre and H. Reeves in "High Energy Nuclear Reactions in Astrophysics" edited by B. S. P. Shen (W. A. Benjamin Inc., 1967), pp. 256.

Al 62 G. Albouy, J. P. Cohen, M. Gusakow, N. Poffe, H. Sergolle, L. Valentin, Phys. Letter 2, 306 (1962).

Au 62 S. M. Austin, G. L. Salmon, A. B. Clegg, K. J. Foley and D. Newton, Proc. Phys. Soc. 80, 383 (1962).

Ba 71 C. A. Barness in "Advances in Nuclear Physics," Vol. 4, edited by M. Baranger and E. Vogt (Plenum Press, New York, London, 1971), pp. 133.

Ba 70 D. Bayer, The Data Acquisition Task TOOTSIE, MSUCL-34 (1971).

BBFH 57 E. M. Burbidge, G. R. Burbidge, W. A. Fowler and F. Hoyle, Rev. Mod. Phys. 29, 547 (1957).

BCJ 70 D. Bodansky, J. Cameron and W. Jacobs, U. of Wash. Annual Report (1970).

Be 72 D. L. Bertsch, C. E. Fichtel and D. V. Reames, Astrophy. J. 171, 169 (1972).

Be 65 R. Bernas, M. Epherre, E. Gradsztajn, R. Klapisch and F. Yiou, Phys. Lett. 15, 147 (1965).

Be 60 P. A. Benioff, Phys. Rev. 119, 316 (1960).

Be 59 P. A. Benioff, UCRL 8780 (1959).

BGRS 67 R. Bernas, E. Gradsztajn, H. Reeves and E. Schatzman, Ann. Phys. 44, 426 (1967).

Bl 51 J. P. Blaser, F. Boehm, P. Marmier, P. Scherrer, Helv. Phys. Acta 24, 465 (1951).

Br 62 C. Brun, M. Lefort, X. Tarrago, J. Phys. 23, 371 (1962).

Ch 68 K. Chen, Z. Fraenkel, G. Friedlander, J. R. Grover, J. M. Miller and Y. Shimamoto, Phys. Rev. 166, 949 (1968).

Cl 61 A. B. Clegg, K. J. Foley, G. L. Salmon and R. E. Segel, Proc. Phys. Soc. 78, 681 (1961).

Cu 63 J. B. Cumming, Am. Rev. Nucl. Science 13, 26 (1963).

Cu 63a J. B. Cumming, Nucl. Phy. 49, 417 (1963).

Da 70 C. N. Davids, H. Laumer and S. M. Austin, Phys. Rev. C1, 270 (1970).

Do 68 I. Dostrovsky, H. Gauvin and M. Lefort, Phys. Rev. 169, 839 (1968).

Do 65 I. Dostrovsky, R. Davids Jr., A. S. Ponkanzer and P. L. Reeder, Phys. Rev. B139, 1513 (1965).

Do 61 I. Dostrovsky, Z. Fraenkel and J. Hudis, Phys. Rev. 123, 1452 (1961).

Do 60 I. Dostrovsky, Z. Fraenkel and P. Rabinowitz, Phys. Rev. 118, 791 (1960).

Do 59 I. Dostrovsky, Z. Fraenkel and G. Friedlander, Phys. Rev. 116, 683 (1959).

Do 58 I. Dostrovsky, P. Rabinowitz and R. Bivins, Phys. Rev. 111, 1659 (1958).

ES 71 M. Epherre and C. Seide, Phys. Rev. C3, 2167 (1971).

FBB 55	W. A. Fowler, G. R. Burbidge, E. M. Burbidge, Astrophys. J. Suppl. 2, 167 (1955).
Fe 50	E. Fermi, Progr. Theoret. Phys. 5, 570 (1950).
Fo 62	K. J. Foley, Nucl. Phys. 31, 43 (1962).
FPLYB 71	P. Fontes, C. Perron, J. Lestringuez, F. Yiou and R. Bernas, Nucl. Phys. A165, 405 (1971).
Fr 63	P. S. Freier and W. R. Webber, J. Geophys. Res. 68, 1605 (1963).
Ge 62	R. George, Thesis, ORSAY.
Go 60	T. J. Gooding and H. G. Pugh, Nucl. Phys. 18, 46 (1960).
JJBSB 70	M. Jung, C. Jacquot, C. Baixeras-Aiguabella, R. Schmitt and H. Braun, Phys. Rev. C1, 435 (1970).
Ho 64	M. Honda and D. Lal, Nucl. Phys. 51, 363 (1964).
Ho 61	H. M. Hoogenboom, Rev. Sci. Instr. 32, 1393 (1961).
Hs 70	K. C. Hsieh and J. A. Simpson, Astrophy. J. 162, L191 (1970).
Kl 67	R. Klapisch, "Complement to the Survey of Cross Section" by J. Audouze, M. Epherre and H. Reeves (1967).
Ko 70a	R. G. Korteling and A. A. Caretto Jr., Phys. Rev. C1, 193 (1970).
Ko 70b	R. G. Korteling and A. A. Caretto Jr., Phys. Rev. C1, 1960 (1970).
La 71	H. W. Laumer, Thesis, Mich. State Univ., p. 15 (1971).

La 66 M. S. Laffleur, N. T. Porile and L. Yaffe, Can. J. Chem. 44, 2749 (1966).

Ma 52 L. Marquez, Phys. Rev. 86, 405 (1960).

Me 66 D. F. Measday, Nucl. Phys. 78, 476 (1966).

Mi 70 H. E. Mitler, "Cosmic-Ray Production of Light elements in the Galaxy." Smithsonian Astrophysical Observatory Special Report 330 (1970).

No 70 L. C. Northciffe and R. F. Schilling, Nucl. Data A7, 233 (1970).

Pa 60 V. Parikh, Nucl. Phys. 18, 646 (1960).

Ra 64 G. F. S. Rayudu, Can. J. Chem. 42, 1149 (1964).

Re 65 P. L. Reeder, J. Inorg, Nucl. Chem. 27, 1879 (1965).

Ro 58 F. S. Rowland and R. L. Wolfgang, Phys. Rev. 110, 175 (1958).

Ru 66 G. Rudstam, Z. Natuurforsch. 21A, 1027 (1966).

Ru 55 G. Rudstam, Phil. Mag. 46, 344 (1955).

Se 47 R. Serber, Phys. Rev. 72, 1114 (1947).

Si 72 R. Silberberg and C. H. Tsao, "Partial Cross Sections in High Energy Nuclear Reaction." NRL (1972).

Si 70 J. A. Simpson, private communication.

Si 59 E. Silverstein, Nucl. Instr. Meth. 4, 53 (1959).

ST 68 A. F. Stehny and E. P. Steinberg, Nucl. Phys. B5, 188 (1968).

St 63	R. M. Sternheimer, Method of Experimental Physics, Vol. 5, Part B, edited by C. Marton, Academic Press, New York, 1963.
Su 56	H. E. Suess and H. C. Urey, Rev. Mod. Phys. 28, 53 (1956).
Sy 57	J. L. Symonds, J. Warren and J. D. Young, Proc. Phys. Soc. A70, 824 (1957).
Va 64	L. Valentin, Thesis, ORSAY.
Va 63	L. Valentin, G. Albauy, J. P. Cohen, M. Gusakow, Phys. Lett. 7, 163 (1963).
We 37	V. F. Weisskopf, Phys. Rev. 52, 295 (1937).
WFH 67	R. V. Wagoner, W. A. Fowler and F. Hoyle, Astrophy. J. 148, 3 (1967).
Wh 58	A. B. Whitehead and J. S. Foster, Can. J. Phys. 36, 1276 (1958).
Wi 67	I. R. Williams and C. B. Fulmer, Phys. Rev. 154, 1005 (1967).
Wi 66	C. F. Williamson, J. P. Boujot and J. Picard, Tables of Range and Stopping Power of Chemical Elements for Charged Particles of Energy 0.05 to 500 MeV, Rapport CEA-R3042 (1966).
Wo 53	H. R. Worthington, J. N. McGruer and D. E. Findley, Phys. Rev. 90, 899 (1953).
YBDFGB 68	F. Yiou, M. Baril, J. Dufaure de Citres, P. Fontes, E. Gradsztajn and R. Bernas, Phys. Rev. 166, 968 (1968).
YSB 69	F. Yiou, C. Seide and R. Bernas, J. Geophys. Res. 74, 2447 (1969).